The Dissertation Committee for Yafei Liu Certifies that this is the approved version of the following dissertation:

Structural Integrity of Pipelines Using Reeling Installation Method

Committee:

Stelios Kyriakides, Supervisor

Michael D. Engelhardt

Rui Huang

Kenneth M. Liechti

Krishnaswa Ravi-Chandar

Structural Integrity of Pipelines Using Reeling Installation Method

by

Yafei Liu

Dissertation

Presented to the Faculty of the Graduate School of

The University of Texas at Austin

in Partial Fulfillment

of the Requirements

for the Degree of

Doctor of Philosophy

The University of Texas at Austin

December 2017

Dedication

To my family.

Acknowledgements

I would like to express my special appreciation to my advisor, Professor Stelios Kyriakides, who has been a tremendous mentor for me throughout my studies. This study would not have been possible without his continuous support and guidance. His advices on my research are priceless, and his enthusiasm and dedication to scientific research have deeply influenced me. The guidance he gave on writing and improving this dissertation is also acknowledged with thanks.

In addition I would like to thank the members of my dissertation committee, Professors Michael Engelhardt, Rui Huang, Kenneth M. Liechti, and K. Ravi-Chandar for their questions, comments, and suggestions on my research and for the time they spent reviewing my dissertation.

This study was financially supported by a consortium of industrial sponsors under the joint industry project Structural Integrity of Offshore Pipelines and by the University of Texas at Austin. Both sources of support are acknowledged with thanks.

Special thanks are given to Dr. Julian Hallai for his help with the study on the effect of Lüders banding on reeled pipe. The following senior members of our research group helped me to overcome difficulties in my research are acknowledged: Drs. Liang-Hai Lee, Rong Jiao, Lin Yuan, Stavros Gaitanaros, Nathan Bechle, and Wen-Yea Jang. It has also been a great joy for me to work with the talented and friendly fellow students in the group: Dongjie Jiang, Kelin Chen, Chenglin Yang, Benjamin Harrison, Martin Scales, and Karlos Kazin.

Structural Integrity of Pipelines Using Reeling Installation Method

Yafei Liu, Ph.D.

The University of Texas at Austin, 2017

Supervisor: Stelios Kyriakides

In the reeling method for installing offshore pipelines, several miles of line are wound onto a large diameter drum onshore mounted on a vessel. The vessel travels to the installation site where the line is unwound gradually installing it to the sea floor. This process involves repeated excursions into the plastic strain range of 1-3%. This study examines three structural integrity issues that arise from the process. A full-scale numerical modeling scheme incorporating nonlinear kinematic hardening plasticity is developed for the reeling/unreeling process.

The first issue studied is the degradation of the cross section of pipelines and its effect on the collapse pressure. To capture the ovalization induced and assess its impact on the structural performance of the pipeline in deeper waters, the complete 3-D finite element model and a simplified 2-D model are presented to simulate reeling/unreeling of up to three cycles and subsequent collapsing under external pressure. Comparison of the results of such simulations with experiments highlights when fully a 3-D model is required and when the simpler 2-D model is adequate for evaluating the structural performance of a reeled pipe.

The second issue investigated is the discontinuity in pipelines. In order to show how discontinuities in geometry and mechanical properties can lead to buckling and failure, the 3-D numerical model is applied to simulate the reeling/unreeling of pipelines.

Discontinuities are shown to result in sharp local changes in accompanied by severe local straining and ovalization. These local effects can be reduced by increasing the applied tension at the expense of additional ovalization of the pipeline.

The last part of the study examines the complication brought in by reeling pipes that exhibit Lüders bands. To simulate this process, the material is modeled by a stress–strain response with a negative slope over the extent of the Lüders deformation. During reeling with some back tension, Lüders banding produces inclined bands of localized deformation organized in clusters with distinctly different spatial distribution than that of pure bending. As a consequence, the ovalization develops axial undulations. The influences of problem variables are examined in a detailed parametric study.

Table of Contents

Chapter 1: INTRODUCTION

The installation of pipelines to the sea floor constitutes one of the most challenging offshore operations. Several pipe-lay processes have been developed each involving different types of large installation vessels whose operation requires sophisticated engineering technology and high cost. The high level of technology required and the cost of the vessels used have made pipelaying an engineering discipline on its own accord. The most commonly used installation methods include S-Lay, J-Lay and reeling (Kyriakides and Corona [2007]). This thesis develops some of the technology associated with the reeling pipeline installation method.

The installation process involves winding several kilometers of linepipe onto a large diameter reel mounted on a sea going vessel. The vessel travels to the offshore installation site where the pipeline is gradually unwound and installed on the sea floor along a predetermined path. Having the pipes welded at the spooling base on land, the continuity of the pipe-laying process, and the resultant speed of installation make reeling more efficient and cost effective than the J- or S-lay methods. Thus, reeling installation is increasingly preferred for many pipeline, flowline, and riser projects that involve pipe diameters of 16 in or less (Kyriakides and Corona [2007]).

As a consequence of significant increase in demand in the use of reeling, the reeling vessel fleet, which was born in the 1970s with the Chickasaw and Apache vessels (Kyriakides and Corona [2007]), has undergone a vast expansion with many larger, more powerful and versatile new vessels such as the Apache II, Deep Blue, Seven Oceans, Seven Navica, Deep Energy, Aegir and Seven Pacific. The reel vessels currently in use can install pipelines at speeds of up to two knots, which is significantly faster than the lay speeds of competing installation methods.

Winding a pipe of diameter D onto a reel radius ρ, as shown in Fig. 1.1a, results in a bending strain of

$$\varepsilon = \frac{D}{(2\rho + D)}. \tag{1.1}$$

For typical pipe and reel dimensions (1.1) implies strains of 1-3%, which are well into the plastic range of the material. Consequently, the pipeline must be designed against the possibility of buckling and collapse due to bending. The wall thickness and the mechanical properties of the pipe must be chosen such that local buckling by bending is avoided. The possibility of buckling is further reduced by applying some level of back tension during both the winding and unwinding of the pipe onto the reel (Kyriakides and Corona [2007]).

On unspooling, the line is first straightened and bent once more to a second radius on the ramp shown in Fig. 1.1b, before it is straightened again and reversed bent to end up at zero moment and curvature. Figure 1.1c schematically shows the bending moment-curvature history experienced by one point in the line during the complete winding/unwinding process. The pipe is first wound onto the reel and plastically bent to curvature κ_1 (0-1). It is then unwound and straightened under applied back tension (1-2), and overbent again to curvature κ_3 on the ramp (2-3). Following the overbend, the pipe is straightened again (3-4) and reverse bent in the straightener (4-5). Finally, it is unloaded (5-0) and ends up at approximately zero moment and curvature (Kyriakides and Corona [2007]).

The combined tension and bending cycles introduce changes to the mechanical properties (e.g., Meissner et al. [2012], Tsuru et al. [2013], Liu et al. [2016]) and the cross sectional geometry of the pipe, which in turn affect its integrity and performance

during installation and operation (e.g., Kyriakides and Mok [1992], Dyau and Kyriakides [1992], Chatzopoulou et al. [2016], Kyriakides [2017]).

The main objective of this study is to examine three structural integrity problems that arise from the reeling/unreeling process that lead to pipeline degradation and/or collapse. The problems are tackled using a large-scale three-dimensional numerical model for the reeling/unreeling process that is developed. The numerical modeling must address the geometric and contact nonlinearities associated with reeling. It is further complicated by challenging constitutive issues that arise from the loading/reverse loading histories and by Lüders banding that affects some line grade steels.

1.1 Effects of Reeling on Pipe Structural Performance

The first problem considered is the structural and material degradation suffered by a pipeline due to repeated reeling and unreeling cycles. Cyclic bending of a tube into the plastic range is known to result in progressive accumulation of ovalization of its cross-section. Once a critical value of ovality is reached, the tube buckles. During each loading cycle, the ovality grows with curvature during the bending phase, and decreases during the unbending and reverse bending phase (Kyriakides and Shaw [1987] and Corona and Kyriakides [1991]). During the reeling/unreeling process outlined in the introduction, the pipe experiences repeated bending and straightening. Furthermore, while in contact with the surface of the reel the pipe undergoes a transverse force due to the applied back tension, which tends to aggravate the cross sectional distortion (Dyau and Kyriakides [1992] and Chapter 10 of Kyriakides and Corona [2007]). The reeling under tension experiments of Kyriakides and Mok [1992] (see also Kyriakides [2017]) demonstrated that the repeated plastic bending and reverse bending associated with reeling not only

progressively ovalizes the pipe but also elongates it. These geometric changes and the changes in mechanical properties cause a reduction in the collapse pressure.

Chapter 3 studies the reeling induced degradation of a pipeline using custom numerical models of the reeling process. The problem involves geometric, material, and contact nonlinearities, and the additional complication of cyclic plasticity. The models are first evaluated by direct comparison to the experimental results of Kyriakides and Mok [1992]. They are subsequently used to study the problem parametrically.

1.2 Effect of Geometric and Material Discontinuities on the Reeling of Pipelines

One of the potential limit states of the reeling installation process is bending-induced local buckling (e.g., Ju and Kyriakides [1991, 1992], Kyriakides and Ju [1992], Crome [1999] and Corona et al. [2006]). This is avoided by appropriate choice of pipe diameter-to-thickness ratio (D/t) and back tension applied during spooling and unspooling (e.g., Brown et al. [2004], Smith et al. [2011]). Girth welds and the associated heat-affected zones tend to have somewhat different mechanical properties, which can induce severe local straining and deformation. Consequently, girth welds tend to receive special consideration (e.g., Ernst et al. [2007], Netto et al. [2008]). In addition, variation of the material yield stress along the length of a string of pipe, and variations among different strings often cause sharp discontinuities (see Bauer et al. [2002], Tsuru et al. [2012]). Furthermore, discontinuities in pipe wall thickness are common (Sriskandarajah et al. [2011]). When pipes with such discontinuities are reeled, localized bending, ovalization and straining that develop in the vicinity of discontinuities can lead to local buckling and rupture (Brown et al. [2004]; Denniel et al. [2009] Smith et al. [2011], Liu and Kyriakides [2014]). An example of such a local buckle during the reeling process is shown in Fig. 1.2. A 12-inch pipe with D/t = 21.25 with a thickness discontinuity of

12.5% is wound on to a reel with radius of about 25D. During winding the discontinuity caused locally excessive plastic deformation and ovalization, but the pipe remained intact. However, it developed a sharp local buckle during unwinding and straightening. The extent of damage is such that the pipe could fracture and separate in two with very severe consequences.

A study that examines the local effects of discontinuities in pipe geometry and mechanical properties and the potential of buckling and failure is presented in Chapter 4. The problem is studied using a large-scale finite element framework similar to that developed in Chapter 3, which captures the effects of reeling and unreeling in the neighborhood of yield stress and thickness discontinuities.

1.3 Reeling of Pipe with Lüders Bands

Plastic bending of tubes and pipes tends to ovalize the cross section, which reduces the bending rigidity and can lead to a limit load instability and collapse. Wrinkling on the compressed side is a second type of instability, which for higher D/t pipes leads to collapse by local kinking. The response and these limit states are further complicated when the steel exhibits Lüders banding following initial yielding. This is a dislocation driven material instability whose macroscopic effect is inhomogeneous deformation. In a series of pure bending experiments on tubes with Lüders bands, Hallai and Kyriakides [2011a] demonstrated that Lüders banding leads to localization of curvature that under "favorable" conditions can propagate until the whole structure is Lüders deformed; but under "unfavorable" conditions leads to premature local collapse. An example of such a local collapse is shown is Fig. 1.3 (from Hallai and Kyriakides [2011b]). A tube with a D/t = 24.26 and a Lüders strain of 2.55% is deformed under rotation-controlled pure bending. As the bending progresses, Lüders bands initiate from

the plane of symmetry on the left and get organized in diamond-shaped pockets. The Lüders deformed section bends to a higher curvature, which propagates to the right (images ② to ⑦). The propagation of the higher curvature is interrupted in image ⑧ due to excessive ovalization of the Lüders deformed section. In Image ⑨ the tube collapses in the neighborhood of the plane of symmetry. This behavior is caused by a complex interaction between the underlying material instability and structural nonlinearities of ovalization and wrinkling. It was further demonstrated that all aspects of the problem observed in experiments can be simulated numerically by modeling the material as an elastic–plastic solid with an "up-down-up" response over the extent of the Lüders strain, followed by hardening (Aguirre et al. [2004], Kyriakides et al. [2008], Hallai and Kyriakides [2011b]).

The present study examines the effect of Lüders banding on a pipe that is plastically bent in a reeling operation. Unlike in the case of pure bending, the reeled pipe bends through a transition zone several diameters long until it conforms to the reel curvature. There exists significant variation of curvature through this transition zone, which is thought to make buckling and collapse less likely. Furthermore, the applied back tension and contact with the reel are thought to further stabilize the cross section. These effects are studied parametrically using a fully 3-D numerical model that simulates the reeling process using a similar constitutive model as that used in Hallai and Kyriakides [2011b].

1.4 OUTLINE

The present study develops a full-scale numerical model for the reeling/unreeling process that involves challenging constitutive issues. This thesis starts by introducing the nonlinear kinematic plasticity models adopted, described in Chapter 2.

Chapter 3 describes the first problem studied using this modeling framework: the degradation of the cross section of pipelines and its effect on the collapse pressure. The constitutive models presented in Chapter 2 are used to simulate reeling/unreeling of up to three cycles and subsequent collapsing under external pressure in a typical practical setting.

Chapter 4 describes the second problem studied: reeling/unreeling of pipelines with discontinuities. The aim of the study is to show how discontinuities in geometry and mechanical properties can lead to buckling and failure.

Chapter 5 describes the complication brought in by reeling pipes that exhibit Lüders bands.

Chapter 6 contains a summary of the present study along with major conclusions.

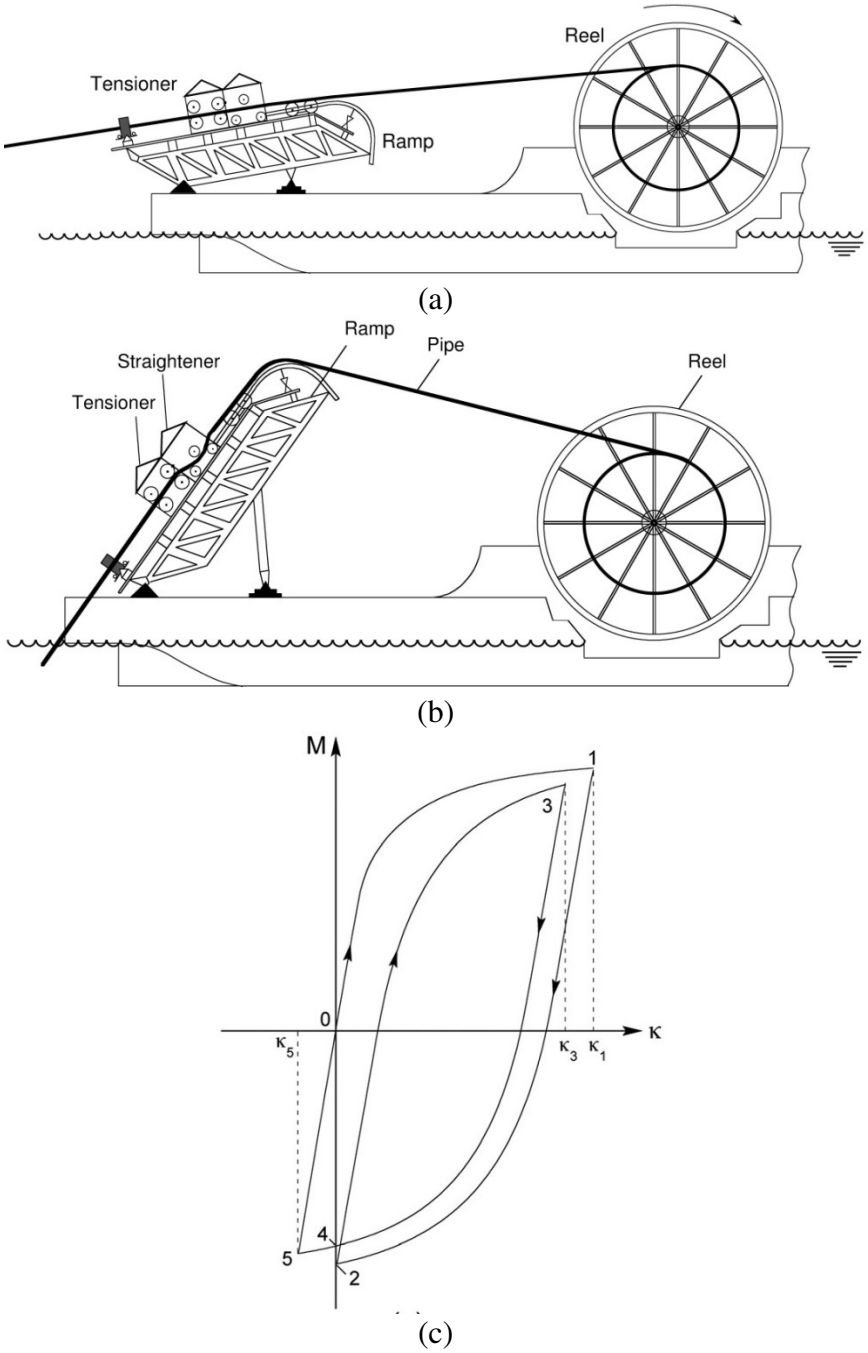

Figure 1.1 Schematics showing a typical reeling vessel configuration during: (a) spooling and (b) installation. (c) Moment-curvature history induced to a pipe section by the process.

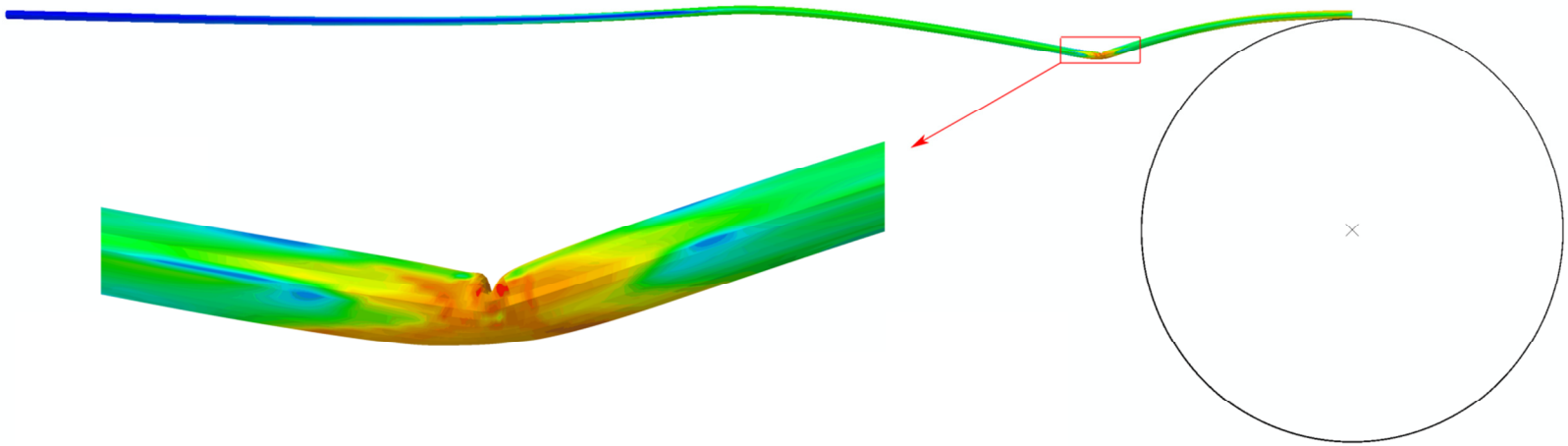

Figure 1.2 Reeled pipeline that buckled during unwinding at a section with thickness discontinuity ($\Delta t = 0.125t$, $T = 0.025T_o$).

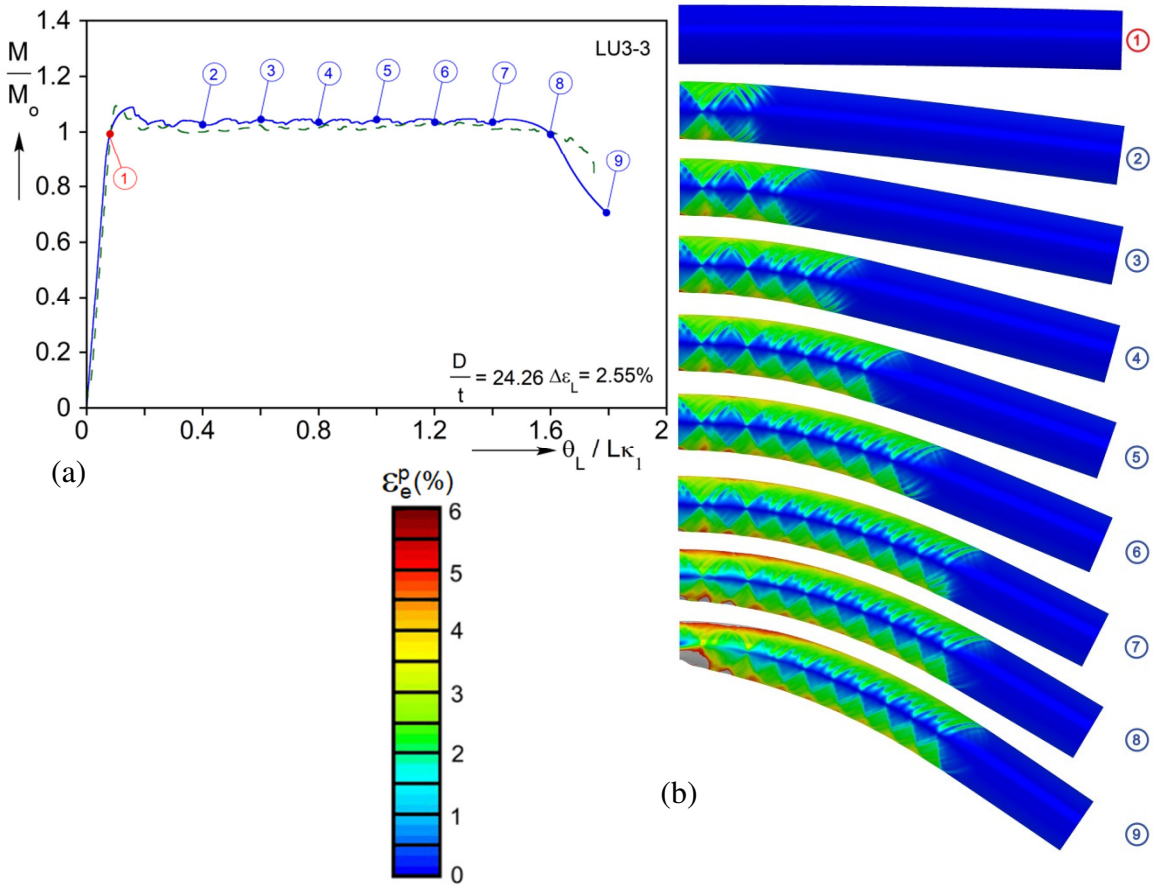

Fig. 1.3 Calculated results for a pipe with Lüders bands under pure bending: (a) comparison of measured and calculated moment-end-rotation response and (b) calculated deformed configurations (Hallai and Kyriakides [2011b]).

Chapter 2: CONSTITUTIVE MODELS

The reeling installation process of offshore pipelines involves repeated plastic loading, unloading, and reverse loading. To simulate this behavior, nonlinear kinematic hardening plasticity models are adopted to represent the material behavior. The Chaboche nonlinear kinematic hardening model (Chaboche [1986]) is used for the 3-D finite element simulations and the two-surface Tseng-Lee [1983] model is used in a simpler 2-D modeling scheme. The two constitutive models are outlined in this chapter together with and their calibration to cyclic stress-strain relationships for steel.

2.1 CHABOCHE NONLINEAR KINEMATIC HARDENING MODEL [1986]

The Chaboche [1986] nonlinear kinematic hardening model (see also Lemaitre and Chaboche [1990]) adopts a J_2-type yield surface expressed as

$$f(\boldsymbol{\sigma}-\boldsymbol{\alpha})=\left[\frac{3}{2}(\boldsymbol{s}-\boldsymbol{a})\cdot(\boldsymbol{s}-\boldsymbol{a})\right]^{1/2}=\sigma_O, \tag{2.1}$$

where $\boldsymbol{\sigma}$ is the stress tensor, $\boldsymbol{\alpha}$ is the current center of the yield surface (or back stress), $\boldsymbol{s}$ and $\boldsymbol{a}$ are their respective deviators, and σ_o is the size of yield surface. Plastic deformations obey the flow rule

$$d\boldsymbol{\varepsilon}^p=\frac{1}{H}\left(\frac{\partial f}{\partial\boldsymbol{\sigma}}\cdot d\boldsymbol{\sigma}\right)\frac{\partial f}{\partial\boldsymbol{\sigma}}, \tag{2.2}$$

where H is the plastic modulus, which for uniaxial loading is reduces to

$$H=\frac{d\sigma}{d\varepsilon^p}. \tag{2.3}$$

The model is completed by incorporating a nonlinear kinematic hardening rule to the flow rule. The increment of deviatoric back stress tensor is represented by a superposition of several Armstrong-Frederic [1966] hardening rules as follows:

$$d\boldsymbol{a} = \sum_{i=1}^{M} d\boldsymbol{a}_i\,,\quad d\boldsymbol{a}_i = \frac{2}{3}C_i d\boldsymbol{\varepsilon}^p - \gamma_i \boldsymbol{a}_i d\varepsilon_e^p\,,\quad d\varepsilon_e^p = (2d\boldsymbol{\varepsilon}^p \cdot d\boldsymbol{\varepsilon}^p / 3)^{1/2}\,(i:1, N \text{ no sum}), \quad (2.4)$$

where C_i are the initial kinematic hardening moduli and γ_i determine the rate of decrease of the moduli as the material hardens. The plastic modulus for each hardening rule can be determined for the consistency condition to be:

$$H_i = C_i - \frac{3}{2}\gamma_i \boldsymbol{a} \cdot \frac{(\boldsymbol{s} - \boldsymbol{a})}{\sigma_o}. \quad (2.5)$$

2.1.1 Calibration of the Chaboche Model

The model is calibrated to a measured stress-strain response by choosing *N* pairs of material parameters, C_i and γ_i, which correspond to *N* superposed hardening rules. The calibration will be demonstrated using a stainless-steel 304 stress-strain response used in Chapter 3 (Armstrong-Frederic [1966], Bari and Hassan [2000], Chaboche [1986]). For a uniaxial stress-state, Eq. (2.5) reduces to

$$H_i = \frac{d\alpha_{11}}{d\varepsilon_{11}^p} = C_i - \gamma_i \alpha_{11} \text{sig}(\sigma_{11} - \alpha_{11}), \quad (2.6)$$

where α_{11} and σ_{11} are the back stress and stress components in the loading direction respectively and $d\varepsilon_{11}^p$ is the plastic strain increment. Integrating (2.6) produces the following exponential relationship between stress and plastic strain

$$\alpha_{11} = \frac{C_i}{\gamma_i}\left(1 - e^{-\gamma_i \varepsilon_{11}^p}\right). \quad (2.7)$$

Thus, γ_i governs the rate of decay of the response and $\alpha_{11} = C_i / \gamma_i$ is the stress at relatively large values of strain.

Figure 2.1 shows an example construction of the plastic part of a hardening stress-strain response using *N* = 3. The first hardening rule starts with a very large plastic

modulus and stabilizes very quickly as shown in the figure, which means having larger C_1 and γ_1. The second rule captures the transient nonlinear portion of the response, and thus C_2 and γ_2 have intermediate values. The third rule has a linear hardening rule with $\gamma_3 = 0$ representing the hardening at larger values of strains. The three sets of constants chosen are listed in Table 2.1 and the resultant stress-plastic strain plots are plotted in Fig. 2.1.

Table 2.1 Material parameters for the Chaboche constitutive model.

E Msi (GPa)	σ_o ksi (MPa)	C_1 Msi (GPa)	γ_1	C_2 Msi (GPa)	γ_2	C_3 Msi (GPa)	γ_3
30.3 (207)	17.1 (118)	16.2 (112)	2421	6.76 (46.6)	451.2	0.428 (2.95)	0

2.1.2 Calibration to Measured Steel Stress-strain Responses

This process was used to calibrate the model to experimental uniaxial stress-strain responses of two steels used in Chapters 3 and 4. Here the material parameters are determined from a uniaxial stable hysteresis curve instead of the monotonic curve. Also, the third component has a non-zero γ_3 so that the calibration better captures the nonlinearity of the hardening. This requires a hysteresis loop of relatively high strain range, which in this case is 1-2%. The first material studied is X-60 line-grade steel. The material parameters are presented in Table 2.2. Figure 2.2 compares the calibrated monotonic and hysteresis responses generated for uniaxial loading to experimental results. The calibration is seen to fit the experimental results well. Included in the figure with a dashed line is the prediction of these responses using isotropic hardening. As expected, this model does not capture the Bauschinger effect well, which as will be demonstrated adversely influences the unreeling results.

Table 2.2 Material parameters for the Chaboche constitutive model of X-60.

E Msi (GPa)	σ_o ksi (MPa)	C_1 Msi (GPa)	γ_1	C_2 Msi (GPa)	γ_2	C_3 Msi (GPa)	γ_3
30.0 (207)	53.7 (370)	1.058 (7.29)	82.34	1.692 (11.7)	252.4	3.509 (24.2)	801.7

The model was also calibrated to representative measured cyclic uniaxial stress-strain responses of the two families of SS-304 tube materials used in the experiments described in Chapter 3 and the extracted parameters are listed in Table 2.3. Figure 2.3 compares the measured response to that of the calibrated model for tubes with D/t = 15.5 and 20. The initial monotonic response and the two unloading/reverse loading parts of the hysteresis loops are captured very well whereas the reloading section of the hysteresis is underpredicted to some extent.

Table 2.3 Material parameters for the Chaboche constitutive model of SS-304.

$\frac{D}{t}$	E Msi (GPa)	σ_o ksi (MPa)	C_1 Msi (GPa)	γ_1	C_2 Msi (GPa)	γ_2	C_3 Msi (GPa)	γ_3
20	30.3 (209)	30.6 (211)	20.87 (143.9)	5325	9.734 (67.11)	1084	3.496 (24.10)	254.1
15.5	28.4 (196)	28.8 (199)	0.834 (5.75)	96.94	12.31 (84.87)	712.6	110.2 (759.8)	10910

In addition to the kinematic effect, plastic straining causes an increase in the dislocation density and change of dislocation distribution, which can cause a change in the size of yield surface (Chaboche [1986]). To capture this phenomenon, the model allows for the yield surface size to evolve (isotropic hardening) as a function of the plastic strain. In the present calibration, this feature is used to capture the difference between the initial monotonic and hysteresis responses. This is accomplished by

providing a table of stress and plastic strain values on the monotonic response as shown in Table 2.4 for SS-304 steel used in Chapter 3. The yield surface starts with a larger value than that of the hysteresis response. As ε^p increases, the code adjusts the size of the yield surface. In this case the size in Eq. (2.1) decreases, until it matches that of the hysteresis; subsequently the yield surface stays constant.

Table 2.4 Evolution of the yield surface size for Chaboche constitutive model of SS-304.

$\frac{D}{t}=20$	ε^p	0	0.001	0.002	0.003	0.005	0.01
	σ_o ksi (MPa)	30.6 (211)	24.3 (168)	21.1 (146)	18.6 (128)	17.3 (209)	17.1 (209)
$\frac{D}{t}=15.5$	ε^p	0	0.002	0.004	0.006	0.008	0.01
	σ_o ksi (MPa)	28.8 (199)	26.3 (209)	22.3 (209)	21.8 (209)	20.8 (209)	20.3 (209)

2.2 TSENG-LEE MODEL [1983]

This is a non-linear kinematic hardening model with two surfaces: a yield surface and a memory surface that encloses the yield surface. The yield surface is given by

$$f(\boldsymbol{\sigma}-\boldsymbol{\alpha})=\left[\frac{3}{2}(\boldsymbol{s}-\boldsymbol{a}).(\boldsymbol{s}-\boldsymbol{a})\right]^{1/2}=\sigma_o \tag{2.8}$$

where σ_o represents its size. The memory, represented by

$$F(\boldsymbol{\sigma})=\left[\frac{3}{2}\boldsymbol{s}.\boldsymbol{s}\right]^{1/2}=\sigma_b \tag{2.9}$$

is centered at the origin with its current size σ_b representing the maximum stress state in history. The memory surface grows isotropically any time the state of stress exceeds σ_b. During the initial loading the flow rule is based on the memory surface and is given by

$$d\varepsilon_{ij}^{p} = \frac{1}{H}\left(\frac{\partial F}{\partial \sigma_{mn}} d\sigma_{mn}\right)\frac{\partial F}{\partial \sigma_{ij}} \tag{2.10}$$

where $H = \dfrac{d\sigma_1}{d\varepsilon_1^p}$

is evaluated from the monotonic stress-strain response (oab in Fig. 2.4a). The yield surface stays attached to the memory at the current stress point. It detaches on the first reverse loading and subsequently the flow rule is based on the yield function as follows:

$$d\varepsilon_{ij}^{p} = \frac{1}{H}\left(\frac{\partial f}{\partial \sigma_{mn}} d\sigma_{mn}\right)\frac{\partial f}{\partial \sigma_{ij}} \tag{2.11}$$

The yield surface translates according to

$$d\alpha_{ij} = d\mu(\bar{\sigma}_{ij} - \sigma_{ij}) \tag{2.12}$$

where

$$\bar{\sigma}_{ij} = \frac{\sigma_b}{\sigma_o}(\sigma_{ij} - \alpha_{ij}) \tag{2.13}$$

as shown in Fig. 2.4b (Mroz [1967]). The plastic modulus, H, is now evaluated from

$$H(\delta, \delta_{in}) = E_m^p\left[1 + h\left(\frac{\delta}{\delta_{in} - \delta}\right)\right] \tag{2.14}$$

where E_m^p is the plastic modulus of the memory at σ_b and δ is a stress measure from the current plastic state to the memory surface, which in the uniaxial setting is represented by two horizontal lines located at the maximum stress level reached in history $\pm\sigma_b$. Similarly, δ_{in} is the value of δ at the last elastic state (see Fig. 2.4). h is a fit parameter of the monotonic (oab) or stable hysteresis response (bcde) determined as outlined in the Appendix. In the multiaxial setting, δ is generalized as follows:

$$\delta = \left[(\bar{\boldsymbol{\sigma}} - \boldsymbol{\sigma}) \cdot (\bar{\boldsymbol{\sigma}} - \boldsymbol{\sigma})\right]^{1/2} \tag{2.15}$$

(see also Dafalias and Popov [1975,1976]).

2.2.1 Calibration of Tseng-Lee Model (see Appendices C and F of Kyriakides and Corona [2007])

The Tseng-Lee model is calibrated using the same uniaxial stress-strain data. The monotonic part of the response (oab in Fig. 2.4a) is fitted with the Ramburg-Osgood fit, which is a powerlaw relationship expressed as

$$\varepsilon = \frac{\sigma}{E}\left[1+\frac{3}{7}\left(\frac{\sigma}{\sigma_y}\right)^{n-1}\right] \tag{2.16}$$

where E, σ_y and n are fit parameters that can be determined from a measured stress-strain response.

The material parameters for the basic hysteresis curve (bcde) are determined as follows:

E_c is the elastic modulus of the hysteresis curve. It is the slope of the unloading curve (bc). It is usually assumed to equal the elastic modulus of the loading curve, i.e. $E_c = E_m$.

σ_{oc} is the radius of the yield surface is calculated by identifying the elastic limit of the hysteresis curve (point c):

$$\sigma_{oc} = \frac{1}{2}(\sigma_b - \sigma_c) \tag{2.17}$$

where σ_b and σ_c are the stresses corresponding to the points b and c on the response.

h is a shape parameter representing the hardening characteristics of the hysteresis curve. It is calculated as follows:

The slope, or plastic modulus, of the monotonic curve at point b is

$$E_m^p = \left(\frac{1}{E_m} - \frac{1}{E}\right)^{-1} \tag{2.18}$$

The stress at point b, σ_b, represents the current size of the memory surface.

The second memory line is constructed by drawing a horizontal line through point b, i.e. at stress σ_b.

The second memory line is constructed as the horizontal line $\sigma = -\sigma_b$.

δ_{in} is evaluated as

$$\delta_{in} = \sigma_c + \sigma_b \tag{2.19}$$

Then choose a point on the unloading curve, point d, and evaluate δ as follows

$$\delta = \sigma_d + \sigma_b \tag{2.20}$$

where point d is chosen such that

$$0.1 \le \frac{\delta}{\delta_{in}} \le 0.5 \tag{2.21}$$

The plastic strains corresponding to points c and d are evaluated as follows:

$$\varepsilon_c^p = \varepsilon_c - \frac{\sigma_c}{E_C} \quad \text{and} \quad \varepsilon_c^p = \varepsilon_d - \frac{\sigma_d}{E_C} \tag{2.22}$$

where ε_c and ε_d are the strains at points c and d, respectively.

h is evaluated by solving the following nonlinear equation

$$\frac{\delta_{in} h}{(h-1)^2} \ln\left[1 - \left(\frac{h-1}{\delta_{in} h}\right)(\delta_{in} - \delta)\right] + \frac{\delta_{in} - \delta}{h-1} = -E_m^p \left(\varepsilon_c^p - \varepsilon_d^p\right) \tag{2.23}$$

The stress-strain parameters obtained by the procedures described above should be adjusted by trial and error until a satisfactory fit is obtained. Use the fit parameters as initial values and perform a numerical simulation of the experiment used for the calibration. Compare the numerical fit of the stress-strain response with the experimental one, and adjust the parameters (mainly *h*) until an optimum fit is obtained.

Instead of solving the nonlinear equation (Eq. (2.23)) in order to evaluate *h*, a good initial trial value for steels is

$$40 \le h \le 60. \tag{2.24}$$

Select a value for *h* and then improve it by trial and error.

Figure 2.5 shows an example of a calibration of this constitutive model to monotonic and hysteresis uniaxial stress-strain responses (same material as in Fig. 2.1). The corresponding model parameters are listed in Table 2.5.

Table 2.5 Material parameters for the Tseng-Lee constitutive model.

E Msi (GPa)	σ_{om} ksi (MPa)	σ_y ksi (MPa)	n	σ_o ksi (MPa)	E_c Msi (GPa)	σ_{oc} ksi (MPa)	h
30.3 (209)	11.01 (75.91)	22.10 (152.4)	5.5	39.85 (274.8)	28.5 (196)	18.00 (124.1)	50

2.2.2 Calibrated Material Parameters of Pipeline Steels

The Tseng-Lee [1983] model described above is incorporated in the code REELING to account for the Baushinger effect. The model is calibrated to the experimental cyclic stress-strain responses of the SS- 304 stainless steels used in Chapter 3 using the calibration procedure outlined above. The model parameters for the materials for two tube families used in this study are listed in Table 2.6. The experimental and fitted stress-strain curves are shown in Fig. 2.

Table 2.6 Material parameters for the Tseng-Lee constitutive model.

$\frac{D}{t}$	E Msi (GPa)	σ_{om} ksi (MPa)	σ_y ksi (MPa)	n	σ_o ksi (MPa)	E_c Msi (GPa)	σ_{oc} ksi (MPa)	h
20	30.3 (209)	25.31 (174.5)	36.00 (248.2)	20	39.85 (274.8)	28.5 (196)	18.00 (124.1)	50
15	28.4 (196)	30.70 (211.7)	48.50 (334.4)	21	49.64 (342.3)	27.5 (190)	19.33 (133.3)	80

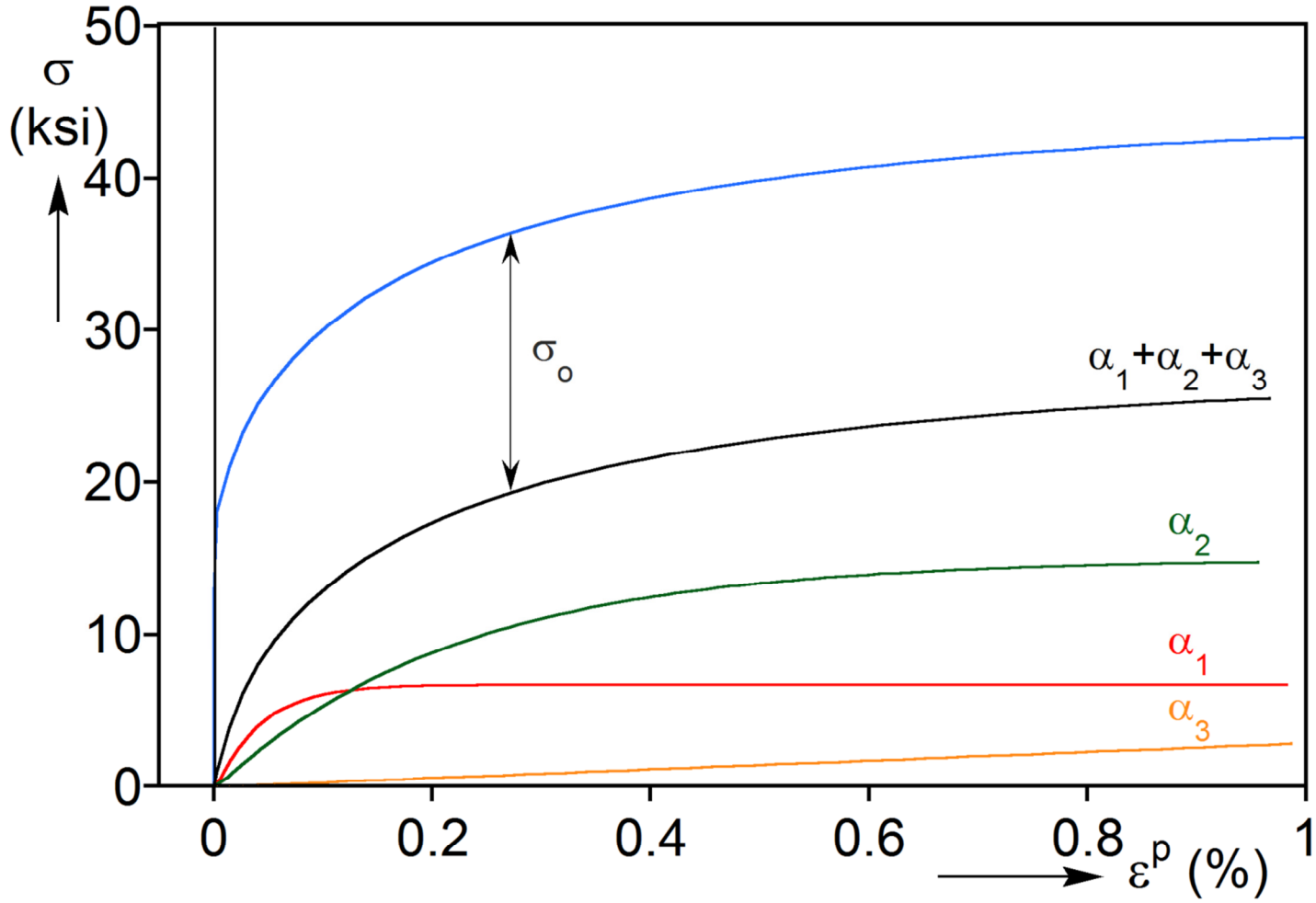

Fig. 2.1 Superposition of three hardening rules of Chaboche model.

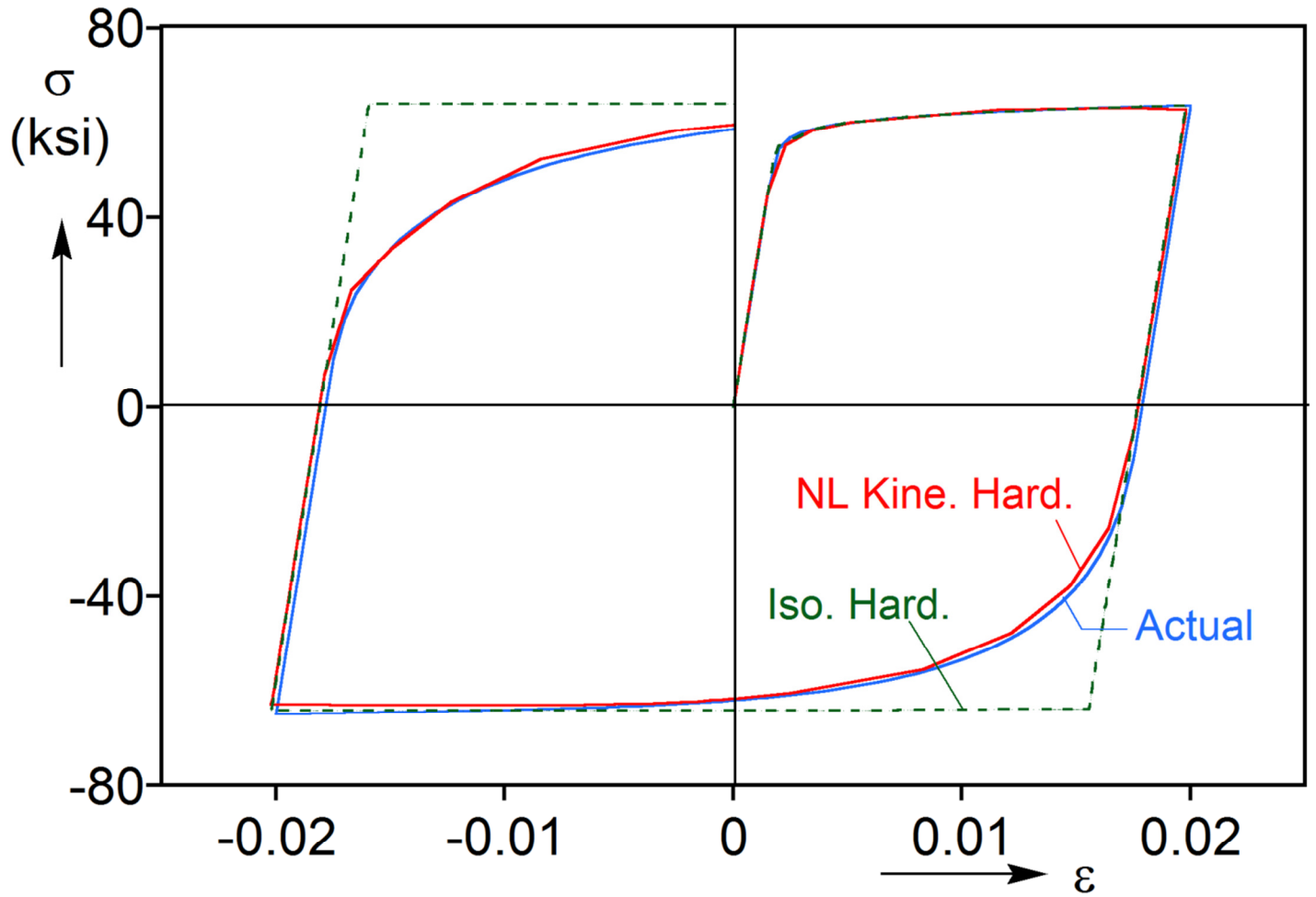

Fig. 2.2 Monotonic and hysteretic stress-strain response of an X-60 steel used and the representations by kinematic and isotopic hardening models.

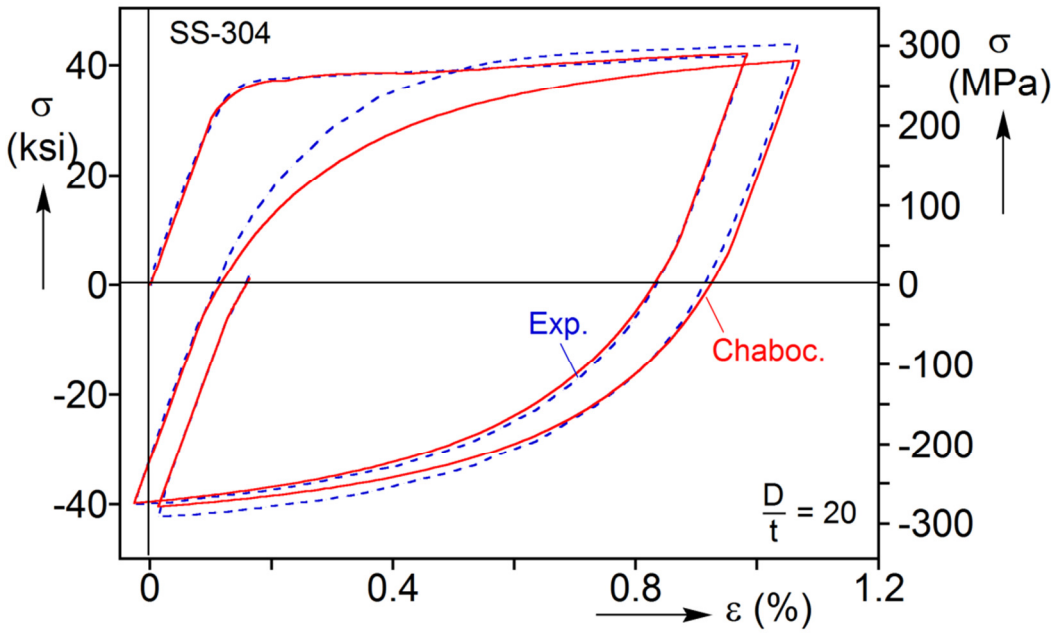

(a)

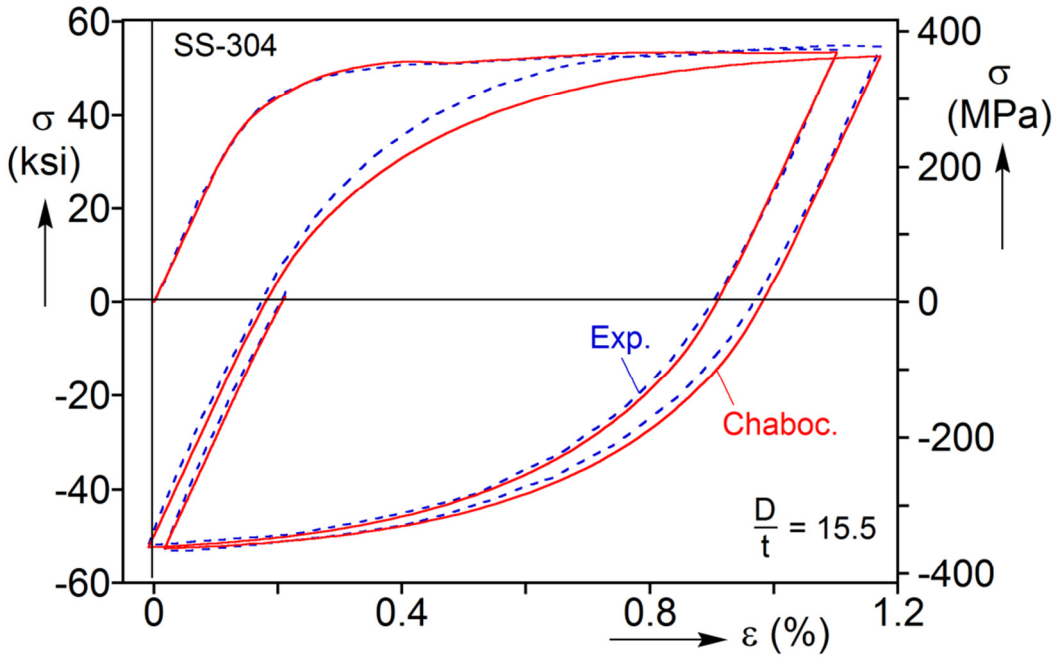

(b)

Fig. 2.3 Cyclic stress-strain response of the SS-304 material used and the fit using the Chaboche model of (a) $D/t = 20$ and (b) $D/t = 15.5$.

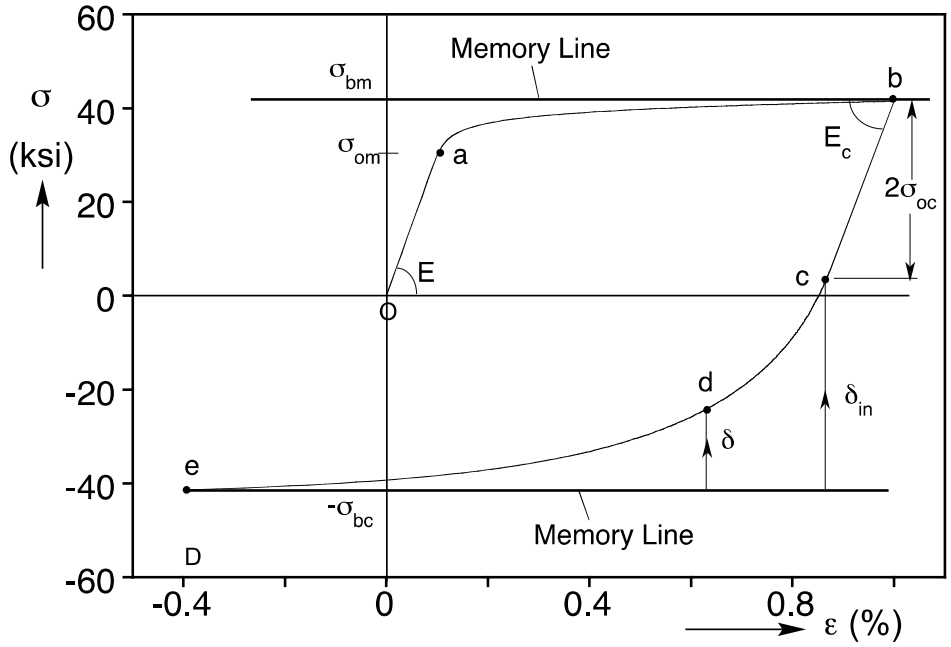

(a)

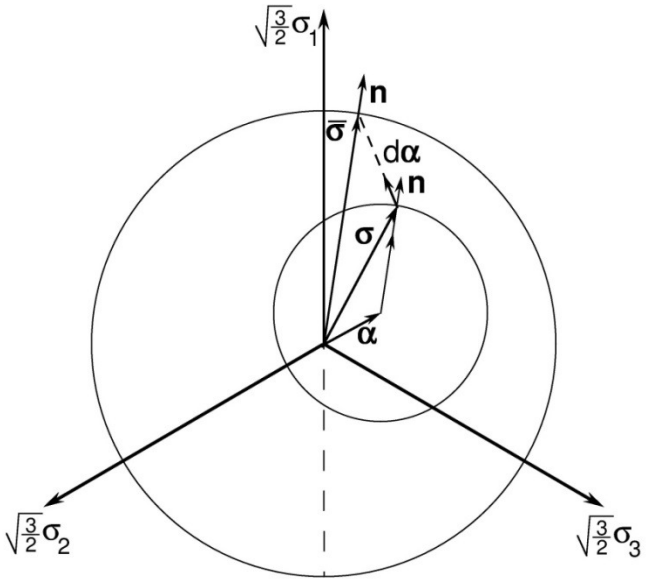

(b)

Fig. 2.4 (a) Uniaxial monotonic and hysteresis stress-strain responses and (b) yield and bounding surfaces of the Tseng-Lee model.

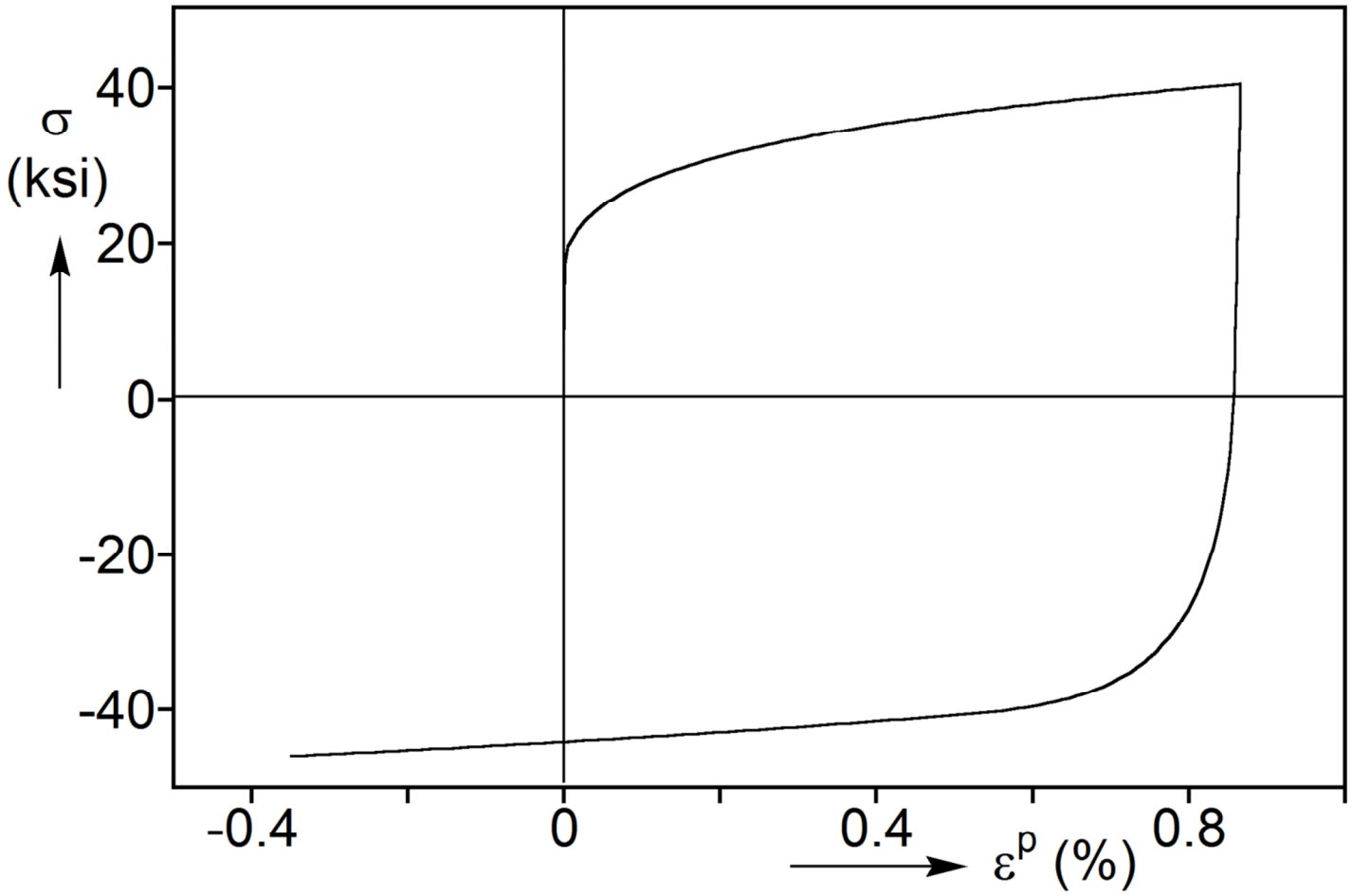

Fig. 2.5 Example of a fitted stress-strain curve using Tseng-Lee model.

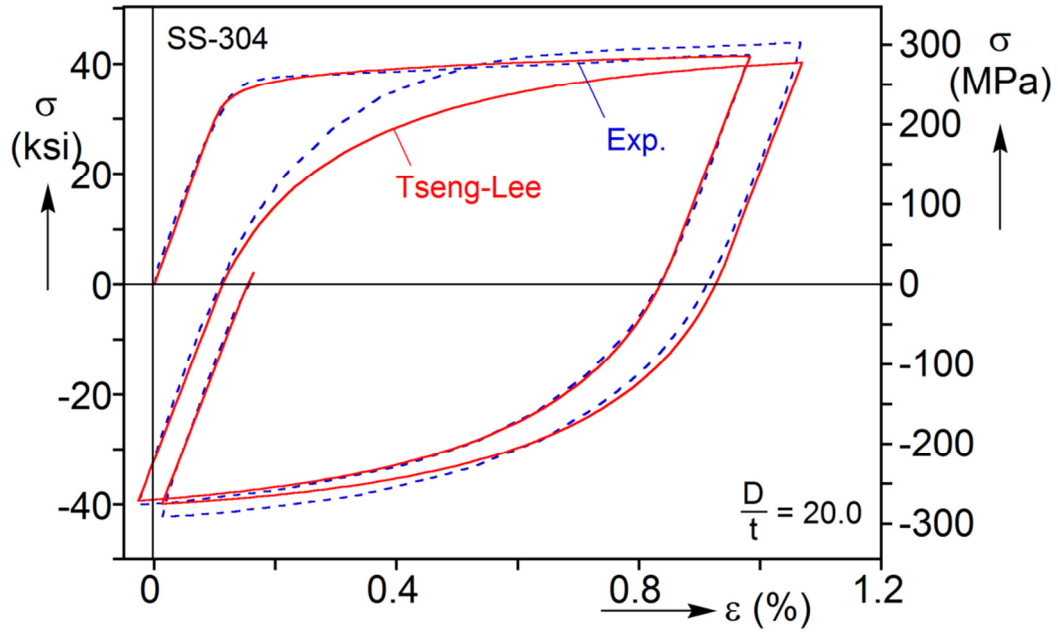

(a)

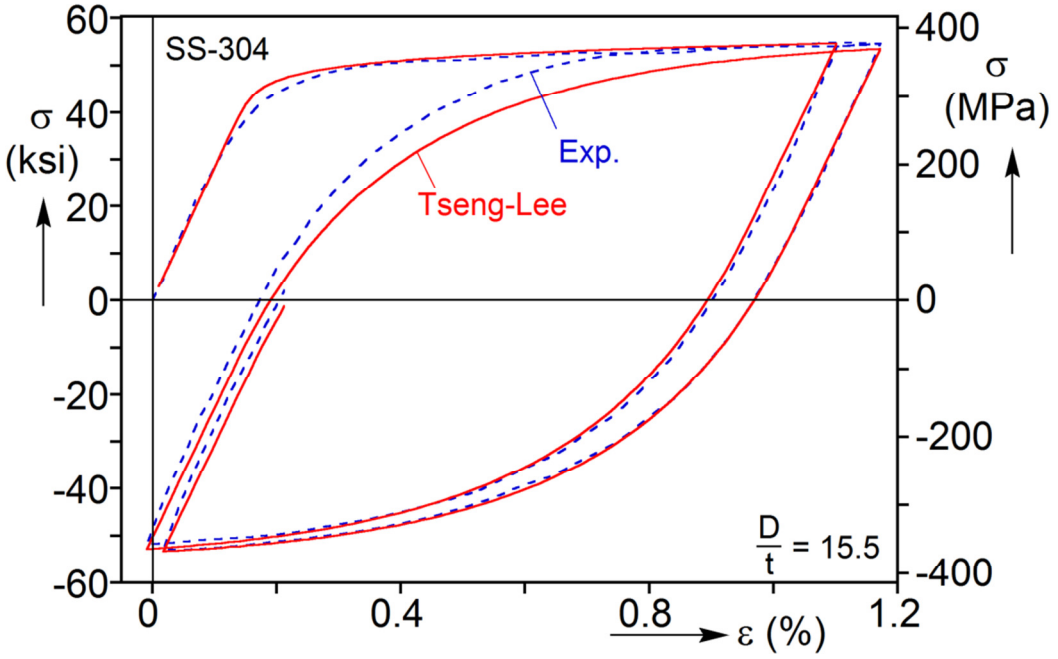

(b)

Fig. 2.6 Cyclic stress-strain response of the SS-304 material used and the fit using the Tseng-Lee model of (a) D/t = 20 and (b) D/t = 15.5

Chapter 3: EFFECTS OF REELING ON PIPE STRUCTURAL PERFORMANCE[1][2]

The reeling installation process involves repeated cycles of bending and straightening that induce bending strains ranging from 1-3%. This cycling bending induces ovality and changes to the mechanical properties that impact the structural performance of the pipeline, particularly so in deeper waters. Kyriakides and Mok [1992] built a unique model reeling facility and used it to examine the structural degradation induced by reeling cycles to tubes wound and unwound at different levels of tension (see also Kyriakides [2017]). This chapter starts with a brief review of the experimental facility and procedures used. Subsequently two models capable of simulating the reeling experiments are presented. The first is a three-dimensional finite element model capable of full representation of the history induced by the winding/unwinding process, in which the inelastic behavior of the material is represented by the Chaboche nonlinear kinematic hardening model. The second model applies the curvature/tension loading history experienced at a point to a section of pipe in contact with a rigid surface of variable curvature. Here the Tseng-Lee constitutive model is adopted. The two models are then used to simulate all the experimental results and the two set of predictions are critically compared.

3.1.1 Reeling Facility

The reeling/unreeling experiments were performed using a model reeling test facility shown in the photograph in Fig. 3.1. The major components of the facility are

---

[1] Liu, Y., Kyriakides, S. (2016). Effect of reeling on pipeline structural performance. *35th Int'l Conf. Ocean, Offshore Arctic Eng.,* OMAE2016-54866, June 2016, Busan, South Korea. (The author implemented the constitutive model, conducted the numerical simulations, and analyzed the results.)

[2] Liu, Y., Kyriakides, S., and Dyau, J.-Y. (2017). Effects of reeling on pipe structural performance—Part II: Analysis. *ASME J. Offshore Mech. Arctic Eng.*, **139**, 051707. (The author implemented the constitutive model, conducted the numerical simulations, and analyzed the results.)

identified in Fig. 3.2. It consists of a 52 in (1320 mm) diameter heavy reel, which is mounted on roller bearings on one end of a stiff frame structure. The reel has a 4 in (102 mm) thick solid steel hub and a 6 in (152 mm) wide outer rim onto which the pipe is wound. The surface of the rim was machined to ensure smooth contact with the tubes during winding.

The reel is rotated using a hydraulic torque motor (capacity 6,000 lb-in—680 N-m) mounted onto the frame as shown in Fig. 3.2. It engages a 43 in (1092 mm) diameter spur gear fixed on the hub of the reel (gear ratio of approximately 6). The test facility was designed to wind and unwind pipe onto the reel at prescribed values of tension, which is achieved as follows. The test specimen, typically 1.0 in (25.4 mm) diameter and about 12 ft (3.66 m) long, is secured onto the reel at one end. The other end is connected via a shackle to a steel wire rope that runs over two pulleys located at the far end of the frame as shown in Figs. 3.1 and 3.2. The loop is closed by connecting the steel cable back onto the reel as shown in the figure. Three turns of the steel cable are pre-wound on the reel, and the end is fixed on the outer rim of the reel. The test specimen-steel cable loop is closed with a 4 in (102 mm) single-ended hydraulic actuator and a load cell (Fig. 3.2). The closed loop is pre-tensioned by contracting the actuator (capacity 10,000 lb—44 kN). The two actuators are powered by a 6 gpm (23 lpm) hydraulic power unit. Independent servo-controlled closed loops are used to prescribe the axial load in the wire/specimen loop and the rotation of the reel.

The frame was constructed out of 8 x 6 in (200 x 150 mm) rectangular steel tubes and rests in a horizontal position on four legs. The overall length of the test facility is 20 ft (6 m). The distance between the axis of the reel and those of the pulleys is 16 ft (4.88 m). The facility is surrounded by a safety cage. More details about the design of the facility can be found in Kyriakides and Mok [1992].

3.1.2 Experimental Procedure

The experimental results reported here involve 1.0 in (25.4 mm) diameter seamless stainless-steel (SS) 304 tubes with D/ts of about 20 and 15.5. The experiments fall into two categories: (a) three cycles of wind/unwind/straighten at prescribed tension; and (b) one cycle of wind/unwind/straighten followed by collapse under external pressure. Winding a pipe diameter D onto a reel radius ρ plasticizes the line to a bending strain of

$$\varepsilon_b = \frac{D}{(2\rho + D)}. \tag{3.1}$$

In accordance with Eq. (3.1) winding an 1-inch tube on the model reel induces a bending strain of 1.886%.

The objective of these experiments was to establish how repeated cycles of reeling, unreeling and straightening a pipe at a given value of tension affect its geometric integrity. Thus, test specimens were pre-loaded to a selected value of axial tension and were subsequently wound and unwound onto the reel three times while the axial tension was kept constant by the closed-loop tension controller.

During these experiments, the applied tension was recorded as a function of the angle of rotation ϕ of the reel. A custom-built transducer, shown in Fig. 3.3, was used to monitor the change in the diameter of the tube in the plane of bending, at a point located approximately at the mid-length of the test specimen. After each cycle was completed, the change in diameter at different positions along the length of the test specimen was measured manually, using a micrometer, and recorded. The axial strain induced to a test specimen during reeling was monitored by a pair of strain gages bonded to the tube at approximately the same position as the transducer measuring the change in diameter of the tube (see Fig. 3.3).

A second objective of these experiments was to establish the degradation in the collapse pressure of pipe as a result of reeling. Sixteen such experiments were performed using similar SS-304 tubes with D/t values of approximately 20 and 15.5. The test specimen preparation and experimental procedure followed were the same as described above. After one wind/unwind/straighten cycle, the change in diameter in the plane of bending and the ovalization

$$\Delta = \frac{D_{\max} - D_{\min}}{D_{\max} + D_{\min}} \tag{3.2}$$

of the cross section were measured manually at intervals of 6 in (152 mm) along the length of the test specimen. A section, usually 36D long, was then cut from the central part of the reeled section of tube. After sealing the ends, the tube was collapsed under external pressure and the collapse pressure was recorded. Varying the tension applied during winding and unwinding resulted in different values of residual ovality. The collapse pressure of as received pipe was also established experimentally in separate experiments.

The geometric characteristics of the test specimens used in the second group of experiments, the applied tension, the initial and residual ovalities Δ_o and Δ respectively, and the collapse pressure, P_{CO}, is normalized by the yield pressure defined as

$$P_o = \sigma_o \frac{2t}{(D-t)}. \tag{3.3}$$

3.1.3 Experimental Results

We start with results from a representative experiment involving a tube with $D/t \approx 20$ wound/unwound at a tension of $0.11T_o$. Figure 3.4 depicts a sequence of photographs that show the progression of a 12 ft (3.65 m) long tube as it is wound onto the reel (images ①-⑤) and then unwound (images ⑥-⑨). Although the applied tension is

relatively small, the unwound section of the pipe remains essentially straight during both winding and unwinding.

During winding, the end of the tube connected to the cable via the shackle is seen in images ①-⑤ in Fig. 3.4 to move closer to the reel. Concurrently, an equal length of wire rope is unwinding from the reel. As a result, the actuator/load cell assembly that rides on rollers on the floor is seen to be gradually rolling away from the reel. In ⑤, the shackled end of the tube has reached the reel while the actuator/load cell assembly has rolled out of the field of view. Image ⑥ shows the specimen during the early part of unwinding and images ⑦-⑨ at more advanced stages. As unwinding proceeds, the actuator trolley is seen to roll back towards the reel. Because of the applied tension, most of the tube straightens as it unwinds. An approximately 12D long section at the end of the tube did not come into full contact with the reel during the winding and as a result is seen to be pointing downwards during unwinding. Typical reeling and unreeling rates were approximately 36D per minute. The corresponding bending strain rate is approximately $\dot{\varepsilon}_b = 5.66\times10^{-2}\,\mathrm{s}^{-1}$. The second and third cycles were performed in a similar manner.

The effect of reeling/unreeling cycles on the pipe cross section will be illustrated using experimental results shown in Fig. 3.5. Plotted are the tension-rotation history (Fig. 3.5a), and the change in diameter- and strain-rotation histories (Figs. 3.5b, 3.5c), both variables measured at mid-length. The tube diameter remains unchanged until point A gets very close to the reel. As its neighborhood bends to conform to the reel curvature, ΔD undergoes a sharp increase. A small overshoot is recorded, presumably associated with the point of contact, following which the local ovalization remains constant during the rest of the winding cycle. ΔD remains also constant during the first part of unwinding but starts to decrease as point A detaches from the reel and starts to straighten. This is preceded by a small transient probably associated with the moment of lift off. The cycle

leaves a permanent ovality to the straightened pipe, depicted as ΔD_1 in Fig. 3.5b. The process is repeated with each subsequent cycle so that the residual ovality grows to ΔD_2 after cycle 2 and to ΔD_3 after cycle 3. It is interesting to observe that the first cycle introduced a larger value of residual ovality than the subsequent two cycles. Furthermore, the transition from one ovality plateau to the next is larger for unwinding as compared to winding for all cycles. Although cyclic bending even at zero tension results in permanent ovalization of the tube cross section (see Kyriakides and Shaw [1987], Corona and Kyriakides [1991]), in the experiments that follow it will be demonstrated that the residual ovality increases significantly as the winding/unwinding tension increase.

The axial strain measured at point A during the three cycles is plotted against the reel rotation angle ϕ in Fig. 3.5c. The strain associated with the pre-tensioning of the tube (ε_o) is elastic and small, and consequently does not register in the scale of this plot. It remains constant until the neighborhood of point A starts to bend. Bending plastically deforms the pipe reducing its axial rigidity. Thus, by the time this section of tube conforms to the curvature of the reel, it has undergone significant axial stretching. Once the section comes in full contact with the reel the axial strain does not change. It also remains unchanged during the initial stages of unwinding but starts to increase again as the neighborhood of A starts to straighten. Straightening plastically deforms the tube again and the axial rigidity is reduced, causing the axial strain to increase once more. As this section of tube straightens, the axial strain stabilizes at the value of ε_1. The same process is repeated during each half cycle so a permanent elongation of ε_2 is recorded after the second cycle and ε_3 after the third. In summary then, the strain increases (ratchets) both during winding and unwinding (to be contrasted with the change in ΔD). As was the case for ΔD, the largest increase in axial strain occurred during the first cycle.

Subsequent experiments will demonstrate that the rate of strain ratcheting is strongly dependent on the applied tension.

3.2 Modeling and Analysis

3.2.1 Three-Dimensional Finite Element Model

A three-dimensional (3-D) model of the complete wind/unwind history is developed within the nonlinear code ABAQUS. The reel is represented as a circular rigid surface with a radius ρ. A $160D$ long section of pipe is connected to the reel as shown in Fig. 3.6. The other end of the pipe is placed between rollers that prevent vertical but allow horizontal motion of the line. A constant tension force (T) is applied on the left end, and the line is wound by applying incrementally a rotation, ϕ, to the reel. The pipe is unwound by reversing the direction of rotation until ϕ is back to zero while the level of the back tension is maintained. (A similar model in is used in Chapter 4 to study the effect of pipe discontinuities on the integrity of reeled pipe— see also Liu and Kyriakides [2014].)

The pipe consists of a starter section $15D$ long, a "test section" $15D$ long, and a $130D$ trailing section. The pipe is assumed to deform symmetrically about the plane of bending so only half of the cross section is modeled with S4 shell elements. Of main interest are the stresses and deformations induced by the wind/unwind process to the test section. To capture this with accuracy a finer mesh is adopted for the test section; it is assigned 20 elements around the half-circumference and 20 elements per pipe diameter axially. The other two sections have the same circumferential mesh distribution but only one element per diameter axially. The two mesh densities were determined using convergence studies.

The reel is modeled as an analytical rigid surface. Contact with the deformable pipe is modeled using a strict "master-slave" algorithm of ABAQUS, with the reel surface as the master and the pipe as the slave surface. The contact is frictionless but "finite sliding" is allowed between a contact pair. An exponential "softened" contact pressure-overclosure relationship is used with 500 psi (3.4 MPa) and 0.0001 in (0.00254 mm) being representative pressure and clearance values respectively. The nonlinear kinematic hardening constitutive model of Chaboche [1986] incorporated in the code of ABAQUS is used for the simulations. The model and its calibration are outlined in Chapter 2.

3.2.2 Two-Dimensional Model (REELING)

Offshore pipeline installation processes involve significant lengths of pipe often in the km range. In many such applications, the variation of bending, tension and pressure along the length is small enough so that the structure can locally be considered to be axially uniform. Such an assumption reduces the problem to a two-dimensional one. This, for example, is the philosophy behind the computer code BEPTICO which is a main tool for establishing limit states of buckling and collapse under bending, tension, and pressure (see Kyriakides and Corona [2007]). In the same spirit, if in the reeling/unreeling process of interest is limited to the changes induced to the pipe cross section by the wind/unwind process, then a good approximation can be obtained using the two-dimensional (2-D) code REELING. This is a custom numerical analysis, similar to BEPTICO, in which a pipe is bent under tension over a rigid surface uniformly. A long section of pipe under tension, T, in contact with a rigid surface (see Fig. 3.7) is gradually bent by increasing the curvature, κ, of the contact surface (the formulation and the treatment of contact are described in Ch. 10 of Kyriakides and Corona, 2007). Thus, the winding of a pipe on a

reel is accomplished by progressively increasing κ until the pipe acquires the curvature of the reel. Unwinding is achieved by gradually reducing the curvature to zero or to a negative value. In the code REELING the Baushinger effect is accounted for through the Tseng-Lee [1983] two-surface nonlinear kinematic hardening model summarized in Chapter 2. The calibration of the constitutive model to the pipe materials used is also described in the same chapter.

3.3 Simulation of Reeling and Unreeling

The two models are now used to simulate the reeling and unreeling of pipes under constant values of tension. The main problem parameters that will be used in the analyses are listed in Table 3.1. They approximately correspond to average values of each family of tubes used in the experiments reported in Section 3.1; i.e., 1-inch tubes with D/t = 20 and 15.5 wound onto a 26-inch (660 mm) radius reel. This combination induces a bending strain of 1.89% to the tubes.

Table 3.1 Main geometric and material parameters of tubes analyzed

$\frac{D}{t}$	D in (mm)	t in (mm)	ρ in (mm)	E Msi (GPa)	σ_o ksi (MPa)
20.0	1.00 (25.4)	0.050 (1.27)	26 (660)	30.3 (209)	38.5 (266)
15.5	1.00 (25.4)	0.0645 (1.64)	26 (660)	28.4 (196)	49.6 (342)

We will first analyze in detail the reeling of a tube with D/t = 20 wound and unwound at a tension $0.075T_o$. The case will also be simulated with the 2-D model and the induced moment, ovality and elongation will be compared with the corresponding 3-D results.

3.3.1 Three-Dimensional Model Results

The three-dimensional (3-D) model is used to simulate a complete wind/unwind cycle. Figure 3.8 shows five full-scale pipeline deformed configurations from such a cycle. For clarity the $15D$ long test section is colored in red. Tension of $0.075T_o$ is applied to the free end of the line at the start of the winding and is held constant for the rest of the process. The model reel is then incrementally rotated. Thus, for example, in configuration II the starter section and part of the test section have come into contact with the reel and conformed to its circular surface. Rotation continues until $\phi = 120^\circ$, in the process bringing into contact a tube length of $55.5D$ (conf. III). The reel is then incrementally rotated back reducing ϕ (cong. IV). This causes the plastically bent section to nearly straighten as illustrated in conf. V ($\phi = 0$). Figure 3.9 shows expanded views of the pipe test section (between two lines "|") as it engages the reel during the winding (images ①-④) and disengages during unwinding (images ⑤-⑧). The solid dot identifies the position of the center of the test section (point A in Fig. 3.6). The superimposed contours represent the induced axial strain. They show the top of the tube to be stretched and the bottom compressed.

Figure 3.10 shows the evolution of five major problem variables with the rotation angle, ϕ, during the wind/unwind cycle, calculated at section A of the fine mesh test section. They are: (a) the normalized moment acting on the section (M / M_o); (b) the normalized local curvature (κ / κ_1); (c) the contact pressure (p_{co}); (d) the normalized change in diameter in the plane of bending ($\Delta D / D \approx$ ovality); and (e) the mean axial strain (ε_x) (where $M_o = \sigma_o D_o^2 t$, $\kappa_1 = t / D_o^2$, $D_o = D - t$). The values of the five variables corresponding to the eight deformed configurations in Fig. 3.9 are marked on the responses with numbered bullets: ①-④ correspond to the loading half of the cycle and ⑤-⑧ to the unloading half. (The curvature, κ, is calculated using a three point

centered average of the deformed coordinates of element nodes at the mid-surface of the shell. The moment is calculated as follows: $M = 2\sum_{i=1}^{N} z_i F_i$ where F_i is the axial force acting on the ith node on the cross section and z_i is its distance from the mid-surface of the tube.)

When the reel starts rotating, the suspended pipe next to it arches upwards and the induced curvature (Fig. 3.10b) affects the test section, causing the moment at A to gradually increase as shown in Fig. 3.10a. Simultaneously, the ovality and axial strain experience small growths (Figs. 3.10d and 3.10e). By station ①, section A has approached the reel (see Fig. 3.11a) causing further bending. The pipe is plasticized and the ovality and axial strain experience an upswing (Figs. 3.10d and 3.10e). Section A comes into contact with the reel at station ② at a rotation of 55.8°, and simultaneously a sharp local spike in the contact pressure develops as illustrated in Fig. 3.10c. This also corresponds to the maximum moment developed at section A. By station ③, the contact pressure drops down to a low level, the curvature reaches the value that corresponds to that of the reel and subsequently remains constant until unwinding commences. Despite this, the moment experiences a gradual decrease. Between stations ① and ③, the ovality and axial strain undergo a significant increase. Both reach their maximum values of $\varepsilon_x =$ 0.177% and $\Delta D / D =$ 1.54% by station ③ at $\phi \approx 60^\circ$, and remain constant during the rest of the winding. By contrast, the moment continues to drop due to some elastic unloading.

During unwinding, the moment at section A gradually increases while the curvature, ovality, axial strain, and contact pressure remain unchanged until section A approaches liftoff (⑥ in Fig. 3.9). As lift off the reel is approached, a new smaller spike in contact pressure develops and the moment reaches a local maximum. At $\phi \approx 85.8^\circ$

(⑥), section A lifts off the reel and starts moving away from it. Again, a bent transition zone develops closer to the reel within which the curvature decreases. The moment drops first to zero and then becomes negative due to the straightening imposed by the tension (note that the curvature is essentially zero at the end of unwinding). Between stations ⑥ to ⑧, ovality decreases with ϕ changing only modestly beyond ⑧ finishing at a value of about 0.72%. By contrast, ε_x increases because of the re-plasticization imposed by the reverse bending, finishing at a value of 0.24% (such an increase was also observed in the experiments in the experiments as shown in Fig. 3.5).

The contact pressure that develops between the pipe and the reel at first contact during winding, and at the time of detachment during unwinding, is examined in more detail in Fig. 3.11. Shown are two deformed configurations of the neighborhood of section A, with color contours of axial strain superimposed. In these configurations the process is considered to be in a "steady-state," so the numbered bullets correspond to the positions section A would be at the numbered stations marked in the responses in Fig. 3.10. During winding, the reel is rotating in a clockwise manner and the three bullets in Fig. 3.11a correspond to the position of section A as it approaches the reel (bullet ①), at the time of first contact (bullet ②), and shortly after contact (bullet ③). The contact pressure is seen to develop a sharp spike at the time section A engages the reel, which decays down to a small value within a distance of about one tube diameter. It is worth pointing out that this distribution of contact pressure is captured because of the 3-D nature of this calculation. In simpler beam representations of the pipe, contact is limited to a single reaction force at the point of touchdown (limitation imposed by the "plane sections remain plane" assumption). During unwinding, represented by Fig. 3.11b, section A is approaching the point of liftoff from the right (bullet ⑤), lifts off at ⑥, and gradually departs from the reel (bullet ⑦). The contact stress gradually grows from point

⑤, reaches a maximum value just before lift off at ⑥, and drops to zero there after. The transition zone is now longer, covering a length of about 6D.

3.3.2 Two-Dimensional Model Results

Because of its simplifying assumptions, the two-dimensional (2-D) model does not capture the transients experienced by a pipe section as it is coming in and out of contact with the reel. Instead, "winding" is simulated by the bending of the pipe over a rigid surface, which is achieved by gradually increasing its curvature until the value corresponding to the curvature of the reel is reached. "Unwinding" is simulated by gradually reducing the curvature to zero. In the process the evolution of the cross sectional variables is monitored. Figure 3.12a shows the calculated moment-curvature response during such a wind/unwind cycle with the addition of an unloading step at the end. Figure 3.12b plots the induced change in diameter $(\Delta D / D)$ and axial elongation (ε_x) with curvature. The $M-\kappa$ response exhibits the expected hysteretic behavior. The cycle induces bending to a normalized curvature of $0.681\kappa_1$, unloading, reverse loading to zero curvature, and finally removal of the moment, ending up with a small residual curvature. The ovality grows nonlinearly with curvature during the reeling phase, and decreases nonlinearly during the unloading and reverse bending phase (e.g., see Kyriakides and Shaw [1987], Corona and Kyriakides [1991]). The axial strain grows nearly linearly during reeling and continues to grow nonlinearly during the unloading/reverse loading phase.

Figure 3.13 shows corresponding plots of the evolution of the same variables at section A with curvature extracted from the 3-D calculation. The moment-curvature history is nearly identical to that of the 2-D analysis but for the elastic unloading experienced as the section moves around the reel during winding (the final unloading was

not performed for 3-D). The trajectory of $\Delta D / D$ is qualitatively similar but the values predicted by the 3-D model are generally larger. For example, the value at the end of the cycle is about 40% larger for the 3-D case. Ovality has been shown in the past to be sensitive to the hardening direction adopted in the kinematic hardening model (see Corona and Kyriakides [1988], Kyriakides et al. [2004]). Consequently, the difference in $\Delta D/D$ between the 2-D and 3-D simulations is at least partly caused by the different hardening directions of the two constitutive models. The somewhat different stress history induced by the 3-D process is another contributor thought to be secondary. The axial elongation on the other hand is both qualitatively and quantitatively comparable to that of the 2-D model.

3.3.3 Three Wind/Unwind Cycles

In the experimental study of Kyriakides and Mok [1992] summarized in Section 3.1, the tubes were wound/unwound onto the reel three times at prescribed constant values of tension. As mentioned in the introduction, in most reeling vessels the pipe experiences at least two such cycles. It was thus desirable to establish a trend on the degrading effect of repeated cycles on the structure. In the same spirit we extended the simulations of the base case analyzed in Section 3.3.1 to three cycles all performed at the same tension of $0.075T_o$. The pipe is again wound by rotating the reel clockwise by 120^o, and unwound by rotation back to zero degrees.

Figure 3.14 shows the evolution of four of the variables at section A in the test section with the rotation angle, ϕ. Since the tube was not unloaded at the end of each cycle, the second and third cycles start from different initial conditions. Consequently, for these two cycles the moment during winding is seen in Fig. 3.14a to follow a somewhat lower trajectory than that in the first cycle while the unloading path is nearly identical for

all three cycles (the different shapes of the initial monotonic stress-strain response and the hysteretic one contributes to this difference also). In Fig. 3.14b a small difference in the winding trajectories of curvature between the first and subsequent cycles is also observed, primarily for the same reasons. These differences are also reflected in Fig. 3.15a that plots the moment vs. the curvature, with the winding part of the first cycle being different.

Figure 3.14c shows the evolution of change in diameter in the plane of bending. The second and third cycles trace similar trajectories as the first cycle but the residual $\Delta D / D$ is smaller (cycles 1, 2, 3: 0.72%, 1.21%, 1.67%). It is reassuring that the shapes of these trajectories are very similar to those recorded in one of the reeling experiments reported in Fig. 3.5. $\Delta D / D$ is plotted against the curvature in Fig. 3.15b, which presents an alternate view of the cyclic accumulation of this variable (see Kyriakides and Shaw [1987], Corona and Kyriakides [1991]).

Figure 3.14d plots the evolution of axial strain vs. the reel rotation. Here also the trajectories of the second and third cycles are similar to the first cycle with the tube elongating both during the winding and unwinding halves of each cycle. The accumulated strain is, however, much smaller in cycles 2 and 3 than in cycle 1 (cycles 1, 2, 3: 0.24%, 0.33%, 0.41%). These results again mimic those of the experiment in Fig. 3.5. The axial strain is also plotted against curvature in Fig. 3.15b. The results again confirm that elongation takes place every time the section undergoes plastic bending.

The three wind/unwind cycles were also simulated using the REELING code. The calculated moment, ovality and elongation are plotted against curvature in Fig. 3.16. The moment-curvature response (Fig. 3.16a) is essentially identical to that from the 3-D analysis in Fig. 3.15a (less the temporary unloading while on the reel). The ovality follows a similar trajectory with curvature (Fig. 3.16b) as that in Fig. 3.15b producing a

somewhat faster rate of growth (Corona and Kyriakides [1988], Kyriakides et al. [2004] noted the sensitivity of calculated ovality to the constitutive model). The axial elongation-curvature trajectory is similar to that of the 3-D plot both qualitatively and quantitatively.

The 3-D and 2-D models were subsequently used to simulate the whole set of three reeling cycle experiments under varying tension levels reported in Section 3.1 for the two D/t tube families. Once again the "average" mechanical properties of each family of tubes are adopted. Figure 3.17a shows the changes in diameter plotted as a function of tension after the first, second and third cycles for the $D/t \approx 20$ tube family. Included are the corresponding measured results. The results from the two models show nearly constant rates of increase over the three cycles. The two sets of predictions agree well for cycle 1 and they are also in very good agreement with the experimental values. For cycle 2 the 3-D predictions are somewhat higher than the 2-D ones, but the difference spans the scatter in the experimental data. For cycle 3 the difference between the two predictions increases further with the 2-D results being closer to the experimental data.

Figure 3.17b plots the corresponding axial strain predictions vs. tension together with those measured. The two sets of predictions are nearly identical but some differences are observed with the experimental data. The predictions follow the experimental trend for the first cycle, but overestimate those of the second cycle and even more so the third. The prediction of axial ratcheting requires that the evolution of the open hystereses recorded in cyclic experiments be reproduced very accurately (see Hassan and Kyriakides [1992], Jiao and Kyriakides [2009]). The stress-strain results in Figs. 2.3 and 2.6 for the $D/t \approx 20$ tube material show that both models did not reproduce very well the forward half of the hysteresis, which can lead to the discrepancy observed in Fig. 3.17b. The experimental data for the lowest tension of $0.037T_o$ are out of line

with the numerical results. Because of the age of the experiments, we speculate that in this experiment perhaps the bridge was not properly zeroed at the onset of reeling.

Corresponding results and comparisons to the experiments for the $D/t \approx 15.5$ family of tubes appear in Fig. 3.18. The relationship of the 2-D and 3-D prediction is similar to that in Fig. 3.17 with the two sets of predictions being quite close for cycle 1, becoming increasingly more divergent for cycles 2 and 3. The two predictions of the $\Delta D/D - T/T_o$ are in good agreement with the experimental results for cycle 1, the 3-D predictions are closer to the experimental data for cycle 2, whereas for cycle 3 the data falls between the two predictions. Both sets of prediction of the axial strain-tension are in good agreement with the data for the first cycle, but the data for the second cycle are overpredicted somewhat and more for the third cycle.

Overall, the performance of the two models is good for the prediction of the ovality and the accumulated axial strain for cycle 1, reasonably good for cycle 2, but diverges from the data for cycle 3. Improving this performance requires more detailed calibration of the constitutive model to the axial ratcheting behavior of the steel to higher strains.

3.4 Collapse Pressure of Reeled Pipe

In this section the two models are used to simulate the experiments reported in Section 3.1 in which tubes first underwent one reeling/unreeling cycle at various tension levels. After the geometric changes to the cross section were recorded, the tubes were collapsed under external pressure. The simulations of the reeling/unreeling cycles are performed as described in Sections 3.2.1 for the 3-D model and 3.2.2 for the 2-D model, using the average geometric and material parameters of each tube family. The calculated residual changes in diameter in the plane of bending ($\Delta D/D$) for the $D/t \approx 20$ tubes are

plotted against the applied tension in Fig. 3.19a together with the measured values. For both models the predicted residual change in diameter increases nearly linearly with tension. The experimental values exhibit a similar trend and are generally in good agreement with both predictions.

The base case example of a 1-inch diameter tube with D/t = 20.0 wound and unwound on the model reel under a tension of $0.075T_o$ will be used to illustrate how the influence of the reeling process on the pipe collapse pressure was established. Starting with the 3-D model, before the reeling is commenced the $15D$ long finer mesh test section is enclosed within a cavity of fluid elements (ABAQUS F3D4, F3D3) as shown in Fig. 3.20a. The tube is then wound and unwound onto the reel with the fluid elements remaining inactive. In this particular case, the process left a residual ovality of $\Delta_o = 0.538\%$. A $13D$ long section is then removed from the center of the fine mesh test section and its ends are sealed with thick shell elements. The deformed geometry is maintained but the stress history and residual stresses are removed and the structure is assigned the initial monotonic material stress-strain response. The tube is then pressurized by prescribing incrementally the change in volume of fluid in the cavity (δv) until the tube collapses.

Figure 3.20b shows the calculated pressure-change in volume response (P_o is the yield pressure defined in Eq. (3.3)). It has the usual characteristics with an initial stiff nearly linear response that eases into a pressure maximum at $0.725P_o$. Beyond this point the structure collapses with a local profile that is about $6D$ long as described in Chapter 4 of Kyriakides and Corona [2007]. It is interesting to compare this value with the collapse pressure of the intact tube. It had an initial ovality of 0.128% and registered a collapse pressure of $0.819P_o$; thus reeling under a tension of $0.075\,T_o$ caused a degradation of about 13%.

The single cycle reeling was also simulated with the 2-D model. In this case the residual ovality was Δ_o = 0.496%. This ovality is used as input in BEPTICO to calculate the collapse pressure. The structure is again assumed to be stress free and the initial monotonic part of the stress-strain response is adopted. The collapse pressure is estimated to be $0.740P_o$, which compares with the BEPTICO predicted value of $0.833P_o$ for the tube before reeling. Both collapse pressures, although in reasonable agreement with the 3-D model, are somewhat higher. The main cause of the difference in the collapse pressure of the reeled pipe is the difference in the calculated reeling induced ovality. As mentioned earlier, this difference is caused first by the simpler load/unload history of the 2-D model and by the different constitutive models adopted.

The two models were used to predict the collapse pressures of the tube reeled/unreeled at several different values of tension. The predicted collapse pressures are plotted vs. tension in Fig. 3.19b together with the measured collapse pressures. Both sets of predicted collapse pressures follow the trend of the experiments very well both qualitatively and quantitatively. Overall the results demonstrate the detrimental effect that reeling can have on collapse pressure.

The same procedure was used to reel/unreel tubes with $D/t \approx 15.5$ at different levels of tension. The resultant change in diameter in the plane of bending is plotted against tension in Fig. 3.21a. The predicted $\Delta D / D$ again grows nearly linearly with tension, for both models. The 3-D model produces somewhat higher values than the 2-D model that are closer to the measured values.

The corresponding collapse pressures are plotted against tension in Fig. 3.21b. The two sets of predictions exhibit a similar decreasing trend of P_{CO} with tension as the experimental results with the 2-D collapse pressures being somewhat higher. This of course is a direct consequence of the lower predicted ovality by the 2-D model. The 2-D

model predicted collapse pressures are closer to the measured values for lower tension levels and the 3-D results are closer for the higher tensions. We close this section by pointing out that for this relatively low *D/t* of about 15.5 the shell representation of the tube using S4 elements in the 3-D model may be responsible for the larger difference between the 2-D and 3-D predictions observed here. A solid element model should provide a more accurate representation of low *D/t* structures.

3.5 SUMMARY

This chapter has presented two models for establishing the sectional geometric and material changes induced to a pipeline by repeated reeling/unreeling cycles. The first model involves a large-scale computationally intensive 3-D finite element model and the second is a computationally efficient 2-D model. Both models were shown capable of capturing the induced changes in the cross sectional geometry and mechanical properties. The ovality and axial elongation induced at different levels of tension were reproduced by both models with good accuracy for the first cycle, less accurately for the second cycle while the results for the third cycle were generally overpredicted. The predictions for the tubes with D/t ≈ 20 were more accurate than those of the D/t ≈ 15.5 tubes.

It is worth mentioning that the range of tension levels considered in this study includes values that are significantly higher than those used in most current reeling operations. This induced larger values of ovality and elongation than expected from a normal two bending cycle reeling/unreeling process. This in turn allowed evaluation of the two models over a broader range of parameters. Larger than normal ovality values can, for example, result from off-design scenaria in which an installed pipeline is recovered and subsequently reinstalled, in the process undergoing additional reeling/unreeling cycles.

A consequence of the larger tension levels used in the experiments and analysis is larger excursions into the plastic range than the strain range of the cyclic stress-strain measurements used to calibrate the two plasticity models. This is thought to be responsible for the over-prediction of the ovality and elongation during the third reel/unreel cycle. Improved performance by the models requires that the constitutive models be calibrated to strain levels that correspond to those reached in the reeling experiments. It is also worth pointing out that SS-304 hardens under cyclic loads. This hardening was not accounted for in the two cyclically stable constitutive models used, which may have also contributed to the over-prediction of the sectional variables in the third reeling cycle. The main conclusions drawn from this study appear in Section 6.1.

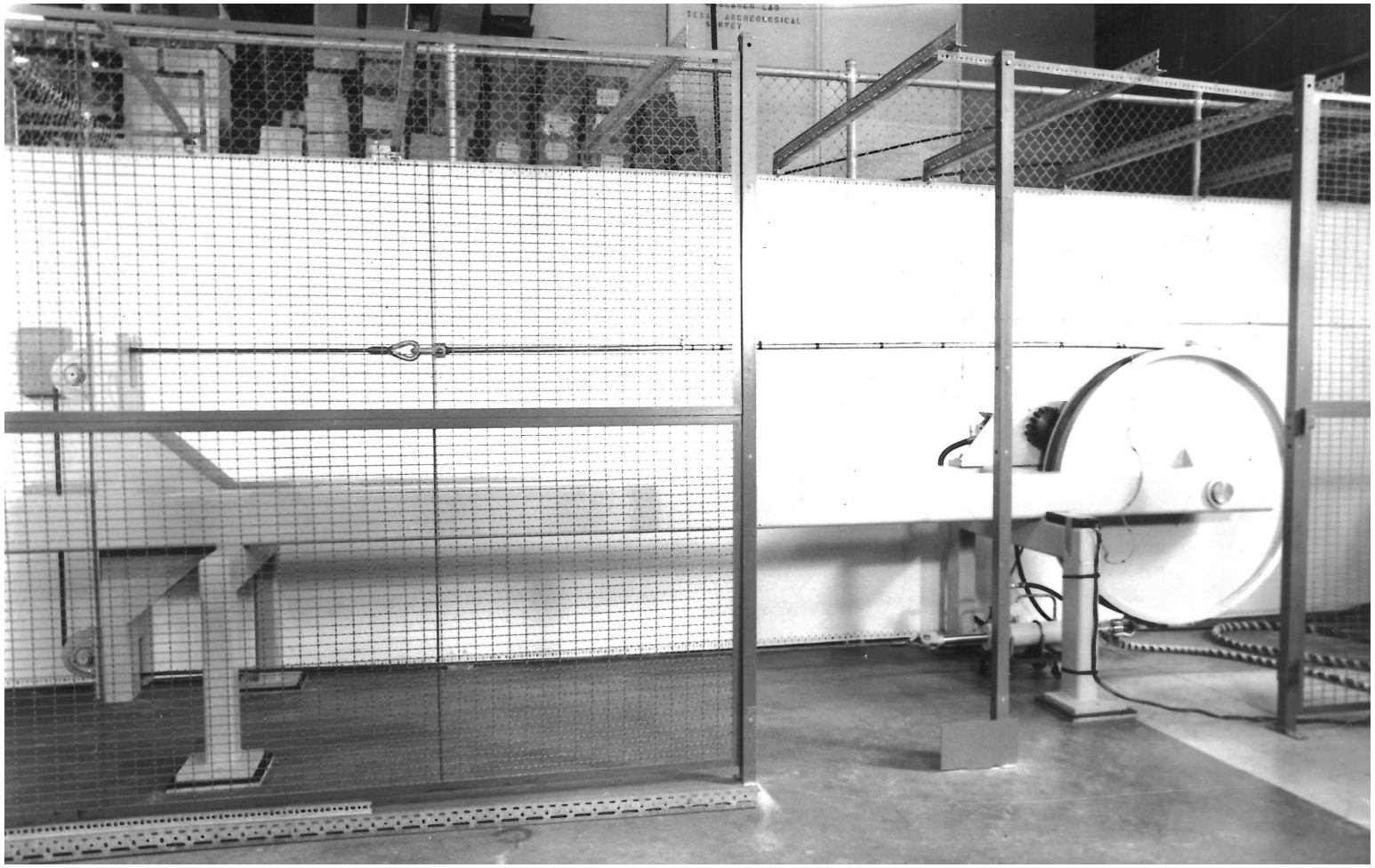

Figure 3.1 Photograph of the model reeling test facility use in the experiments (Kyriakides and Mok [1992]).

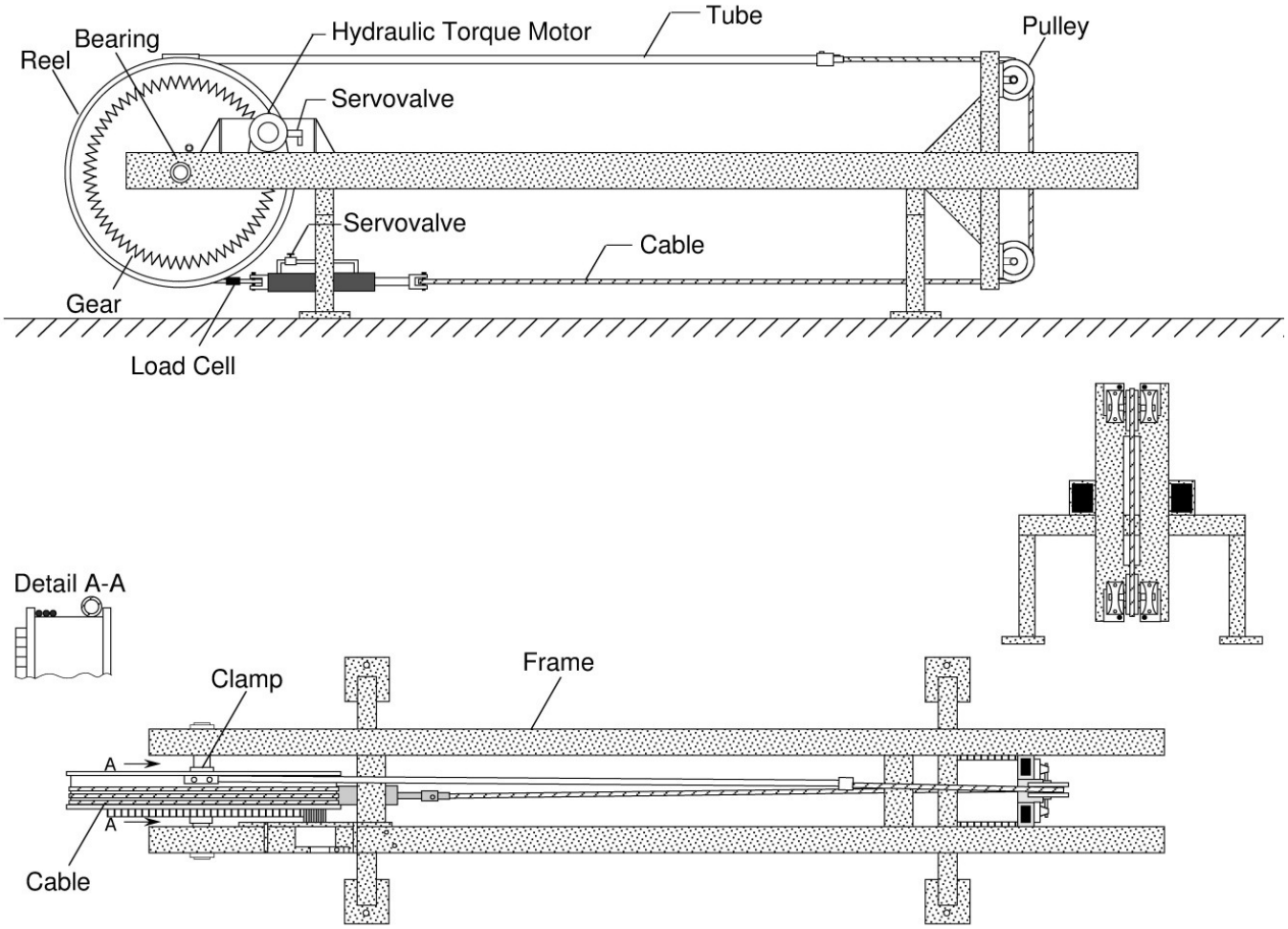

Figure 3.2 Scaled drawings of the model reeling test facility with major components identified (Kyriakides and Mok [1992]).

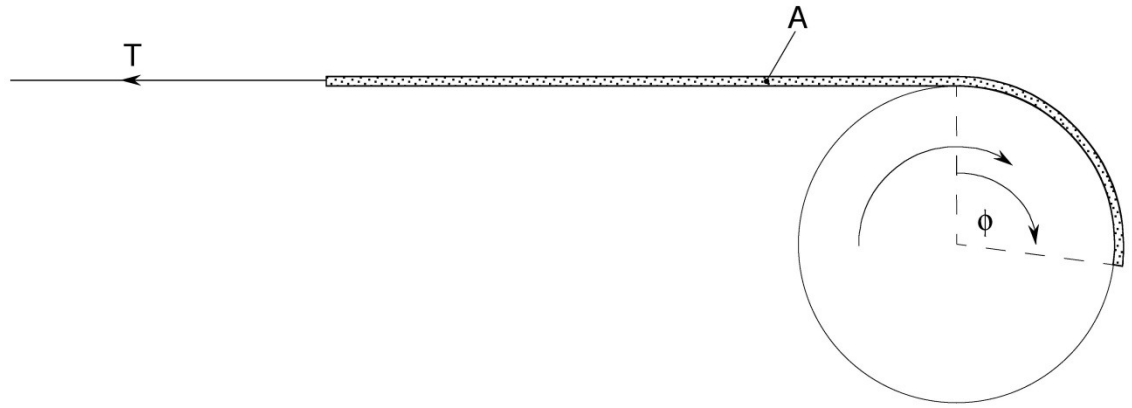

(a)

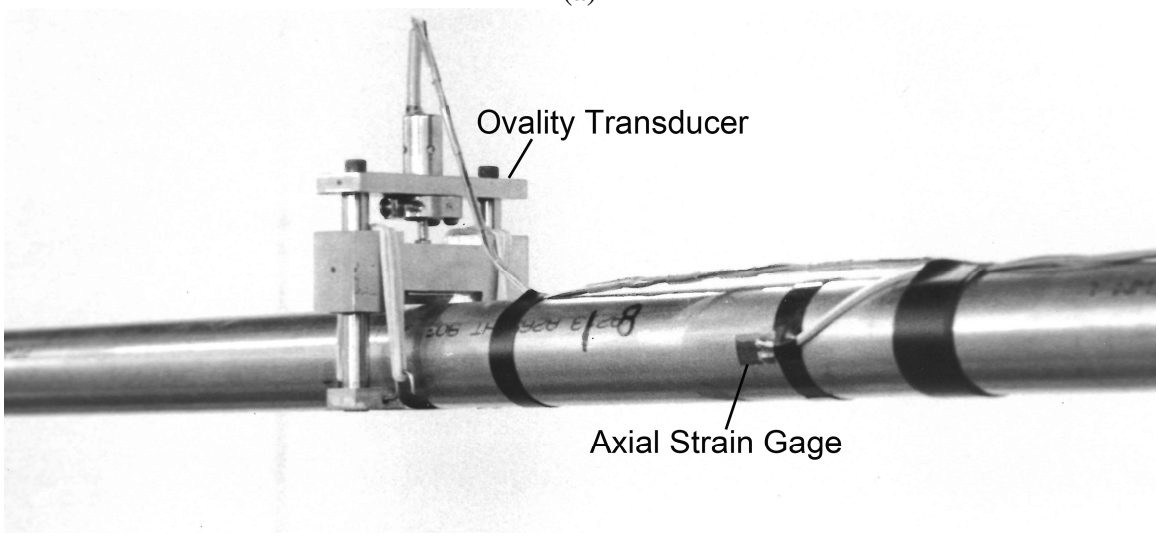

(b)

Figure 3.3 (a) Schematic showing a tube being wound onto the model reel under tension and (b) photograph of the transducer and one of the strain gages for monitoring change in diameter and axial strain at location A on the specimen during reeling (Kyriakides and Mok [1992]).

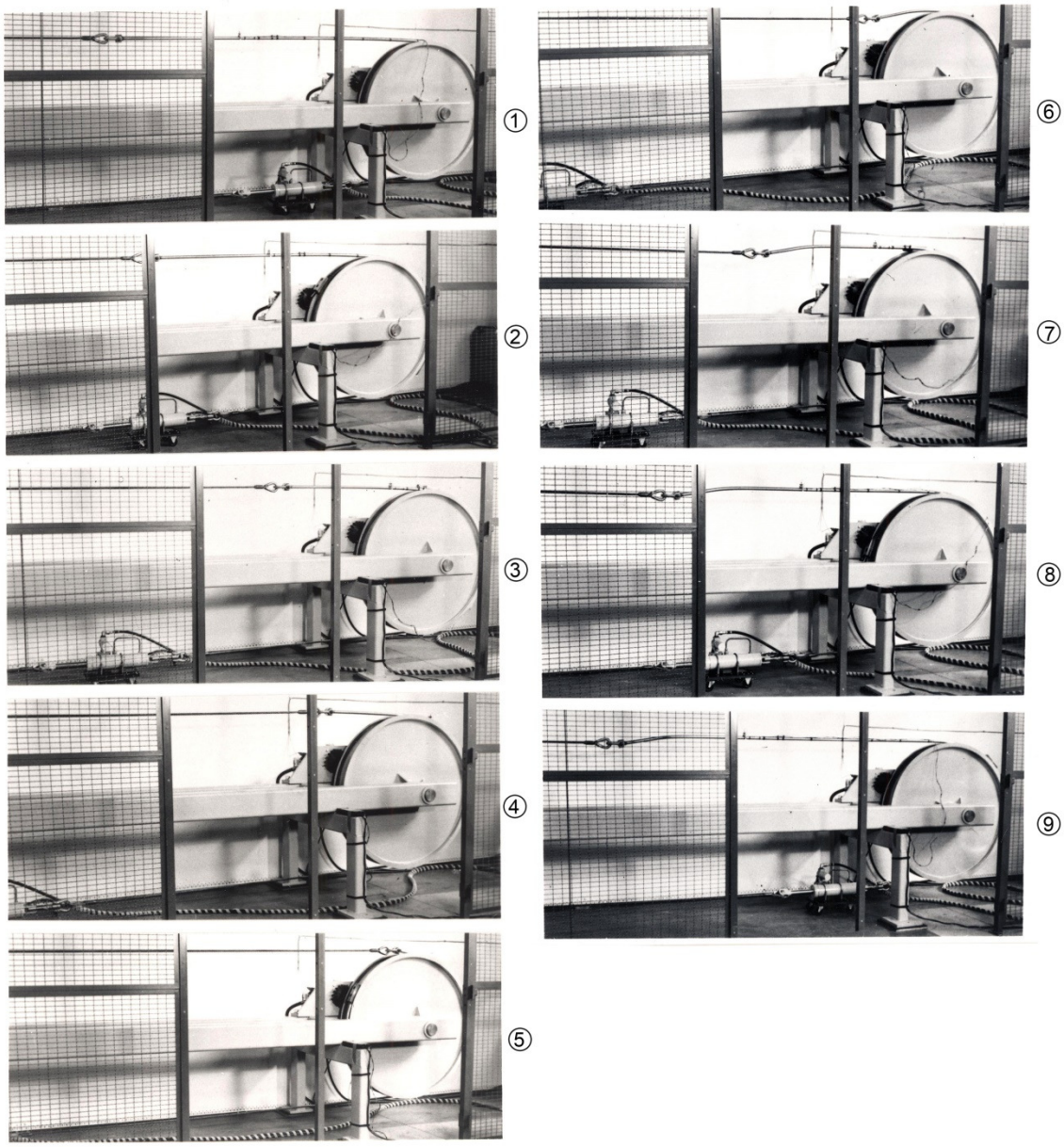

Figure 3.4 Sequence of tube configurations in the facility during reeling and unreeling (Kyriakides and Mok [1992]).

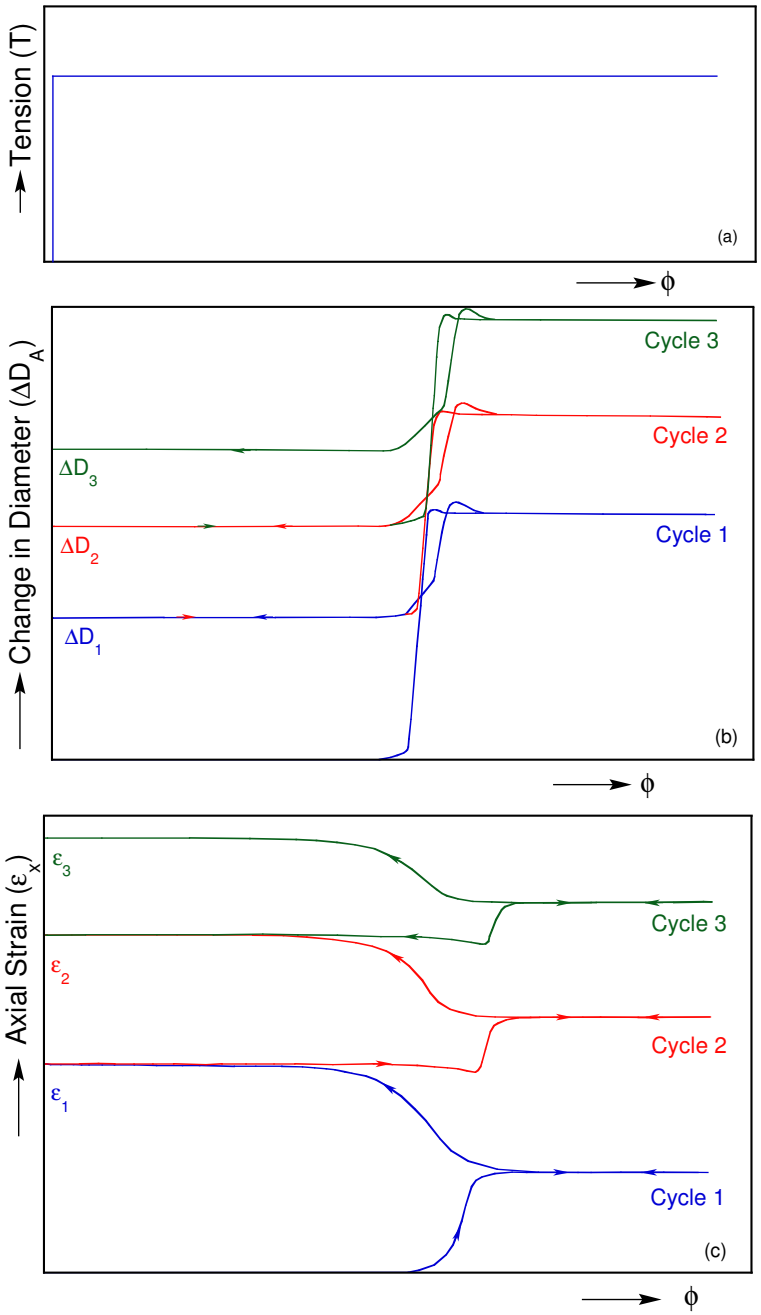

Figure 3.5 Experimental data showing (a) the applied tension, (b) the ovalization and (c) strain at section A vs. the reel rotation angle measured during three cycles of reeling/unreeling (Kyriakides [2017]).

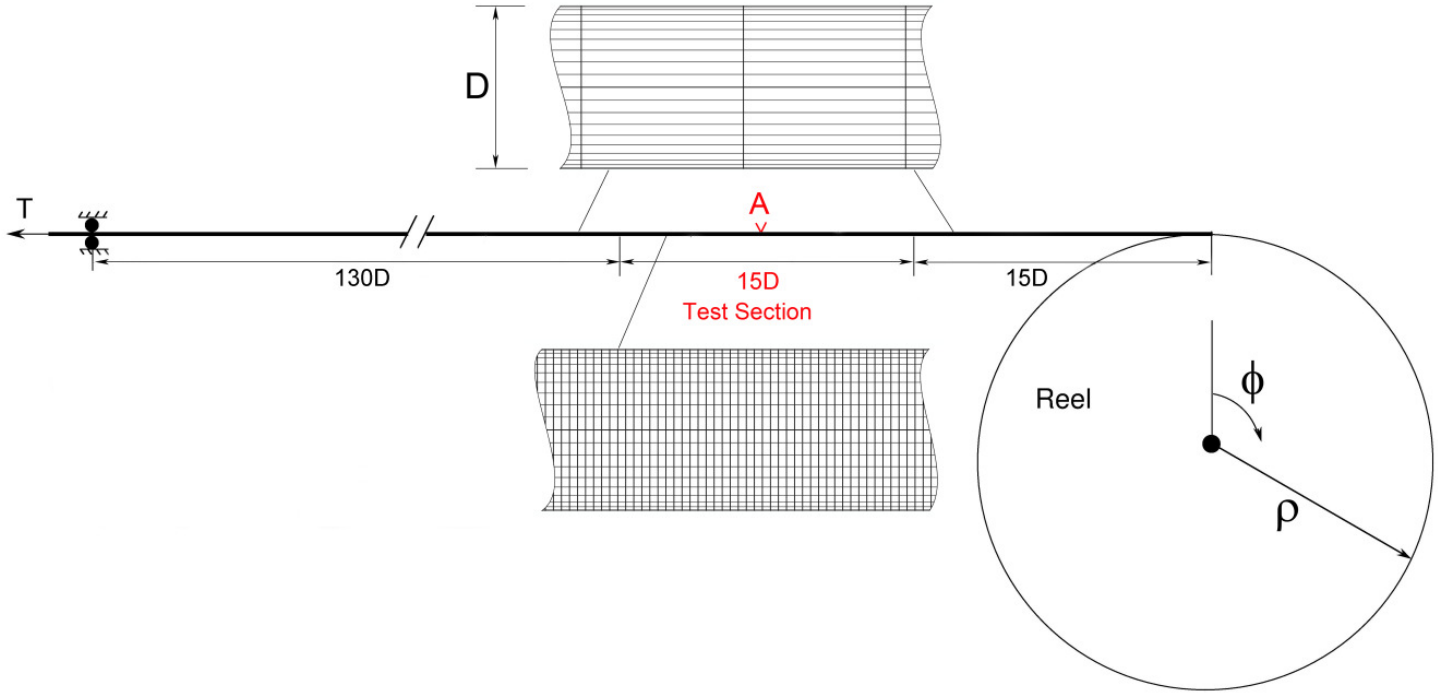

Figure 3.6 Geometry of the reel/pipeline 3-D finite element model.

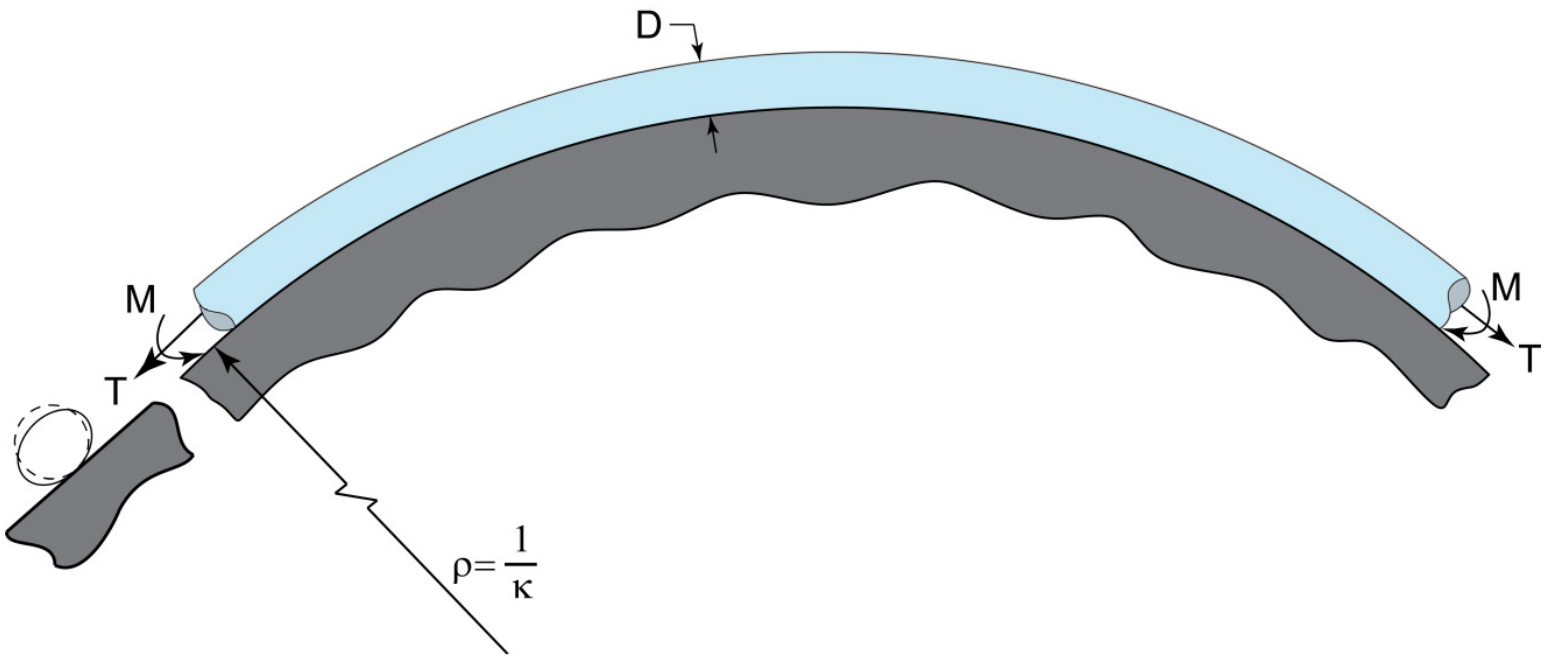

Figure 3.7 A 2-D model of reeling involving a section of pipe being bent over a rigid surface of uniform curvature κ, in the presence of tension T.

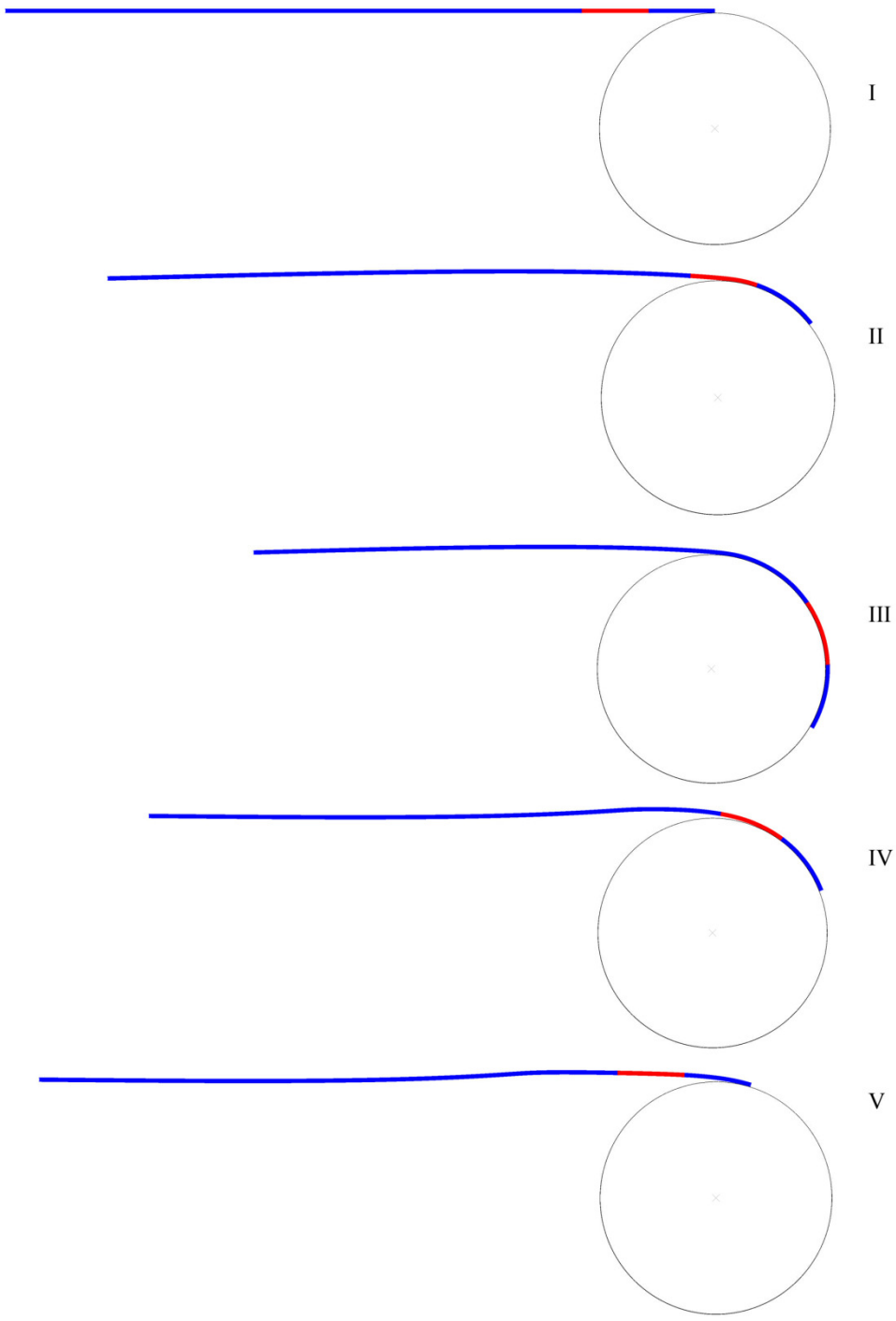

Figure 3.8 Calculated pipe reeling configurations for base case: I – III, winding and IV – V unwinding.

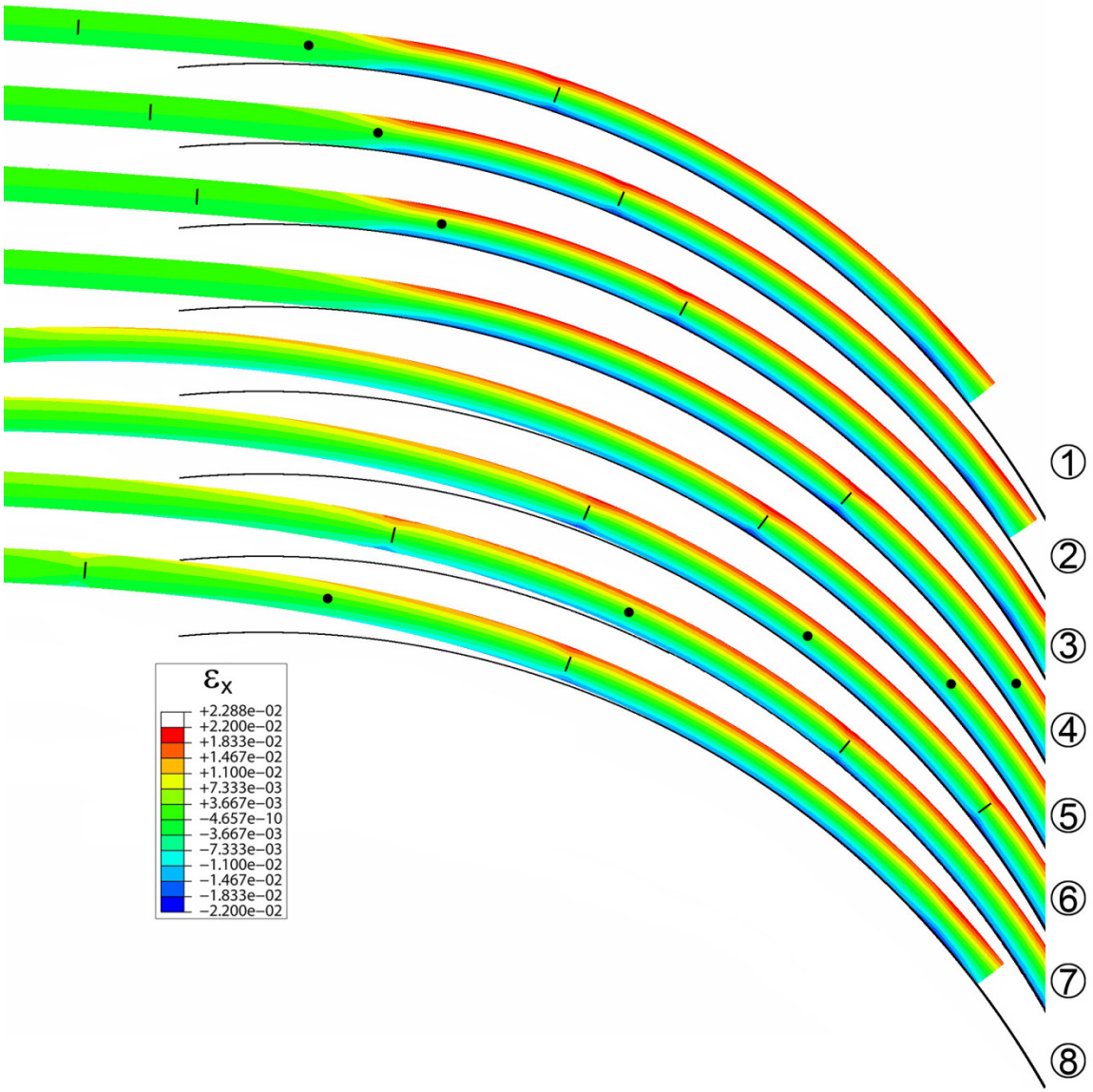

Figure 3.9 Pipe deformed configurations showing the test section coming into contact with the reel during winding, ①-④, and unwinding ⑤-⑧.

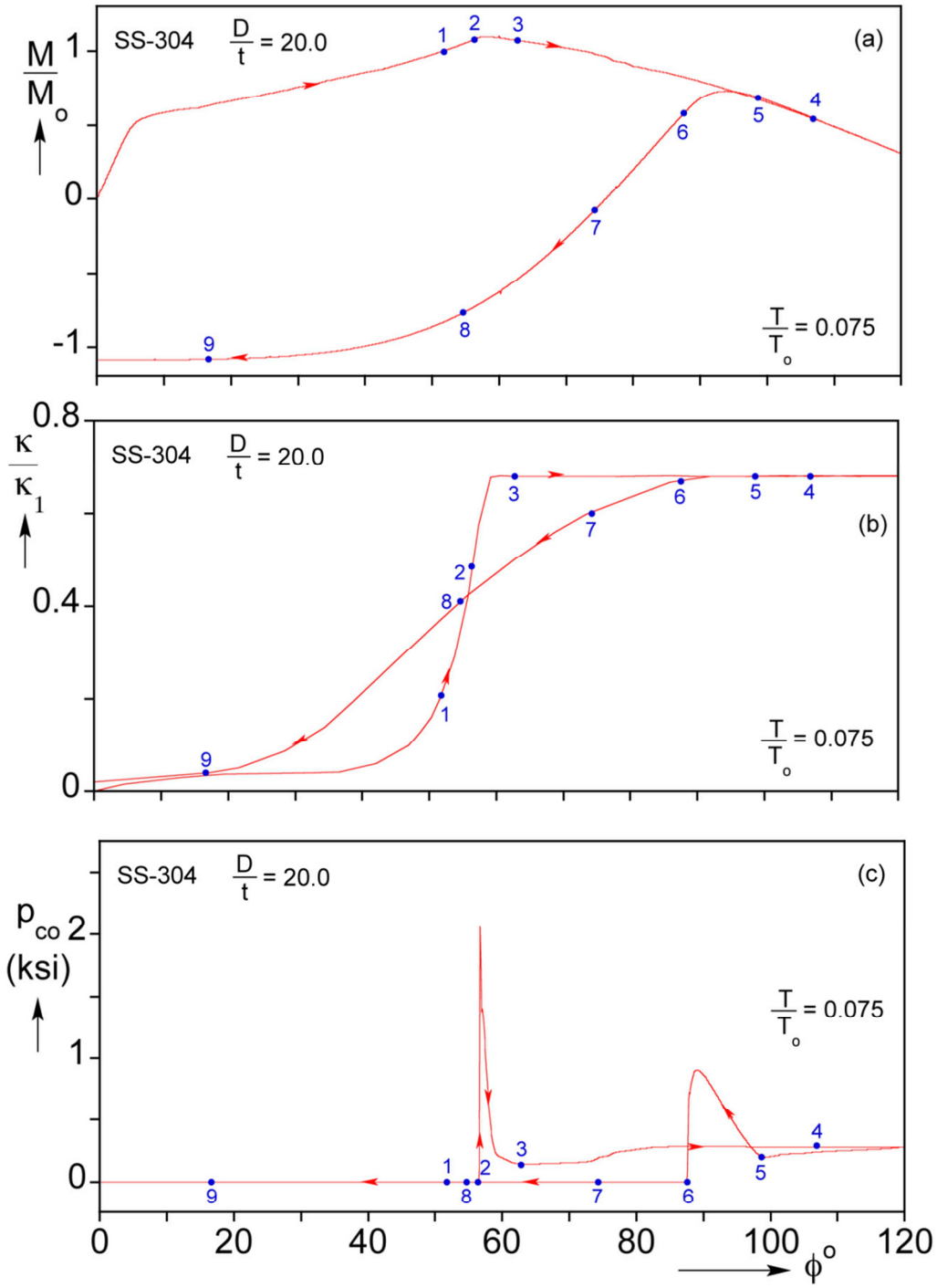

Figure 3.10 Evolution of section variables at section A with reel rotation, ϕ, during a complete wind-unwind cycle: (a) moment, (b) curvature, (c) contact pressure.

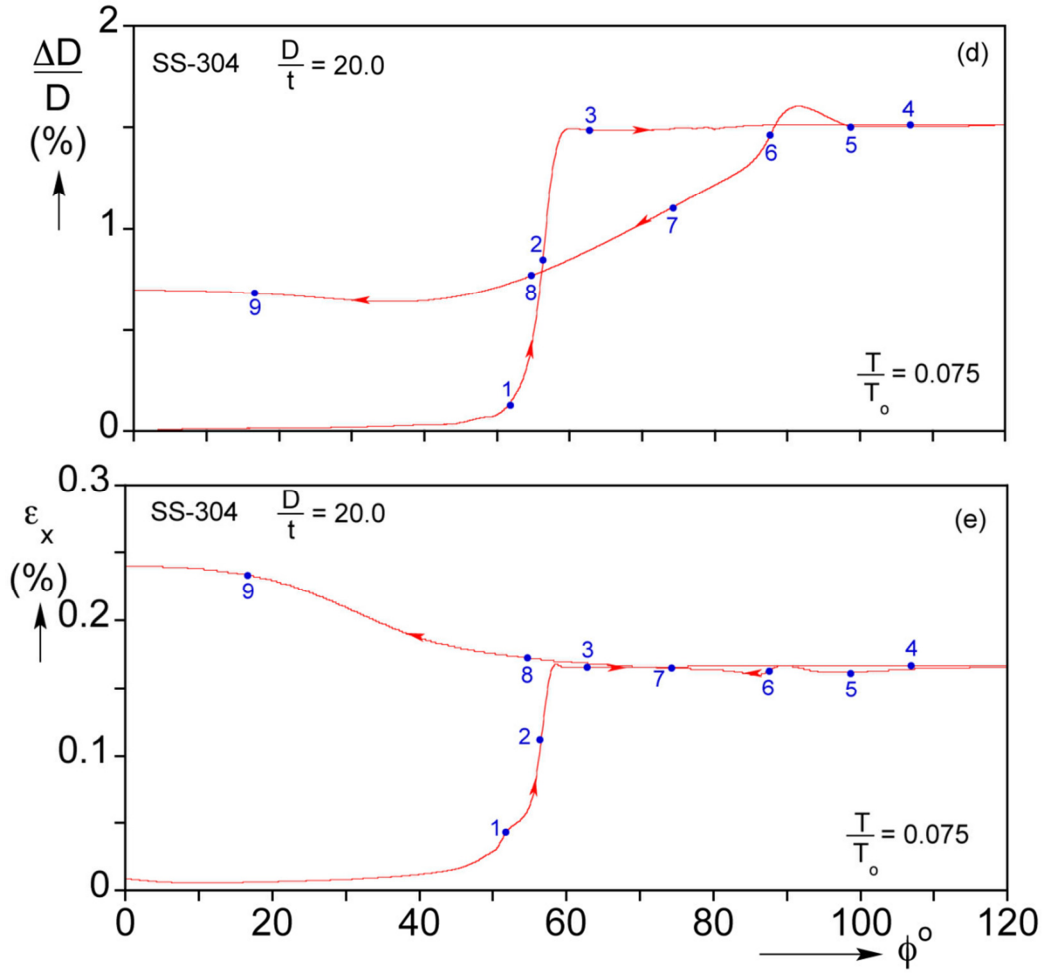

Figure 3.10 Cont. Evolution of section variables at section A with reel rotation, ϕ, during a complete wind-unwind cycle: (d) ovalization, and (e) mean axial strain.

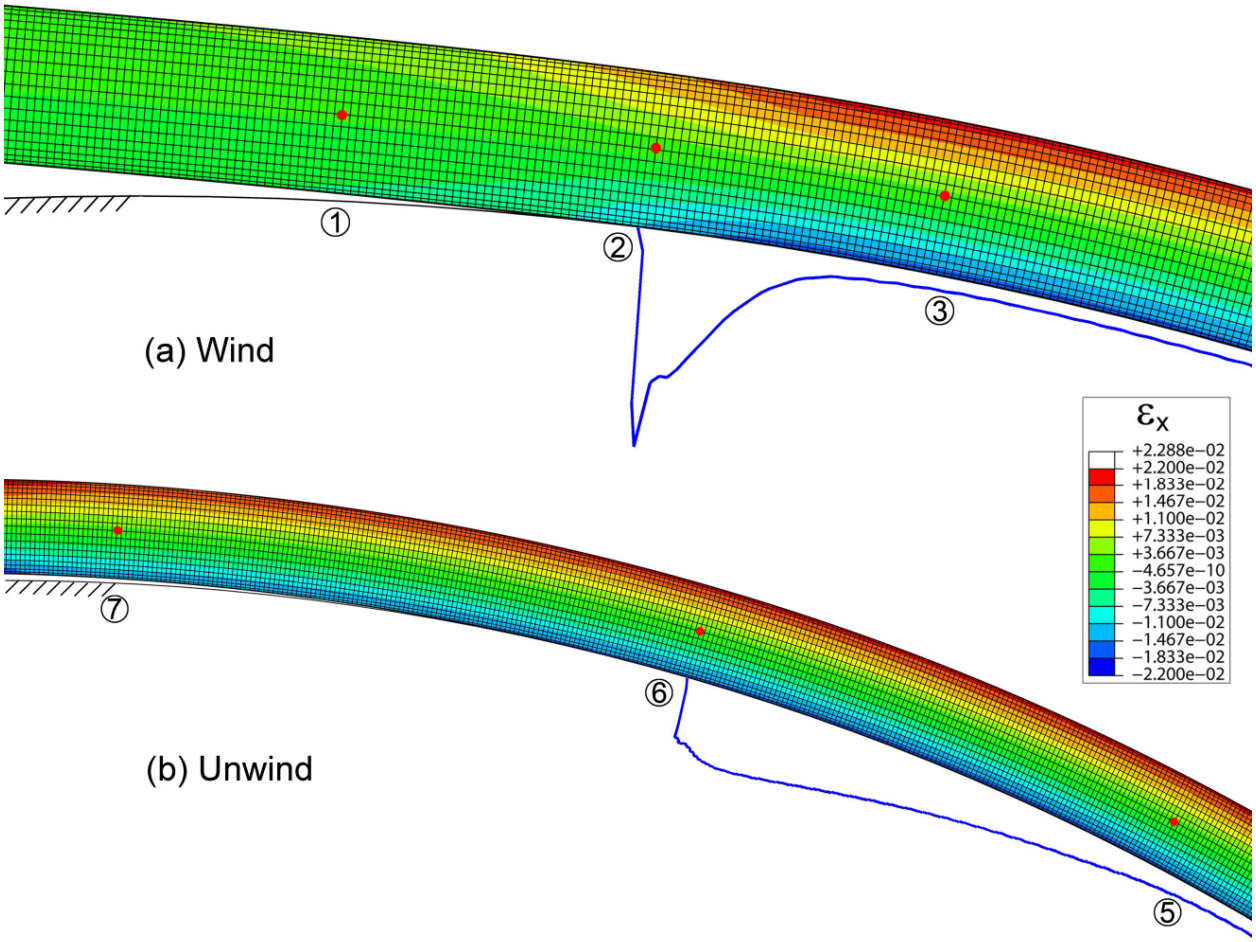

Figure 3.11 Pipe deformed configurations with contact pressure that correspond to the tube coming (a) into contact during winding and (b) off contact during unwinding.

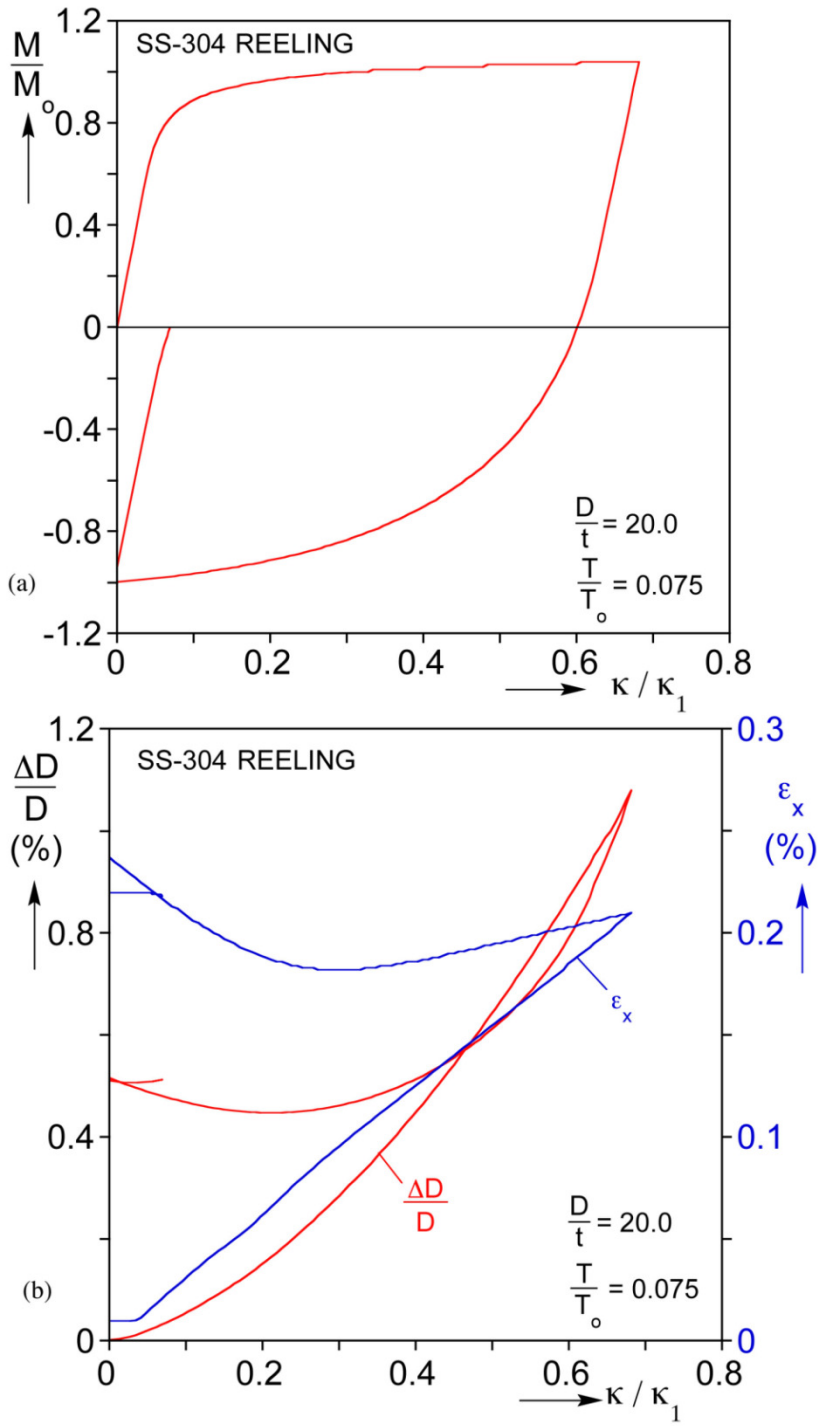

Figure 3.12 2-D model results for a single wind/unwind cycle: (a) moment vs. curvature and (b) ovalization and axial strain vs. curvature.

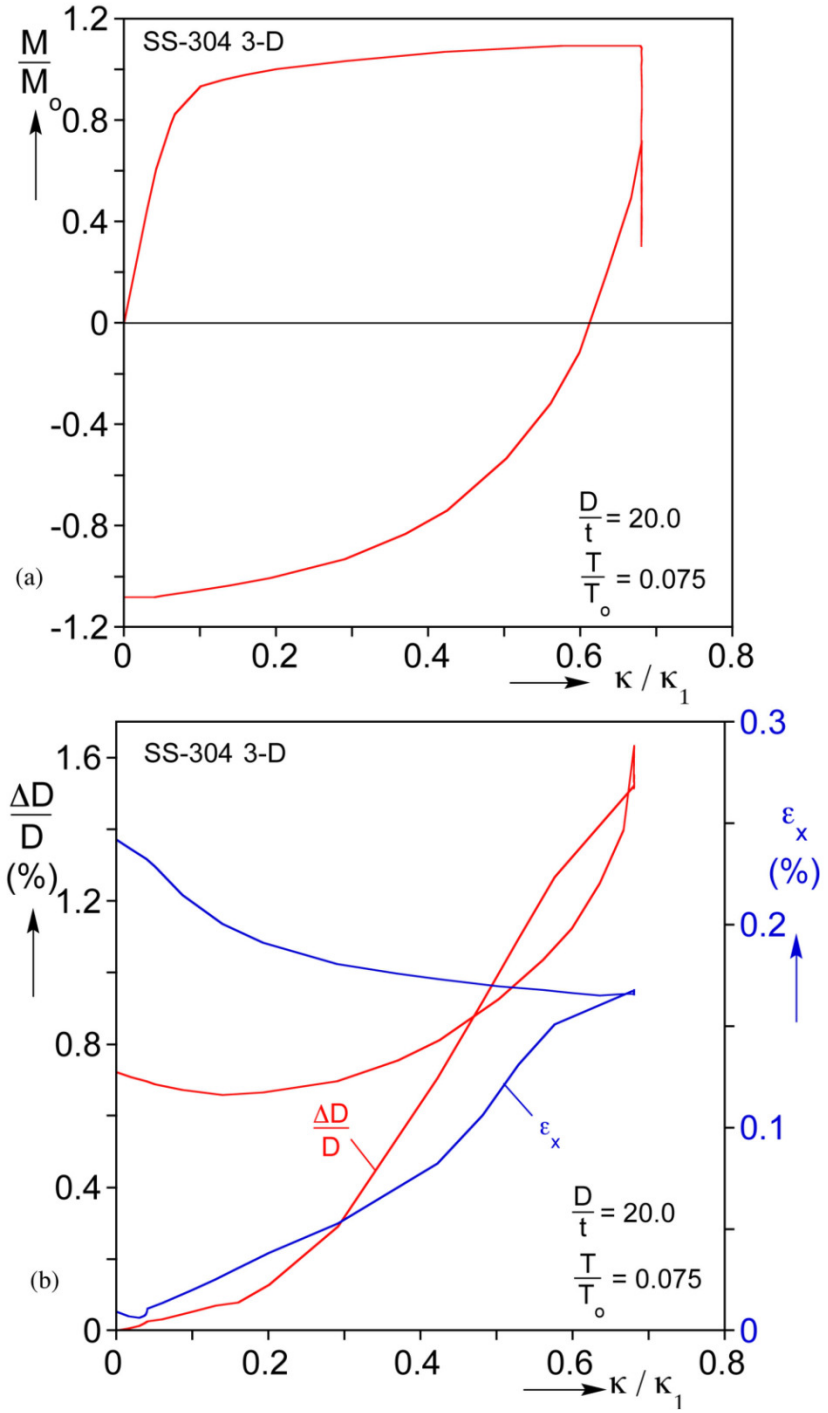

Figure 3.13 3-D model results at section A for a single wind/unwind cycle: (a) moment vs. curvature and (b) ovalization and axial strain vs. curvature.

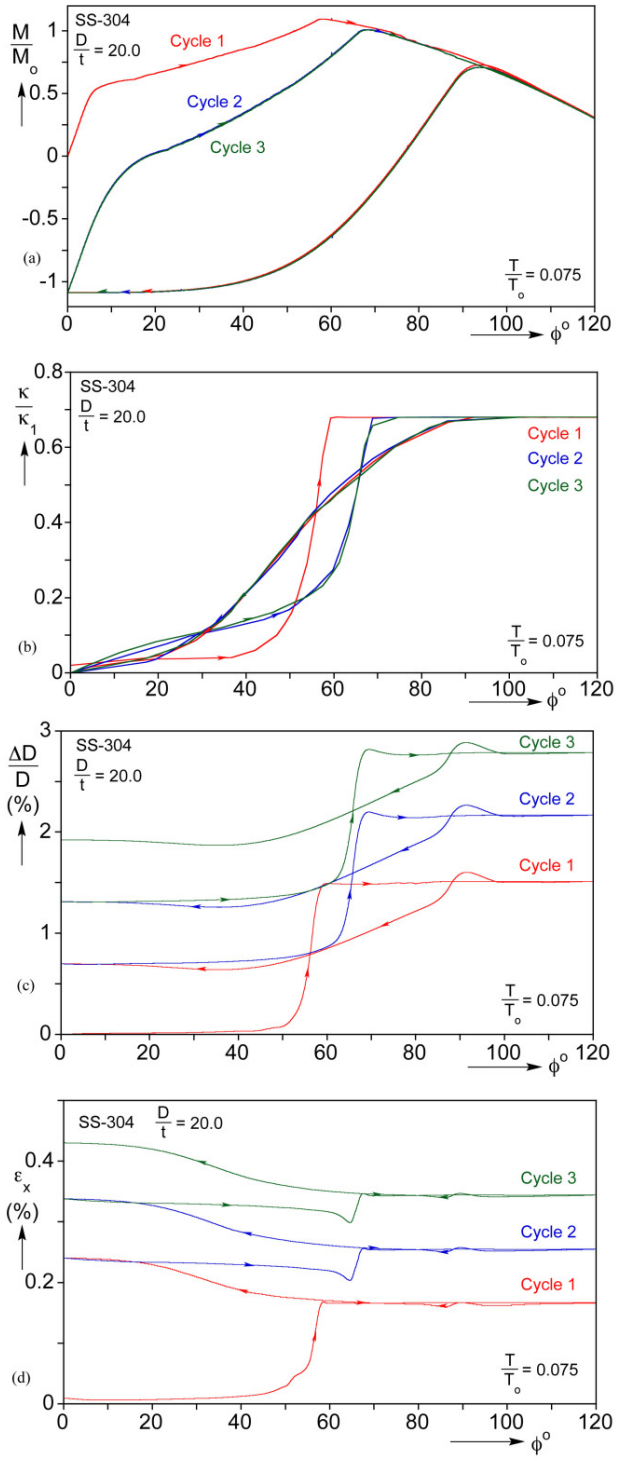

Figure 3.14 Evolution of variables at section A with reel rotation for three wind/unwind cycles: (a) moment, (b) curvature, (c) ovalization, and (d) mean axial strain.

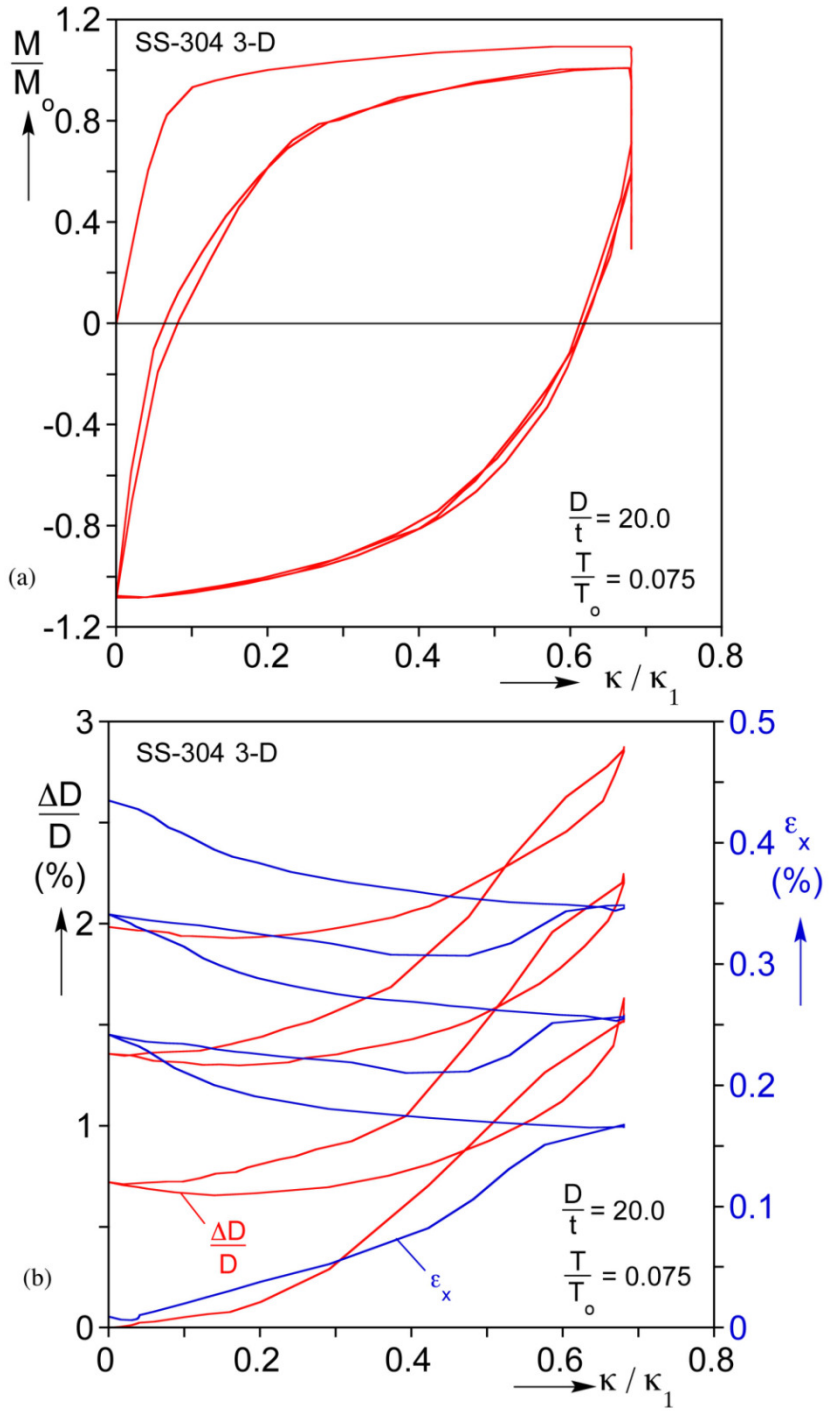

Figure 3.15 3-D model results at section A for three wind/unwind cycle: (a) moment vs. curvature and (b) ovalization and axial strain vs. curvature.

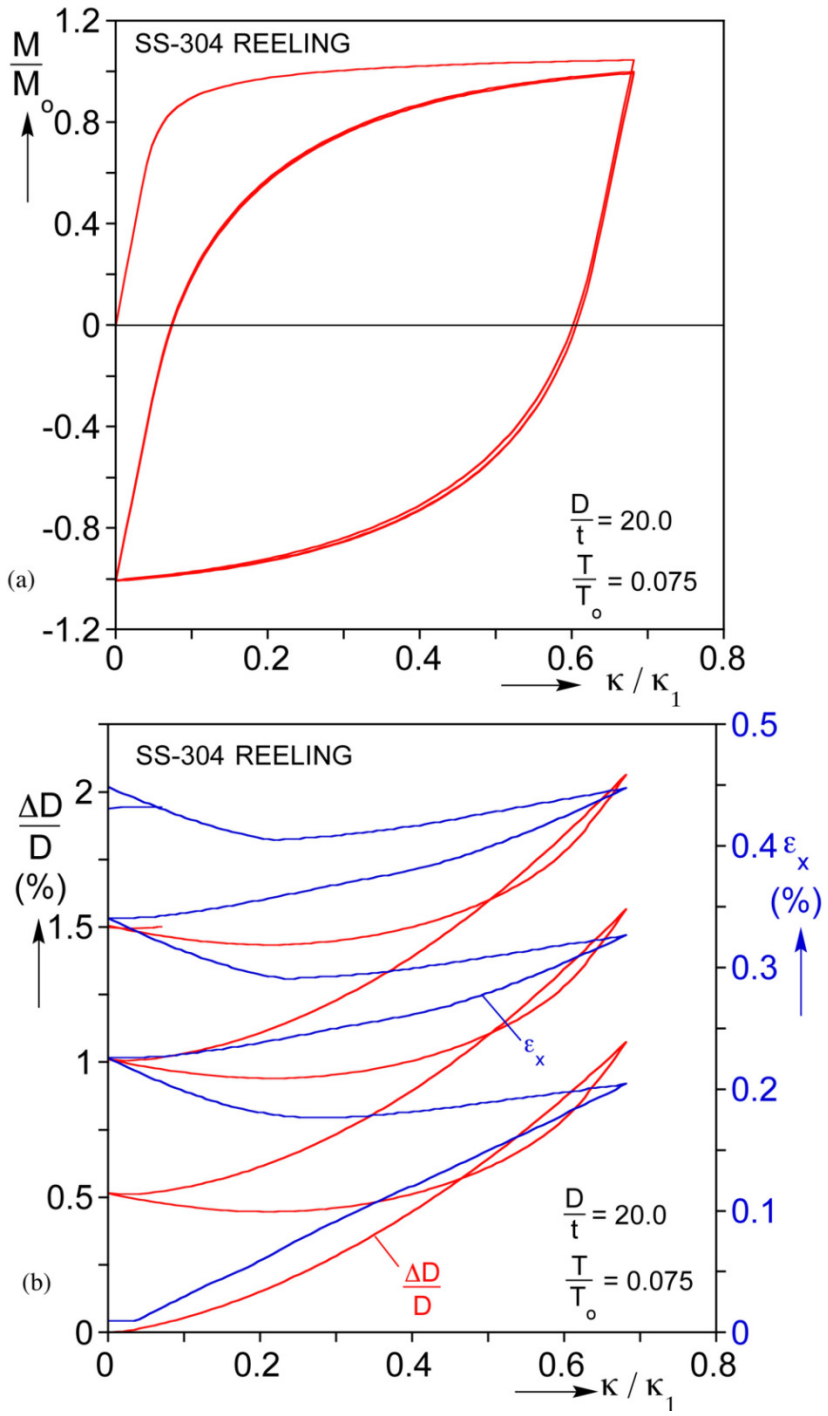

Figure 3.16 2-D model results for three wind/unwind cycles: (a) moment vs. curvature and (b) ovalization and axial strain vs. curvature.

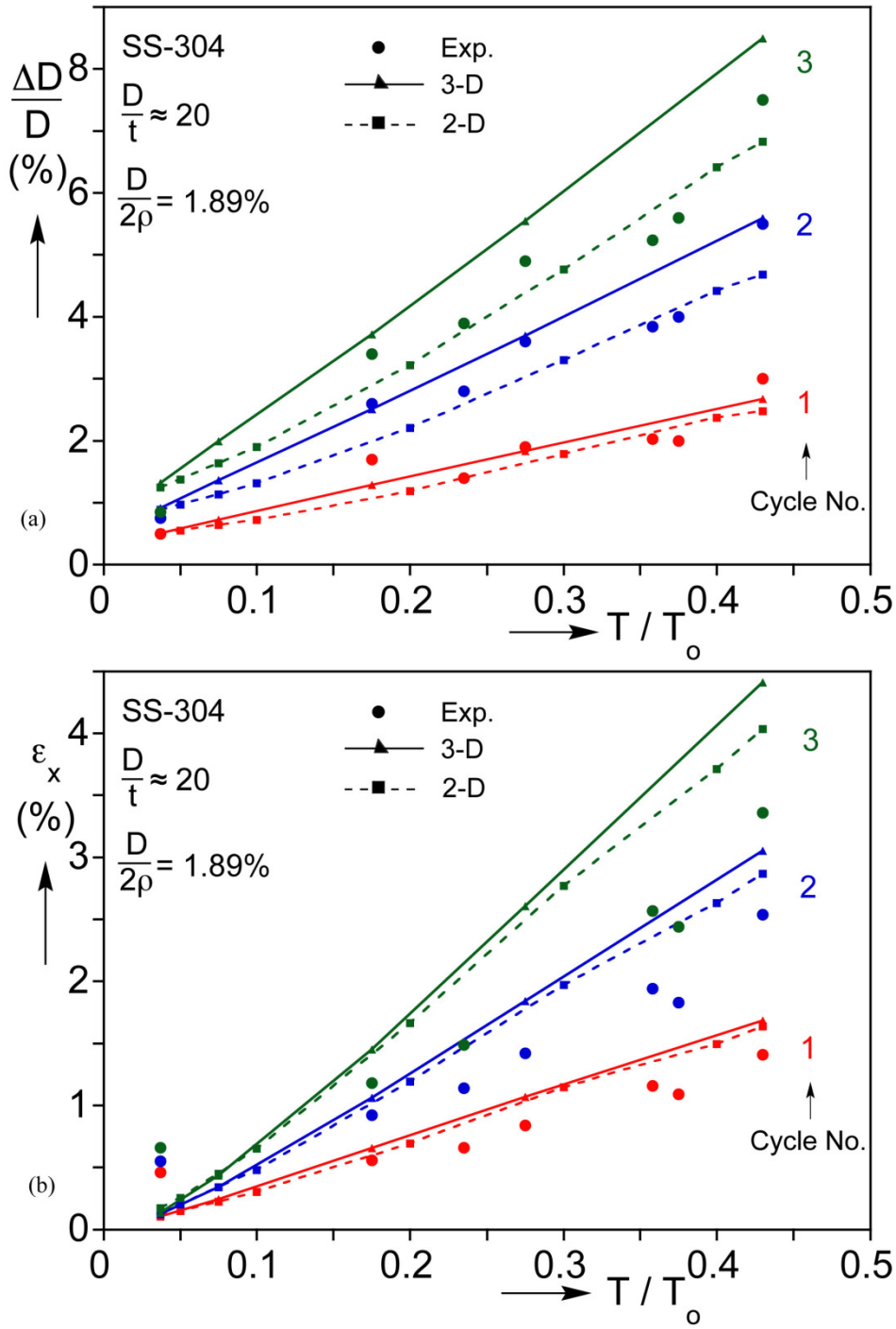

Figure 3.17 Measured and predicted residual (a) ovality and (b) axial strain vs. tension for three wind/unwind cycles for pipes with *D/t* = 20.

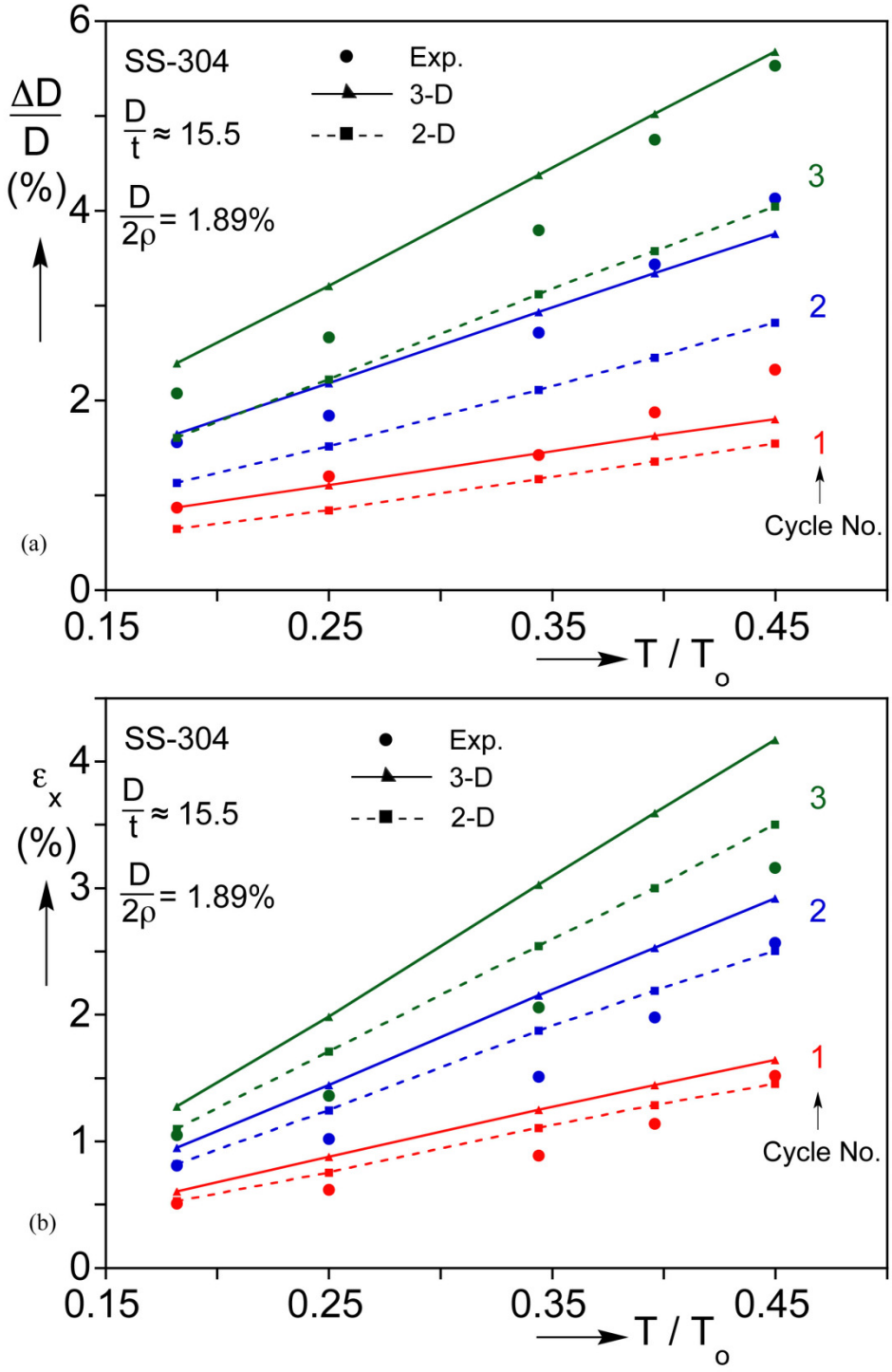

Figure 3.18 Measured and predicted residual (a) ovality and (b) axial strain vs. tension in three wind/unwind cycles for pipes with *D/t* = 15.5.

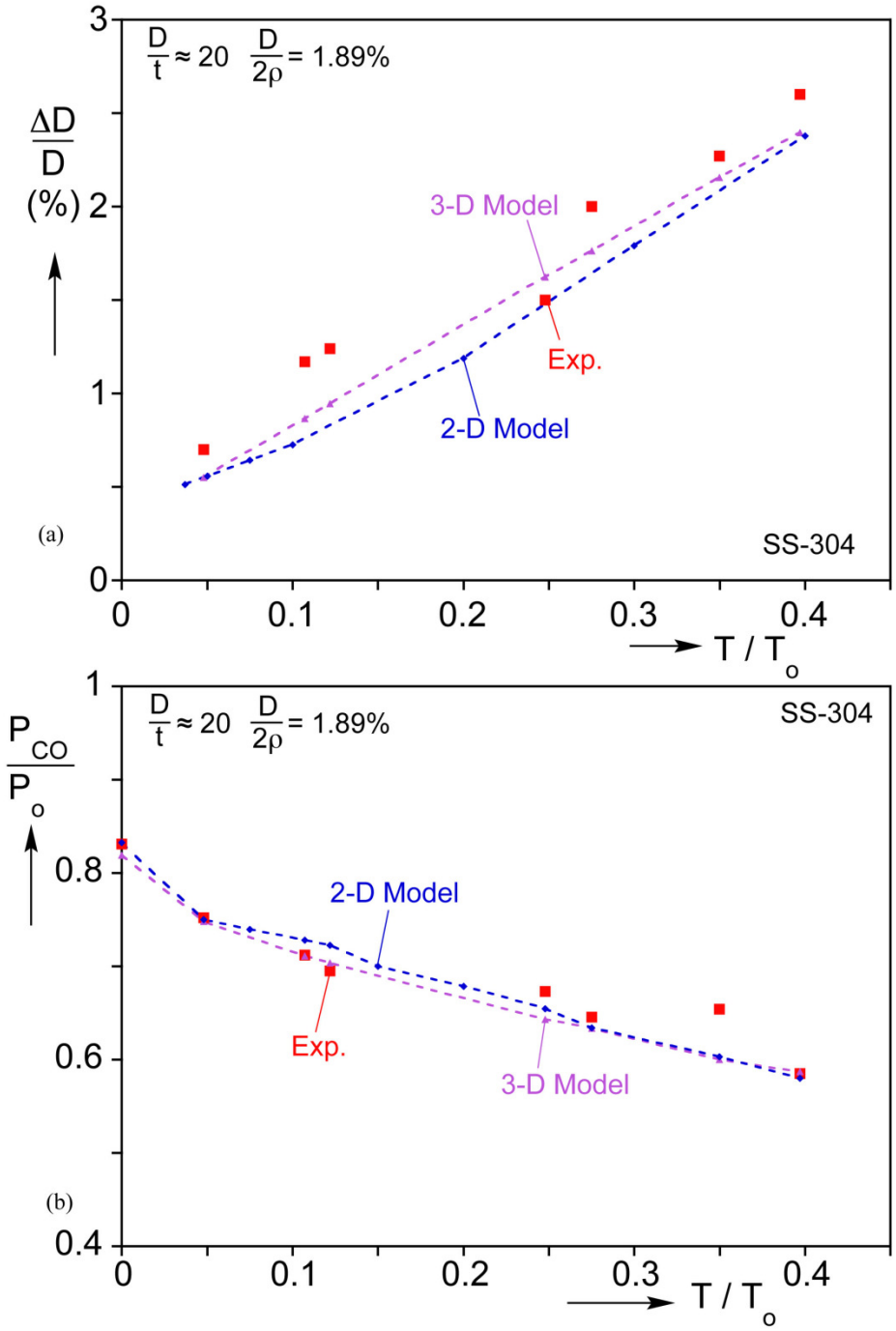

Figure 3.19 Measured and 2-D and 3-D model predicted section variables after a single wind/unwind cycle for tubes with *D/t* = 20: (a) residual ovality vs. tension and (b) collapse pressure vs. tension (data on ordinate are from as received tubes).

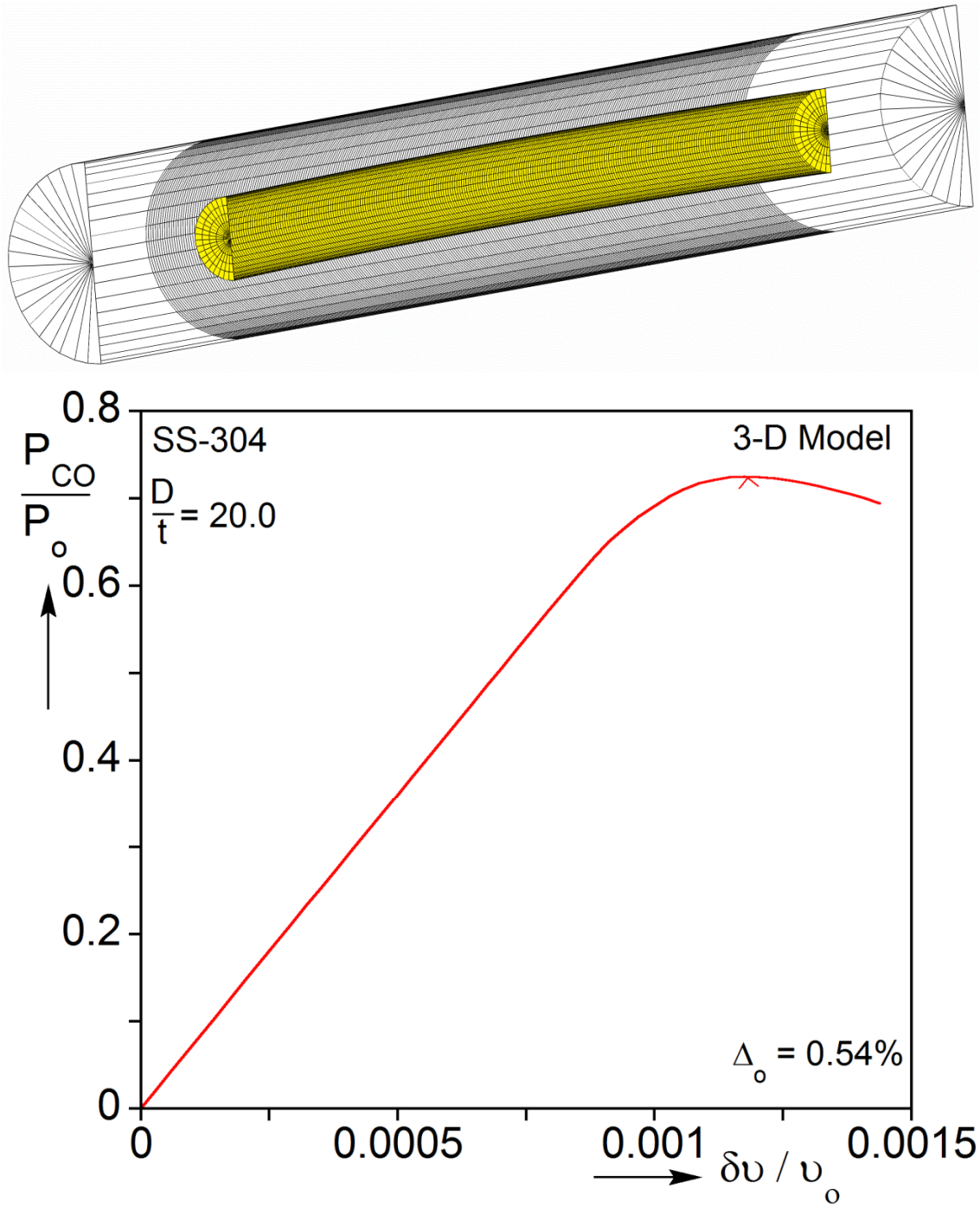

Figure 3.20 (a) Finite element model for calculation of the collapse pressure of the test of a reeled tube; included is the FE model of the tube and the surrounding fluid cavity. (b) Calculated pressure vs. change of volume response of base case with *D/t* = 20.

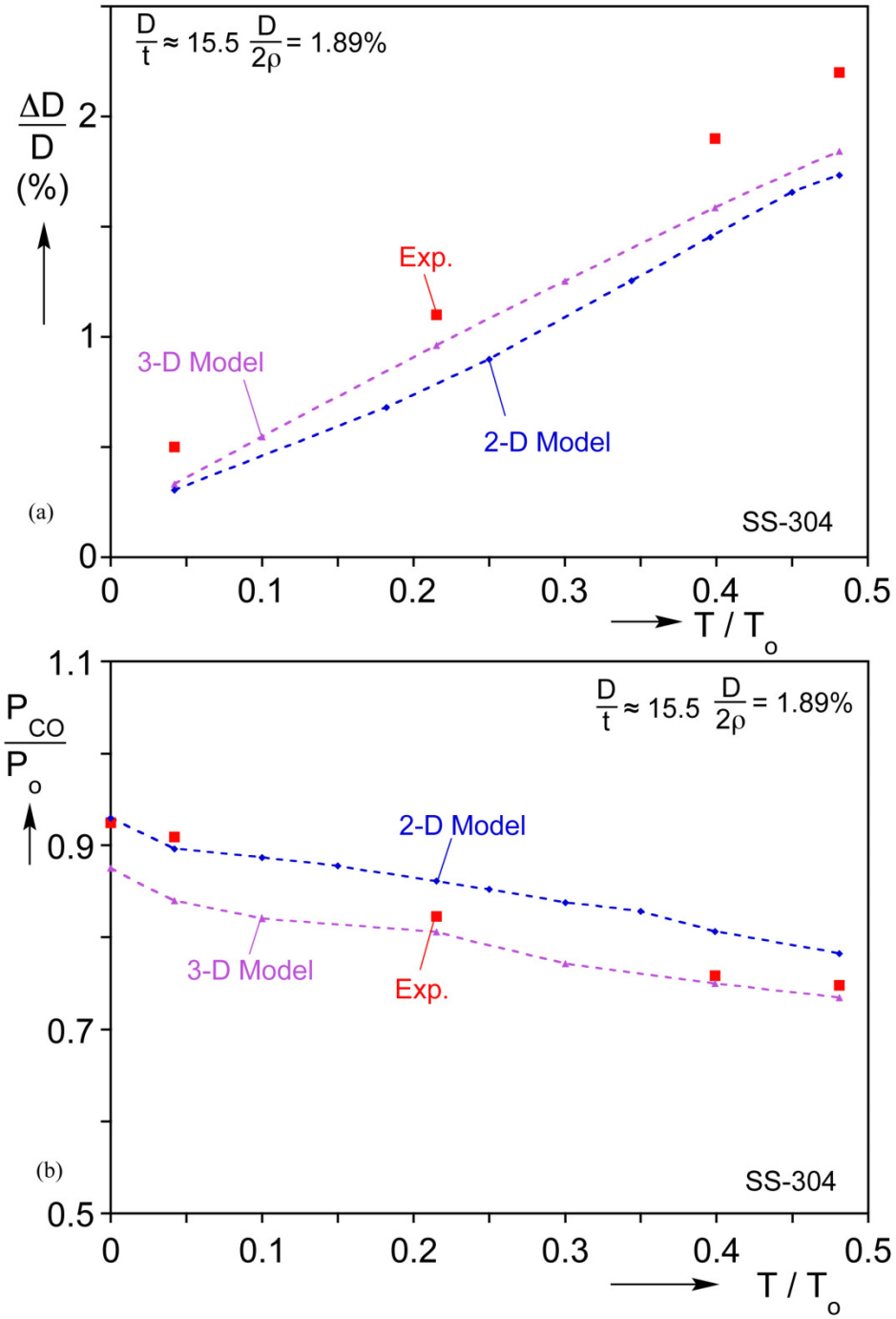

Figure 3.21 Measured and 2-D and 3-D model predicted section variables after a single wind/unwind cycle for tubes with *D/t* = 15.5: (a) residual ovality vs. tension and (b) collapse pressure vs. tension (data on ordinate are from as received tubes).

Chapter 4: EFFECT OF GEOMETRIC AND MATERIAL DISCONTINUITIES ON THE REELING OF PIPELINES[3,4]

In the reeling installation process, during winding the pipeline experiences bending strains of 1.5-3.0% (see Eq. (3.1)). The pipe is straightened on unspooling and bent once more as it conforms to the radius of the ramp before it is straightened again (see Fig. 1.1). The operator must ensure that the repeated bending and straightening are sustained free of local buckling or rupture in the line. Such failures are for example precipitated by pipeline discontinuities in wall thickness and yield stress as they act as stress risers, lead to localized deformations severe enough to result in local buckling. Variations in material yield stress between different strings of pipe and some variation along the length of a given string are unavoidable (see Bauer et al., 2002; Tsuru et al., 2012). Furthermore, thickness discontinuities due to designed changes in pipe wall thickness are common. In addition, in some projects thickness discontinuities result from the introduction of a thicker wall section to act as a buckle arrestor (Sriskandarajah et al., 2011). When such pipe discontinuities are reeled, they cause localized bending, ovalization and straining that can result in local buckling and, in extreme cases, rupture of the line (Brown et al., 2004; Denniel et al., 2009; Smith et al., 2011; Liu and Kyriakides, 2014).

This Chapter presents the results of a study that examines the local effects of discontinuities in pipe geometry and mechanical properties on the reeling installation process. The nonlinear kinematic hardening constitutive model of Chaboche [1986]

---

[3] Liu, Y. and Kyriakides, S. (2014). Effect of geometric and material discontinuities on the reeling of pipelines. *33rd Int'l Conf. Ocean, Offshore Arctic Eng.*, OMAE2014-24474, June 2014, San Francisco, CA, USA. (The author implemented the constitutive model, conducted the numerical simulations, and analyzed the results.)

[4] Liu, Y. and Kyriakides, S. (2017). Effect of geometric and material discontinuities on the reeling of pipelines. *Applied Ocean Research*, **65**, 238-250. (The author implemented the constitutive model, conducted the numerical simulations, and analyzed the results.)

described in Chapter 2 is used to capture the elasto-plastic behavior of the material imposed by the bending/reverse bending history. The effects of wall thickness and yield stress discontinuities of different amplitudes on the local behavior of the pipe are considered by varying the main problem parameters such as the back tension, the reel radius, and the pipe D/t.

4.1 FINITE ELEMENT MODEL

To simulate the reeling/unreeling process, a 3-D model of the complete wind/unwind history is developed within the nonlinear code ABAQUS. The reel is represented as a circular rigid surface with a radius ρ. A 160D long section of pipeline is connected to the reel as shown in Fig. 4.1. The other end of the pipeline is placed between rollers that prevent vertical but allow horizontal motion of the line. A constant tension force (T) is applied on the LHS and the line is wound by applying incrementally a rotation, ϕ, to the reel. The pipe is unwound by reversing the direction of rotation until ϕ is back to zero while the level of the back tension is maintained.

The pipe consists of a 20D long starter section, a 20D long "test section", and a 120D trailing section. The test section has a discontinuity at mid-length marked with the symbol “∨”in the figure. The pipe is assumed to deform symmetrically about the plane of bending so only half of the cross section is modeled. The whole structure is modeled with S4 shell elements. Of main interest are the stresses and deformations induced by the wind/unwind process by the discontinuity to its neighborhood. To capture this with accuracy, a finer mesh is adopted for the test section with 16 elements around the half circumference and 20 elements per diameter along the length. The other two sections have the same circumferential mesh distribution but only one element per diameter axially. The two mesh densities were arrived at from convergence studies.

The reel is modeled as an analytical rigid surface. Contact with the deformable pipe is modeled using a strict "master-slave" algorithm of ABAQUS, with the reel surface as the master and the pipe as the slave surface. The contact is frictionless but "finite sliding" is allowed between a contact pair. An exponential "softened" contact pressure-overclosure relationship is used with 500 psi (3.4 MPa) and 0.0001 in (0.00254 mm) being representative pressure and clearance values respectively.

4.2 NUMERICAL RESULTS

4.2.1 Reeling/Unreeling of a Pipeline with a Thickness Discontinuity

To set the stage for the parametric study that follows, some of the main aspects of the effect of a discontinuity in the pipeline on the reeling/unreeling process will be discussed through an example. It involves a X-60, 12.75 in (324 mm) diameter (D) pipe with a wall thickness t = 0.600 in (15.2 mm) that is wound onto a reel with a radius of 324 in (8.23 m) using a back tension of 0.02 times the yield tension of an X-60 grade pipe ($T = 0.02T_O$; see Table 4.1). Winding takes place by incrementing the angle ϕ, while the tension is kept constant. Figure 4.2 shows five images showing the line in its initial configuration (⓪), during winding (images ① and ②), and unwinding (images ③ and ④). The symbol "∨" depicts the position of a thickness discontinuity of $\Delta t = 0.1t$ (pipe to the left of "∨" has wall thickness $0.9t$; see schematic in Fig. 4.3a). In image ①, the site of the discontinuity is just coming into contact with the reel. It is worth noting that the point of contact is preceded by a gradually bending transition length of pipe. In image ② a length of $80D$ has been wound onto the reel. Image ③ shows the pipe during unwinding with the section with the discontinuity just lifting off the reel. Again, a transition length of bent pipe is observed ahead of liftoff. In image ④ the unwinding of the pipeline has

been completed, with most of it being nearly straight but a bent section separates the part that was reeled with that on the left that was not.

Table 4.1 Base case main geometric and material parameters

D in (mm)	t in (mm)	$\frac{D}{t}$	ρ in (m)	E Msi (GPa)	σ_o ksi (MPa)	T_o kips (tonne)
12.75 (323.9)	0.600 (15.2)	21.25	324 (8.23)	30.0 (207)	60.0 (414)	1374 (623)

Reeling and unreeling plasticize and ovalize the pipe. The discontinuity causes in addition local distortion to the pipe shape and cross section. The axial shape distortion will be represented by local changes in curvature, and cross sectional changes will be represented by the changes in diameter. To this end, in the neighborhood of the discontinuity we will be monitoring the shell mid-surface curvature, κ / κ_1, the change in diameter in the plane of bending, $\Delta D / D$, and the equivalent plastic strain in the shell generator at the top, ε_e^p, where the normalizing variables are: $\kappa_1 = t / D_o^2$, $D_o = D - t$. Each will be plotted over a $10D$ long section that spans the discontinuity first during winding (configuration ②) and second after unwinding (configuration ④); the discontinuity is located at $s = 0$ with the reduced thickness pipe extending for $s \geq 0$). Accordingly, Fig. 4.4a shows the effects on the local curvature, Fig. 4.4b plots the induced local change in diameter and Fig. 4.4c the changes in the equivalent plastic strain. The local curvature is calculated using a three point centered average of the deformed coordinates of the element nodes at the mid-surface of the shell.

Figure 4.4a demonstrates that, for the present problem parameters, during winding a $2D$ long section of pipe at the discontinuity suffers a rather large local increase in curvature, whereas the pipe on either side of it is at a normalized curvature of less than 1,

the value that corresponds to the reel curvature. During unwinding, the section of interest becomes nearly straight as observed in image ④ and the values of κ/κ_1 at the ends of the section; however, the local "kink" introduced during winding remains but with a reduced amplitude.

Figure 4.4b portrays the local distortion of the cross section caused by the discontinuity. It takes the form of excessive ovalization (note the lower $\Delta D/D$ on either end with the value on the thinner pipe on the right being somewhat higher). It is accompanied by a local bulge that is clearly seen in the deformed configuration of this neighborhood of the pipe shown in Fig. 4.3b. The same image also shows a section about $3D$ long to have lifted off the reel, apparently a result of excessive local curvature that developed. Unreeling reduces the ovalization on both sides of the discontinuity but, as expected, a residual amount remains (Corona and Kyriakides [1991], Kyriakides [2016], Liu et al. [2017]). The local distortion at the discontinuity is also reduced and is not visible in the corresponding image in Fig. 4.3b.

The plots of the equivalent strain in the top generator in Fig. 4.4c demonstrate its plastification as it conformed to the reel curvature, but the discontinuity causes a significant additional local strain concentration. It is interesting to note that straightening the pipe increases the plastic strain in this generator everywhere and adds significantly to the local strain concentration (reflected also in the unreeled configuration in Fig. 4.3b). Clearly such strain concentrations can be dangerous and must be controlled.

In the sections that follow we will discuss how the various parameters of the problem affect such local distortions introduced by a discontinuity in the pipeline, in some cases causing local buckling.

4.2.2 Effect of Back Tension

The value of back tension used during reeling affects the curvature of the transition section adjacent to the point of contact with the reel. It will be shown that higher tension tends to reduce the local disturbances caused by discontinuities such as the ones described in Section 4.2.1. However, tension tends to also increase the ovalization of the whole pipeline during reeling and, as a result, cannot be applied arbitrarily (Kyriakides and Mok [1992], Kyriakides [2017], Liu et al. [2017]). Here we examine how the back tension affects the neighborhood of the discontinuity. We perform reeling/unreeling simulations at tension levels of $0.01T_o$, $0.02T_o$, and $0.05T_o$ using the same pipe geometric and material parameters as well as the reel radius as those in Table 4.1. A thickness discontinuity of $\Delta t = 0.1t$ is adopted. Figure 4.5 compares: (a) the variation in curvature, (b) the change in $\Delta D/D$, and (c) and the induced strain in the neighborhood of the discontinuity in the wound state (i.e., corresponding to image ② in Fig. 4.2). Figure 4.5a demonstrates that the local curvature disturbance reported in Fig. 4.4a is reduced when the tension is increased to $0.05T_o$ but is aggravated significantly for $T = 0.01T_o$ causing the pipe to develop a very severe local shell-type buckle as shown in Fig. 4.6a. The movie in Appendix A of Liu and Kyriakides [2017] demonstrates that the buckling occurs just as the discontinuity is approaching the reel. The back tension, which tends to reduce the local curvature keeping the pipe in contact with the reel, is too low in this case, which allows the curvature to increase resulting in the local buckle. The buckle can be seen in Fig. 4.6 that compares the local deformed configurations in the neighborhood of the discontinuity for the three tension values. Buckling results in a significant local drop in moment capacity causing the neighborhood of the buckle to lift off the reel. By contrast, while under tension of $T = 0.02T_o$ the section with the discontinuity lifts off the reel as shown in Fig. 4.6b, it survives the

wind/unwind cycle. The image of Fig. 4.6c, corresponding to the highest tension of $T = 0.05T_o$, shows the pipe to be in nearly perfect contact with the reel during winding.

Two more detailed views of the buckle appear also in Fig. 4.7. It is located in the thinner section of pipe next to the discontinuity. It has developed from localized wrinkling, consisting of a sharp inward kink accompanied by a protrusion (e.g., compare with images of local bending buckles in Ju and Kyriakides [1992] and Corona et al. [2006]). The local strains in the high curvature parts of the wrinkles are large enough to cause catastrophic rupture. Even if such a buckle survives during winding, it will almost definitely rupture if an attempt is made to straighten the damaged section (e.g., see Das et al. [2008]). (Note that a failure criterion and a finer mesh will be required for establishing if such buckles will result rupture.)

In Fig. 4.5b the highest tension is shown to decrease the local disturbance in $\Delta D/D$. But, at the same time, $\Delta D/D$ increases in the uniform sections on either side of the discontinuity. Of course, for $0.01T_o$ the local buckle results in a very severe increase in local ΔD. In Fig. 4.5c, the buckle that develops at the lowest tension causes also a very significant local increase in the plastic strain at the top generator while at the highest tension the disturbance caused by the discontinuity is reduced.

Figure 4.8 shows the corresponding plots following unreeling. Straightening the case with tension $0.01T_o$ that buckled is not attempted. Unwinding straightens the pipe and this reduces the local curvature disturbance for the other two tension levels, but the residual value remains rather large for $0.02T_o$ (Fig. 4.8a). The ovality disturbance is also reduced for both tension levels but, as expected, a residual value remains on both sides of the discontinuity (Fig. 4.8b). It is noteworthy that the residual ovality is larger for the higher tension. By contrast, Fig. 4.8c shows that straightening results in an increase in

the plastic strain for both tension levels. This increase is also reflected in the deformed image in Fig. 4.6c.

4.2.3 Effect of Thickness Discontinuity

The effect of the amplitude of the thickness discontinuity during reeling/unreeling is evaluated for the same pipe and reel parameters, at a tension level of $T = 0.025T_o$ for the following values: $\Delta t / t = \{0.025, 0.05, 0.10, 0.125\}$. Figure 4.9 shows plots of the local curvature, change in diameter and plastic strain in the top generator in the neighborhood of the discontinuity in the reeled condition. Figure 4.10 shows the same variables after the pipelines are unreeled. All values of Δt discontinuity cause local disturbances in curvature (Fig. 4.9a); the disturbance is very small for $0.025t$, somewhat larger for $0.05t$, and quite significant for $0.1t$. The image in Fig. 4.11a shows that a local bulge has developed for this value of $\Delta t = 0.1t$. In the case of $0.125t$ the bulge is even larger, appearing approximately as a local buckle. As a consequence, the local moment capacity has been reduced significantly and the pipe has locally lifted off the reel. Accordingly the local curvature in Fig. 4.9a is off the scale. This constitutes a significant local damage to the structure that would be hard to detect in an actual operation. It will however affect the integrity of the line during unreeling.

All four $\Delta D/D$ plots in Fig. 4.9b show the same values away from the discontinuities. The two lower values of Δt cause rather small disturbances in ΔD, but for $0.1t$ the presence of the local bulge is reflected as a significant disturbance. For $0.125t$ the much larger bulge again throws the local ΔD off the scale. The strain plots in Fig. 4.9c show similar trends; the local disturbance is small for the two lower values of Δt, quite significant for $0.1t$ and large for the largest thickness discontinuity.

When the pipes are unwound, the local curvature is reduced to very small values for the two smaller Δt but a certain amount of local disturbance remains for $0.1t$ (Fig. 4.10a). By contrast, for $0.125t$ the local damage inflicted to the pipe during winding was too large and, on the way to getting straightened, collapsed by developing a sharp kink at the discontinuity shown in Fig. 4.11b. The $\Delta D/D$ plots in Fig. 4.10b show residual ovality after straightening with small differences between the thicker and thinner sides. The discontinuities produce only small local disturbances for the two lower values of Δt and a larger one for $0.1t$. The strain plots in Fig. 4.10c show an increase in the local strain of the top generator for the three cases considered, with the residual local strain being larger for $0.1t$.

In summary, the results indicate that for this pipe/reel system, the combination of $\Delta t = 0.1t$ and $T = 0.025T_o$ appears to be on the boundary of being reelable while pipes with larger thickness discontinuities are not.

4.2.4 Effect of the Constitutive Model Adopted

For many calculations involving inelastic mechanical behavior of pipelines, isotropic hardening suffices. In the case of the reeling installation process, unwinding a reeled pipeline and straightening it involve unloading and reverse loading that bring into play the Bauschinger effect of the material response. As illustrated in the uniaxial setting in Fig. 2.2, isotropic hardening does not capture the rounding exhibited on reverse loading. In this section we examine the effect of this stiffer material model on the reeling/unreeling process through an example. It has the same basic pipe and material parameters as those in Table 2.2 with a pipe thickness discontinuity of $\Delta t = 0.1t$, wound/unwound at a back tension of $T = 0.05T_o$. The calculation is performed first with the nonlinear kinematic model outlined in Section 2.1 and then using isotropic hardening.

Figure 4.12 compares predictions of the local disturbances in curvature, change in diameter, and strain during reeling using the two constitutive models. Figure 4.13 compares the corresponding values after the pipes are unreeled. Both models predict the expected disturbance in curvature caused by reeling (Fig. 4.12a) but the disturbance is somewhat larger for isotropic hardening. The disturbance in ΔD is also more pronounced (Fig. 4.12b) while the ovality of the pipe away from the disturbance is smaller (see similar effect in Corona and Kyriakides [1988] using a different kinematic hardening model). Isotropic hardening causes also a slightly larger local increase in strain in the tensioned generator also (Fig. 4.12c). The differences here are not that large and further evaluation of which is actually closer to an actual application can only come from a careful experiments (e.g., Kyriakides and Mok [1992], Kyriakides [2016]).

A much more significant difference is observed on unreeling (Fig. 4.13). Whereas kinematic hardening shows the disturbance in curvature (Fig. 4.13a), ΔD (Fig. 4.13b) and plastic strain (Fig. 4.13c) to get reduced, isotropic hardening predicts the pipe to buckle at the discontinuity as demonstrated by the deformed configurations in Fig. 4.14. This of course causes the plots of the three disturbances in Fig. 4.13 to go off the scales. Due to the change in direction of the applied moment during straightening, the buckle is again on the top side of the pipe. Clearly this drastic difference in behavior is the result of the much stiffer material response of the isotropic hardening model on reverse loading. Although the problem parameters in this example were chosen to illustrate the buckling vs. no buckling outcome of using the two constitutive models, the results indicate that isotropic hardening is inappropriate for reeling and should be avoided.

4.2.5 Effect of Yield Stress Discontinuity

As mentioned in the introduction, pipes for offshore applications are produced to a minimum specified longitudinal yield stress. Small differences in the thermomechanical processing through which the pipes are produced invariably result in variations in yield stress even for pipes originating from the same heat. Thus, discontinuity in yield stress in adjacent stings of pipe in a pipeline is inevitable and must be considered. Realizing that girth welds and the associated heat affected zones tend to complicate such joints, we idealize them as a sharp difference in yield stress as shown Fig. 4.15. Here we examine the effect of such yield stress discontinuities on a reeling/unreeling cycle using the pipe/reel parameters in Table 4.1, a tension of $0.025T_o$, and the following values of yield stress differences: $\Delta\sigma_o / \sigma_o = \{0.05, 0.10, 0.15\}$. Figure 4.16 shows the local effects of the three yield stress discontinuity values on the usual variables during reeling, and Fig. 4.17 the corresponding ones during unreeling. For $0.05\sigma_o$ the discontinuity has a minimal effect on all three variables. A discontinuity of $0.1\sigma_o$ has a more pronounced but still small local effect on all three variables (see also corresponding deformed image in Fig. 4.18a). By contrast, when the discontinuity is increased to $0.15\sigma_o$ the pipe develops a local bulge that is displayed in Fig. 4.18b. Apparently the local bending rigidity has declined causing the neighborhood of the discontinuity to lift off the reel. The combined effect is a significant disturbance in the curvature, a corresponding one in $\Delta D/D$ with the local strain increasing to nearly 10%. Clearly, this is a dangerous development for the pipeline.

The dangerous situation becomes more critical on unreeling when the pipe buckles at the discontinuity as demonstrated in Fig. 4.18b. For the other two discontinuity values the reeling/unreeling leaves behind small disturbances in curvature and ovality whereas the strain disturbance for $0.1\sigma_o$ reached a level of about 6%, which of course is

large enough to require a more detail failure analysis. The results for $0.15\sigma_o$ are very similar to those of the thickness discontinuity of $\Delta t = 0.125t$ in Figs. 4.9-11. In both cases a bulge developed during reeling which lead to a local buckle during unreeling. In both cases straightening causes the buckle to occur on the opposite side of the initial bulge. Clearly, these and additional results indicate that a yield stress discontinuity is equally detrimental as a thickness discontinuity and deserves similar attention in designing a pipeline reeling protocol.

4.2.6 Effect of Reel Radius

The bending strain induced by reeling depends on the ratio of the pipe diameter and the diameter of the reel (Eq. (3.1)). The bending strain in turn affects the disturbance caused by a discontinuity in thickness or yield stress in the pipeline. So here we compare results for the base case pipe geometric and material properties that is first reeled/unreeled on a 324 in (8.23 m) radius reel at a tension of $0.025T_o$ with one that is reeled on a 286 in (7.26 m) radius reel. The pipelines have a thickness discontinuity of $\Delta t = 0.05t$. Figure 4.19 compares the effects of the discontinuity on the local curvature, ovality and strain in the reeled condition and Fig. 4.20 the corresponding results after unreeling. The disturbance in curvature for the pipe on the smaller radius reel is seen in Fig. 4.19a to have the same amplitude as that of the base case but is shifted to the higher curvature imposed by the smaller ρ. The ovality is also increased by the tighter radius but the amplitude of the local disturbance at the discontinuity is not changed (Fig. 4.19b). The strain in the most tensioned generator increases in accordance with Eq. (3.1), but again the amplitude of the local disturbance does not change (Fig. 4.19c). Unreeling results in somewhat larger residual curvature (Fig. 4.20a), residual ovality (Fig. 4.20b) and residual plastic strain (Fig. 4.20c) than for the larger reel radius but the amplitudes of

the local disturbances are quite similar. Overall, a smaller reel radius induces larger curvature, ovality and bending strain and thus discontinuities such as the ones considered in this study tend to have more severe consequences. Clearly an increase in pipe diameter has a similar effect as change in the reel radius so this is not attempted here.

4.2.7 Effect of Pipe Wall Thickness

The pipe D/t affects the extent to which it can be bent free of wrinkling or local buckling instabilities (Ju and Kyriakides [1992], Kyriakides and Corona [2007]). In this section we compare reeling/unreeling results for the base case pipe geometric, material properties and reel radius, to those of a pipeline with the same diameter but a wall thickness of 0.708 in (18.0 mm) so that the D/t is lowered to 18.0. We wind/unwind the two pipelines at $T = 0.025T_o$, which implies that a higher net tension level is applied to the thicker pipe. The two pipelines have a thickness discontinuity of $\Delta t = 0.05t$, which again implies a larger net value of Δt for the thicker one. Figure 4.21 compares the effects of the discontinuity on the local curvature, ovality and strain in the reeled condition, and Fig. 4.22 the corresponding results after unreeling. The curvature imposed to the two pipes by the reel away from the discontinuity is the same. The difference observed in Fig. 4.21a is introduced by the change in the normalizing variable $\kappa_1 = t / D_o^2$. The disturbance in curvature at the discontinuity is however somewhat smaller for the thicker pipe. In Fig. 4.21b the additional thickness reduces the ovality induced by conforming to the reel curvature, and the amplitude of local disturbance at the discontinuity is reduced somewhat also. The strain in the most tensioned generator depends mainly on the diameter, so since the diameters of the two pipes are the same the strain is the same including the disturbance at the discontinuity (Fig. 4.21c).

Unreeling and straightening leaves behind a larger local curvature disturbance for the thinner wall pipe (Fig. 4.22a). The residual ΔD is also smaller for the thicker wall pipe and so is the residual local disturbance in this variable (Fig. 4.22b). The residual strain in Fig. 4.22c is at very similar levels for the two pipes.

Overall, as expected, increasing the wall thickness of a pipeline of a given diameter tends to reduce the disturbance caused by discontinuities and the overall degradation of the pipe.

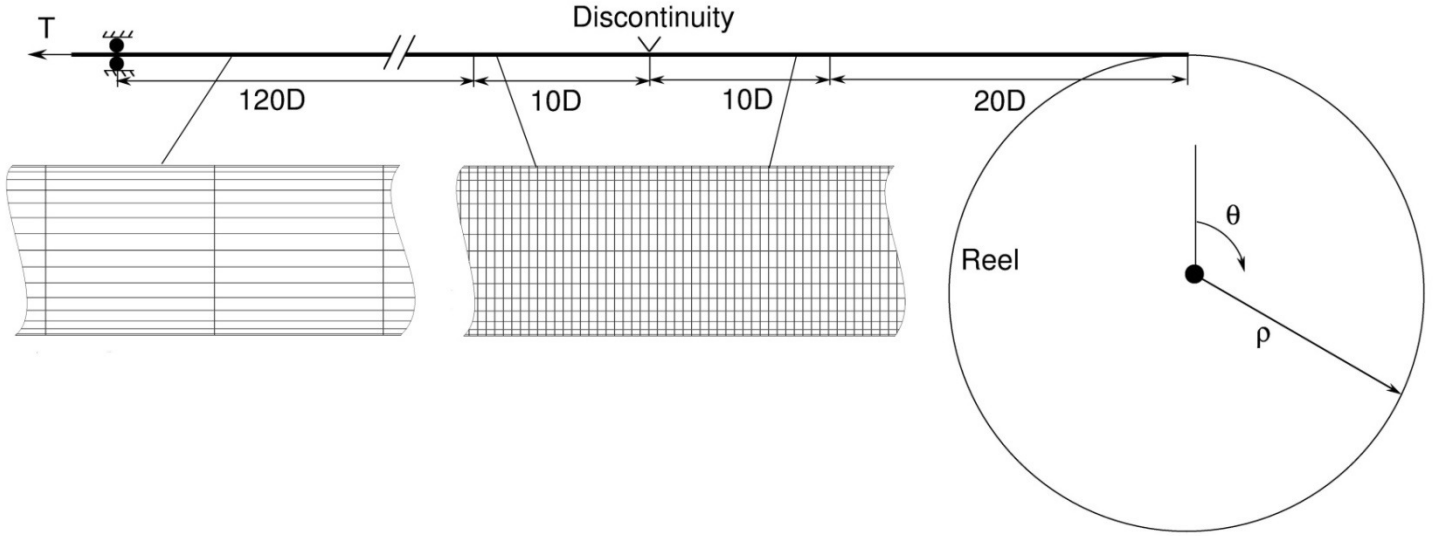

Figure 4.1 Geometry of the reel/pipeline finite element model.

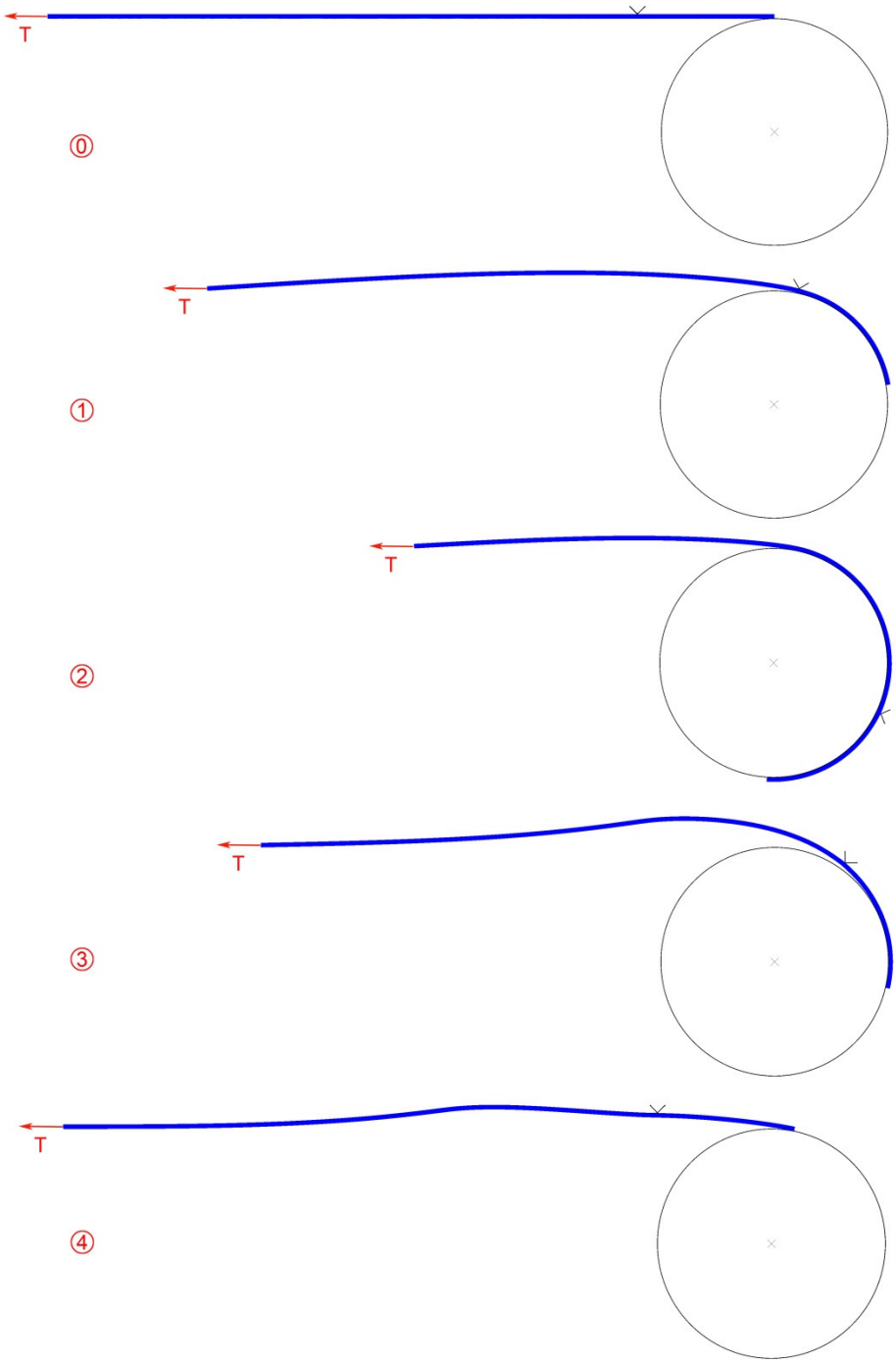

Figure 4.2 Calculated pipeline configurations during reeling ⓪-② and unreeling ③ & ④ for the base case parameters: $T = 0.02T_o$, $\Delta t = 0.1t$.

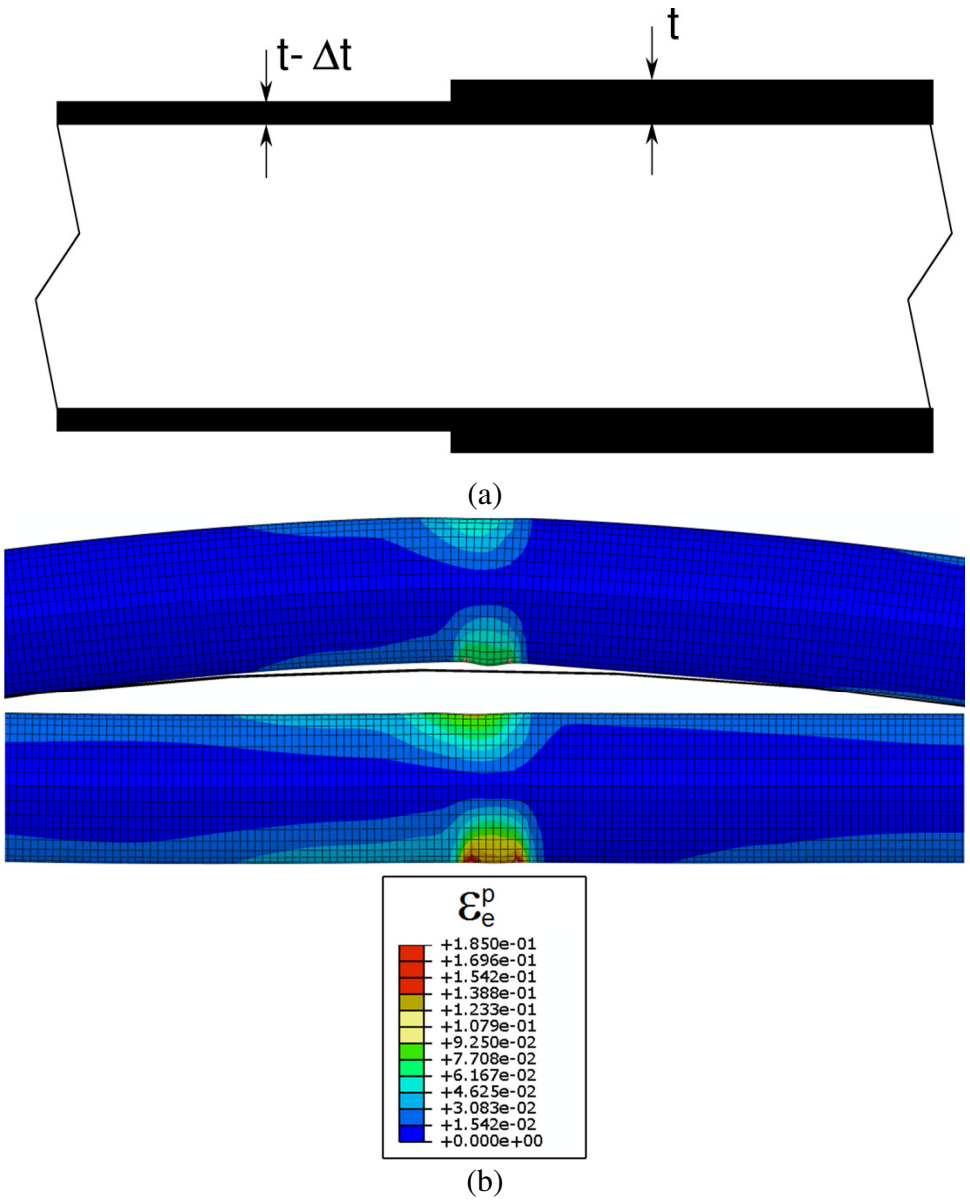

Figure 4.3 (a) Schematic of idealized wall thickness discontinuity. (b) Pipe deformed configurations of the neighborhood of the discontinuity after reeling (top) and after unreeling (bottom) for the base case parameters.

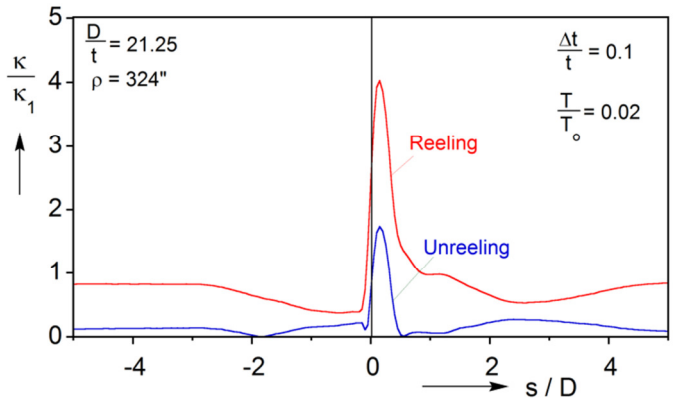

(a)

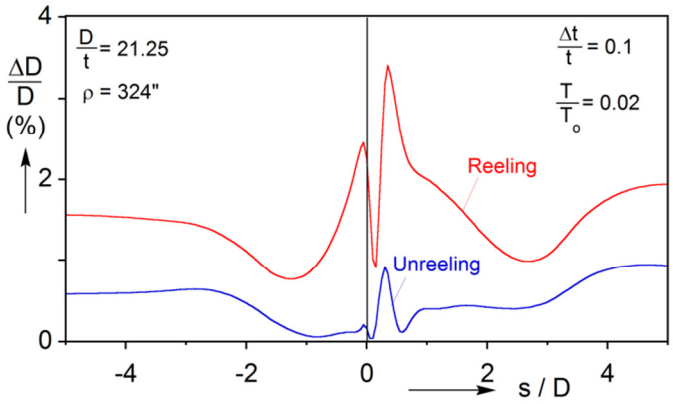

(b)

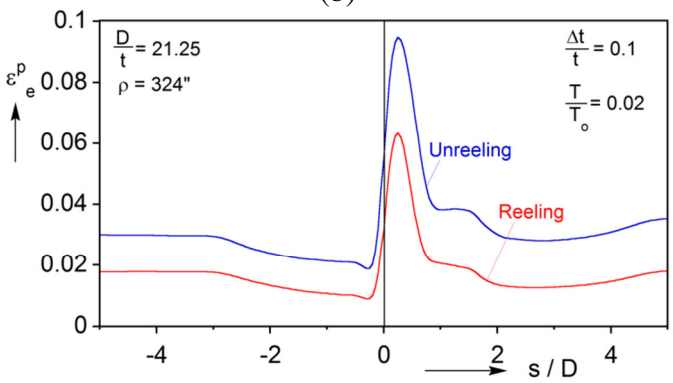

(c)

Figure 4.4 Effect of thickness discontinuity of $\Delta t = 0.1t$ on: (a) the mid-surface curvature, (b) change in diameter in the plane of bending and (c) equivalent plastic strain on the pipe generator at the top after reeling and unreeling for the base case parameters.

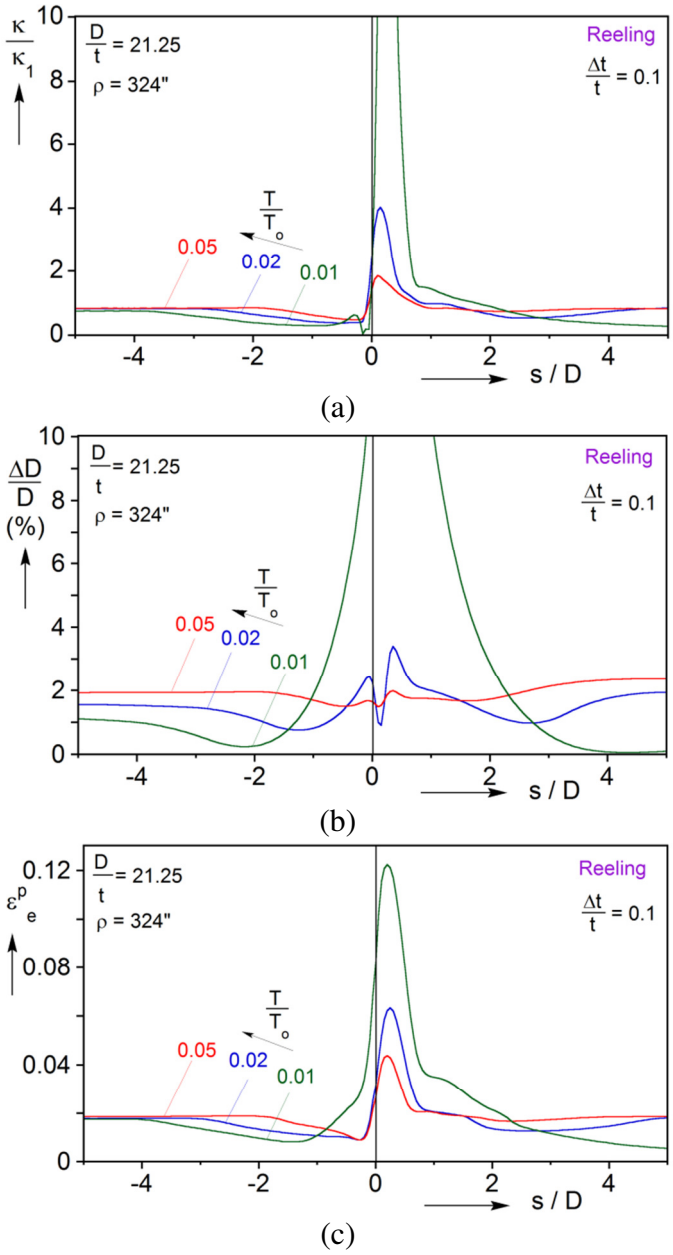

Figure 4.5 Effect of back tension on: (a) mid-surface curvature, (b) change in diameter and (c) equivalent plastic strain after reeling for $\Delta t = 0.1t$.

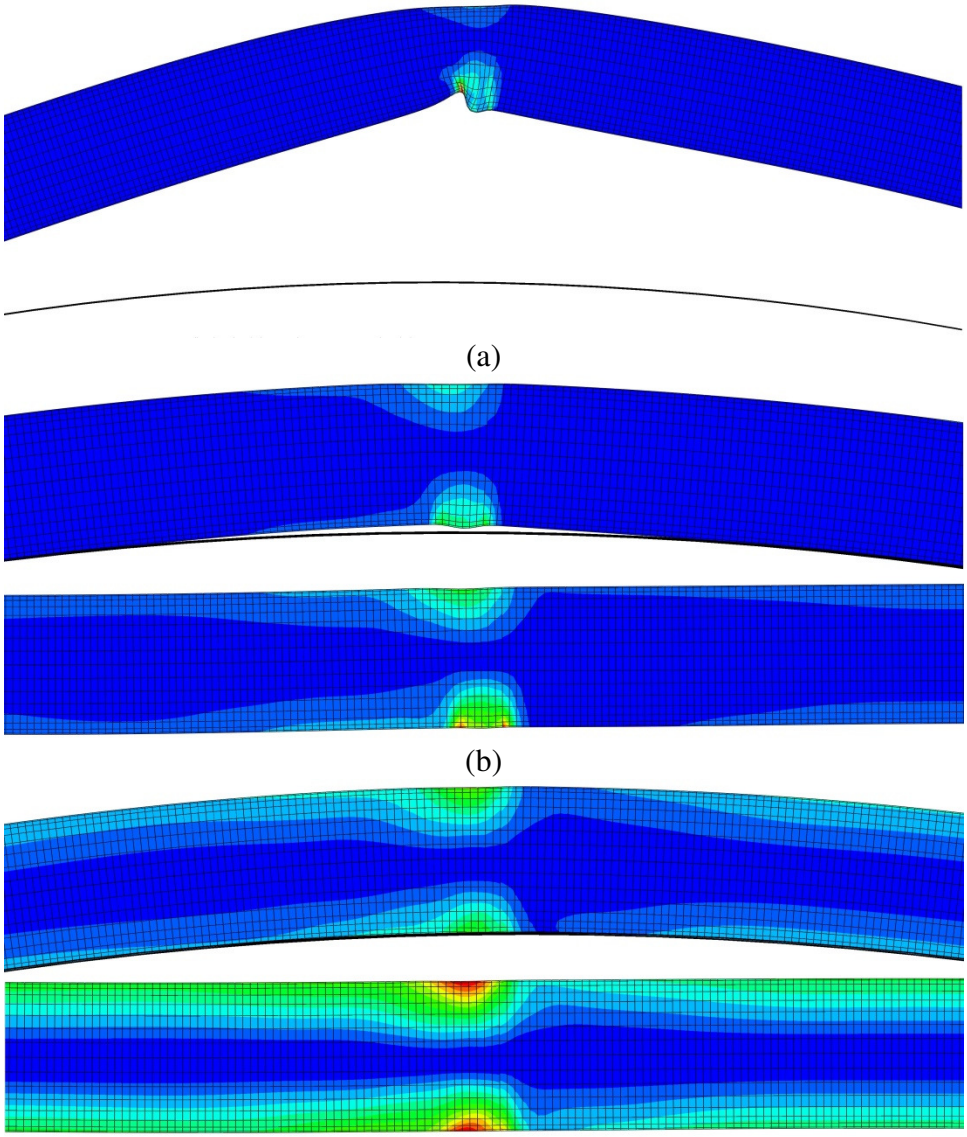

Figure 4.6 Pipe deformed configurations of the neighborhood of the discontinuity after reeling (top) and after unreeling (bottom) corresponding to results in Figs. 4.5 and 4.8 for T = (a) $0.01T_o$, (b) $0.02T_o$ and (c) $0.05T_o$.

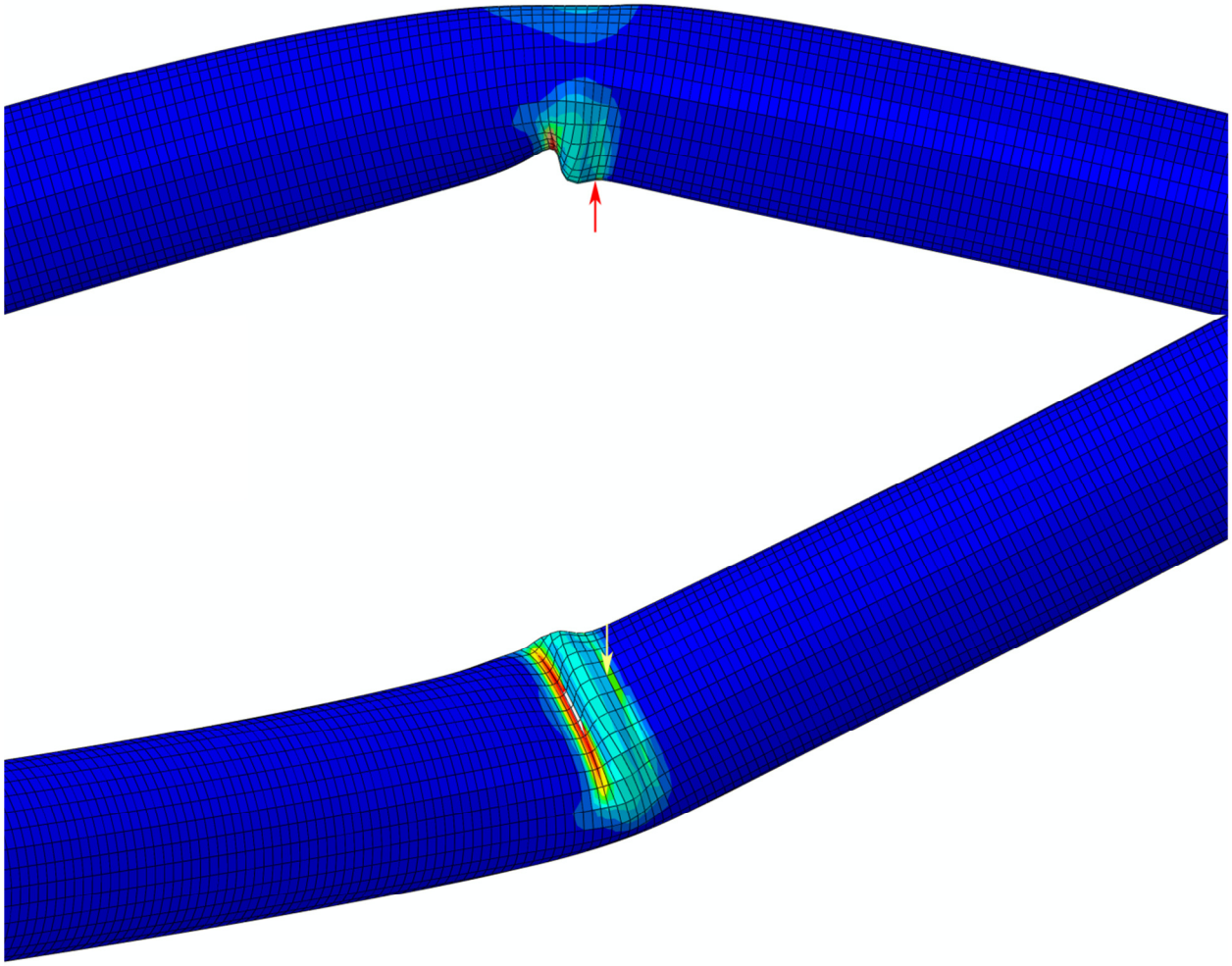

Figure 4.7 Expanded views of the buckle that developed during reeling for $T = 0.01T_o$ in Fig. 4.6a.

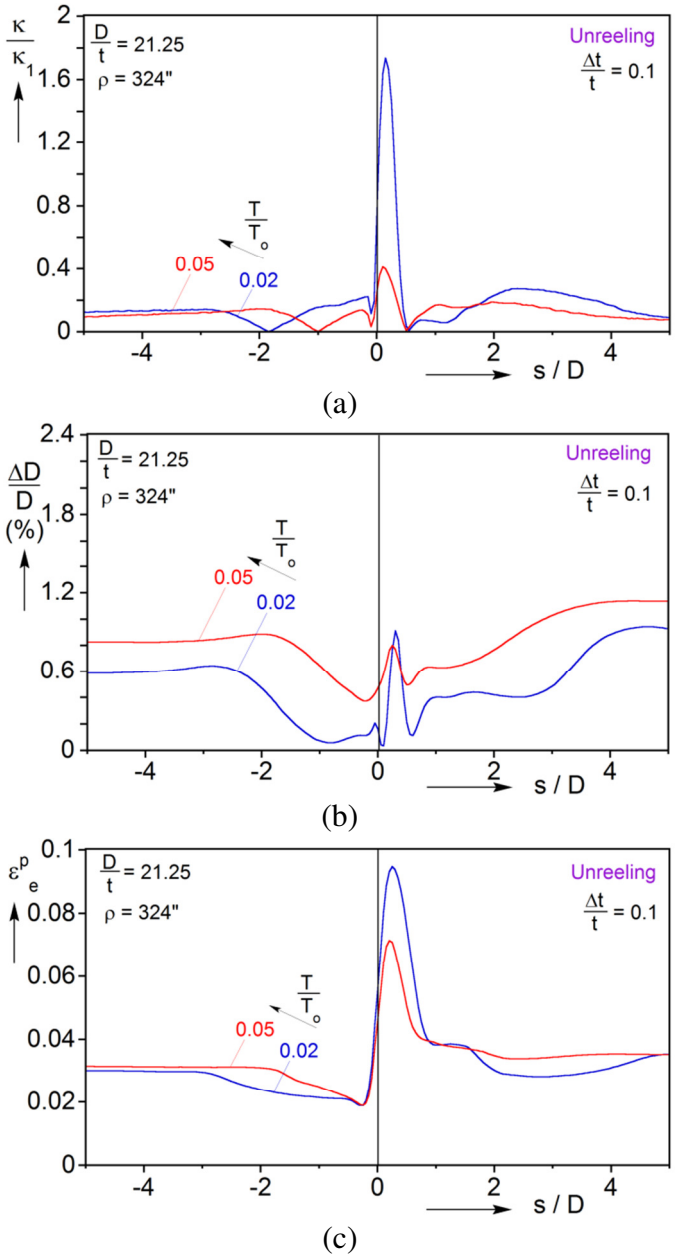

Figure 4.8 Effect of back tension on: (a) mid-surface curvature, (b) change in diameter and (c) equivalent plastic strain after unreeling for $\Delta t = 0.1t$.

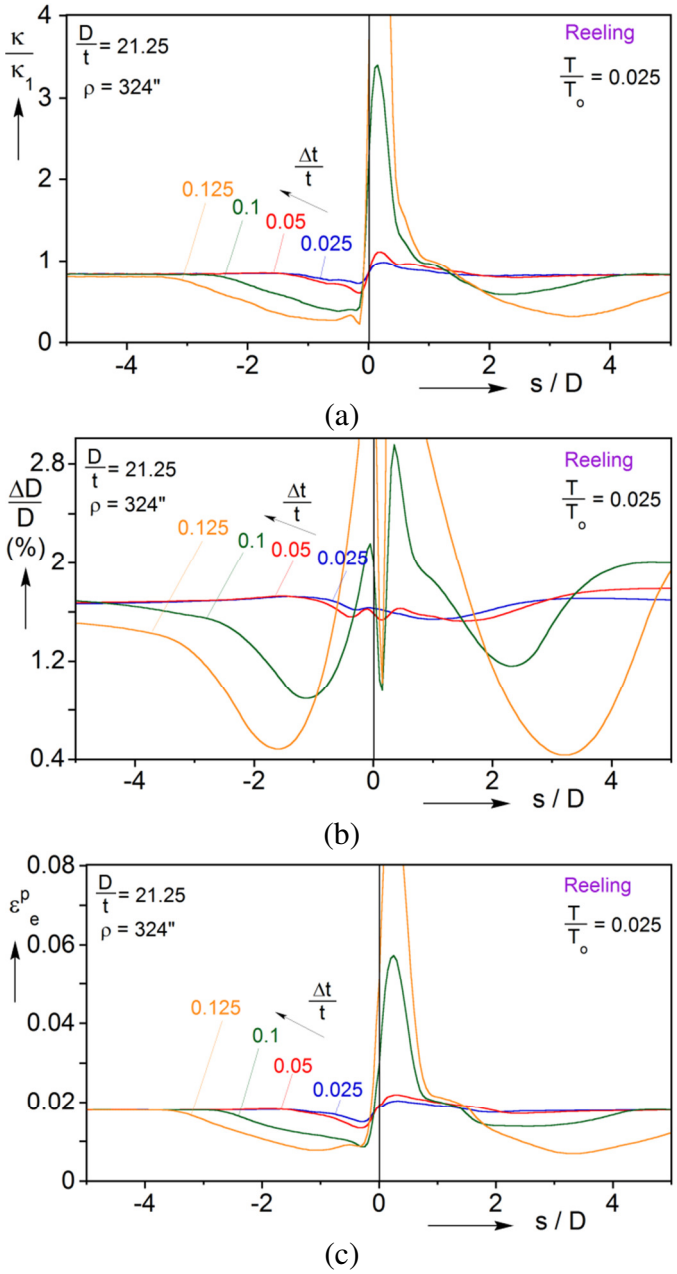

Figure 4.9 Effect of thickness discontinuity on: (a) mid-surface curvature, (b) change in diameter and (c) equivalent plastic strain after reeling for $T = 0.025T_o$.

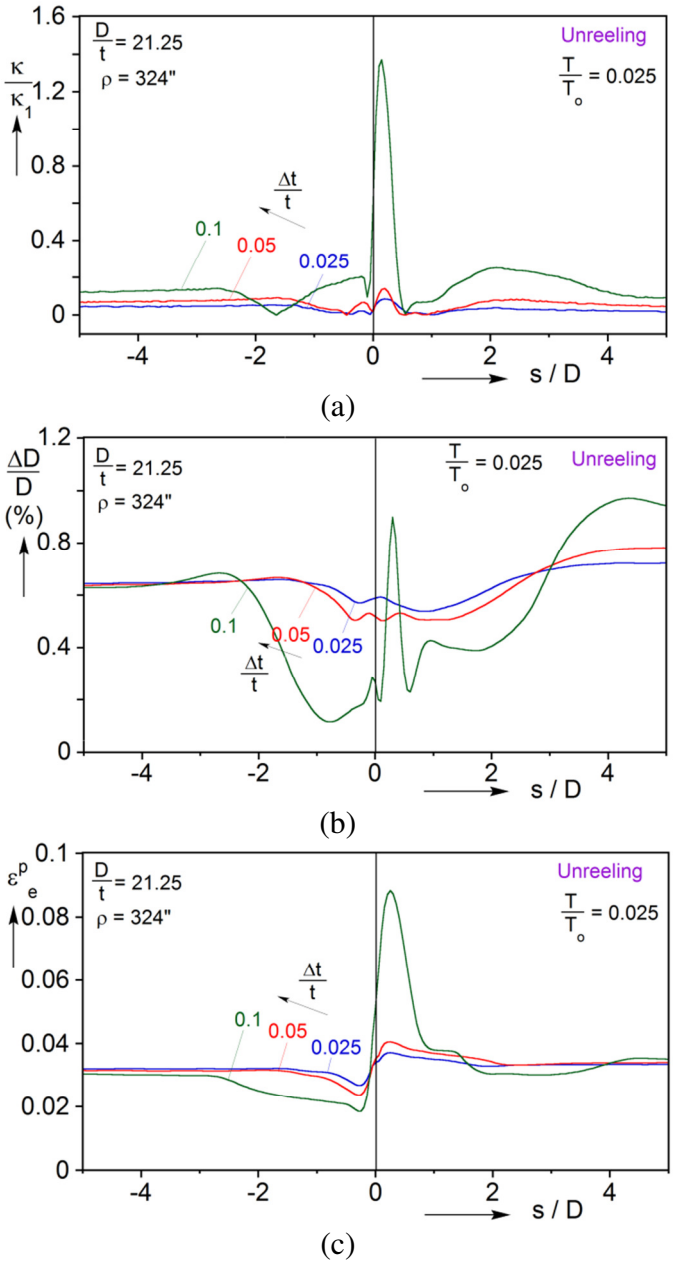

Figure 4.10 Effect of thickness discontinuity on: (a) mid-surface curvature, (b) change in diameter and (c) equivalent plastic strain after unreeling for $T = 0.025T_o$.

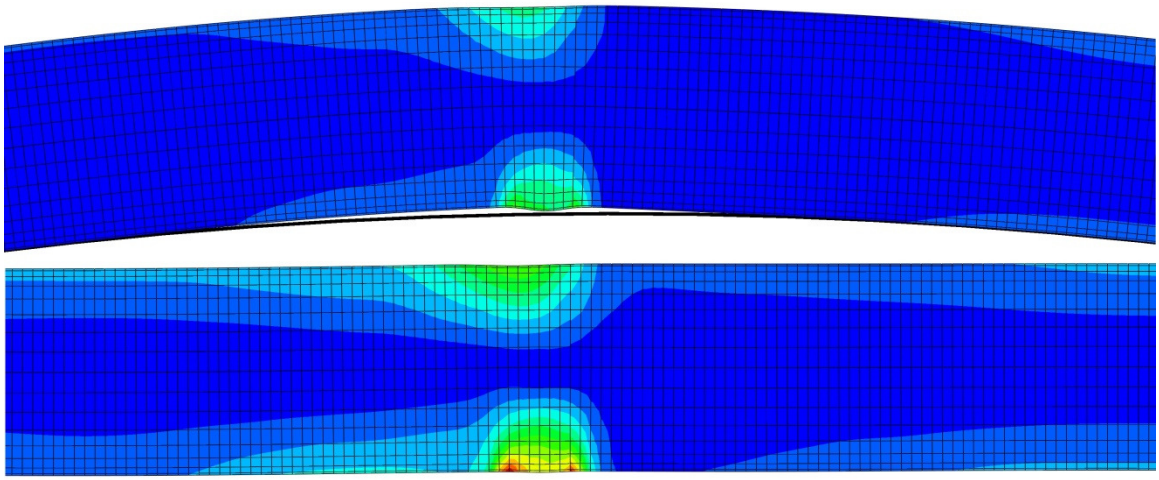

(a) $\Delta t = 0.1t$

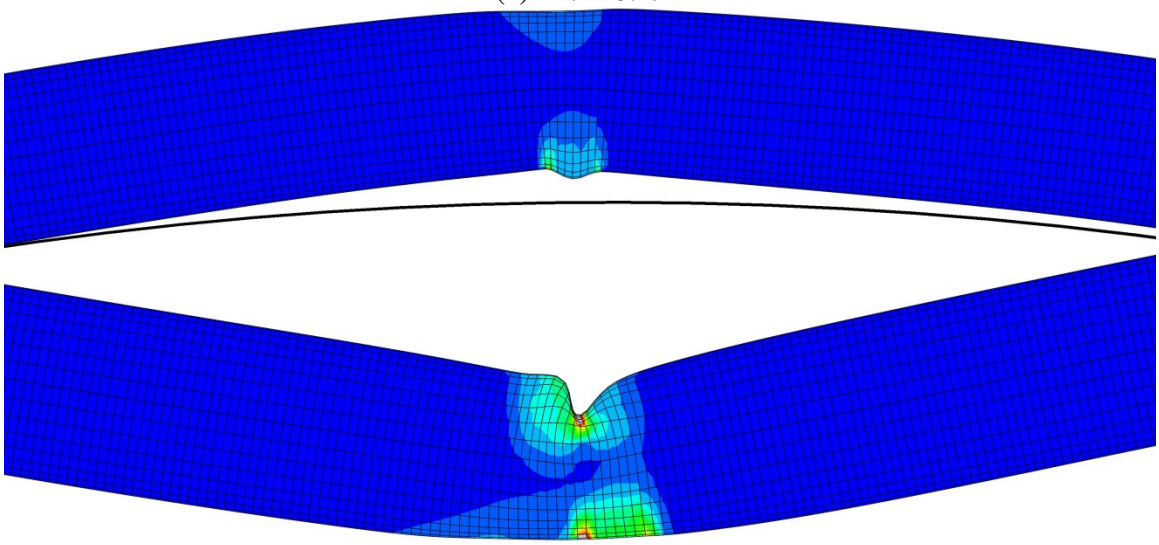

(b) $\Delta t = 0.125t$

Figure 4.11 Pipe deformed configurations of the neighborhood of the discontinuity after reeling (top) and after unreeling (bottom) corresponding to results in Figs. 4.9 and 4.10 for $\Delta t =$ (a) $0.1t$ and (b) $0.125t$.

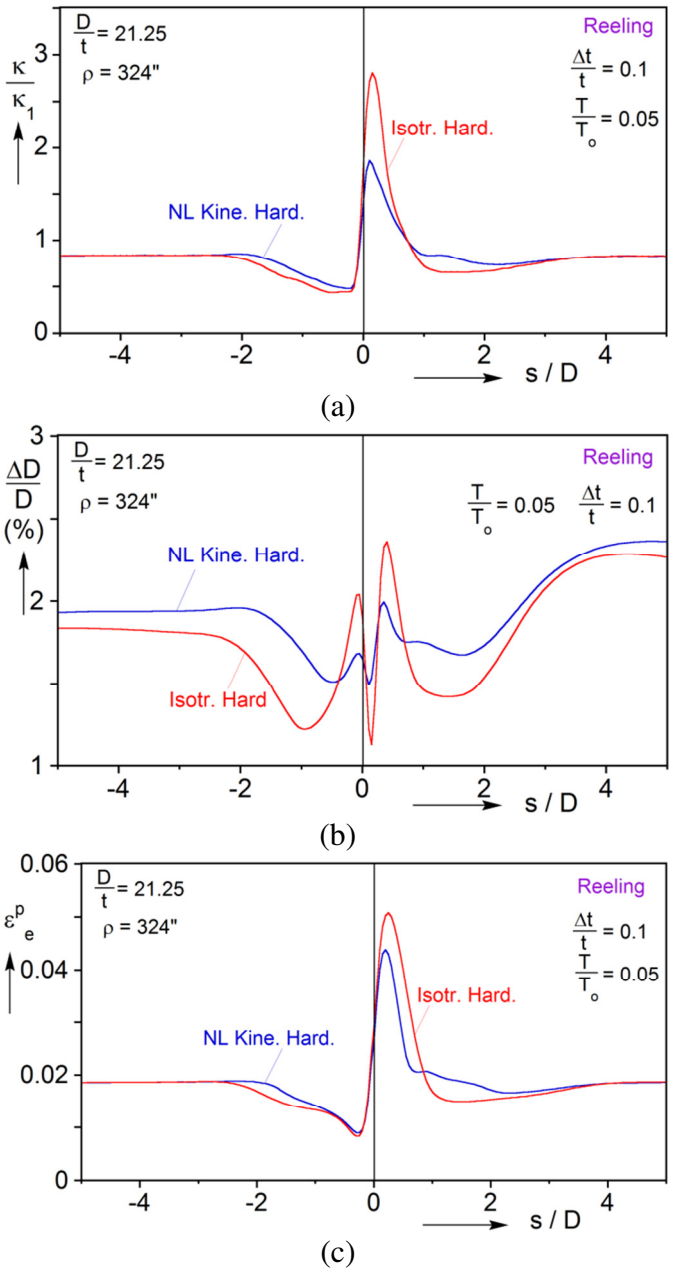

Figure 4.12 Effect of constitutive model on: (a) mid-surface curvature, (b) change in diameter and (c) equivalent plastic strain after reeling for isotropic hardening and nonlinear kinematic hardening for $T = 0.05T_o$ and $\Delta t = 0.1t$.

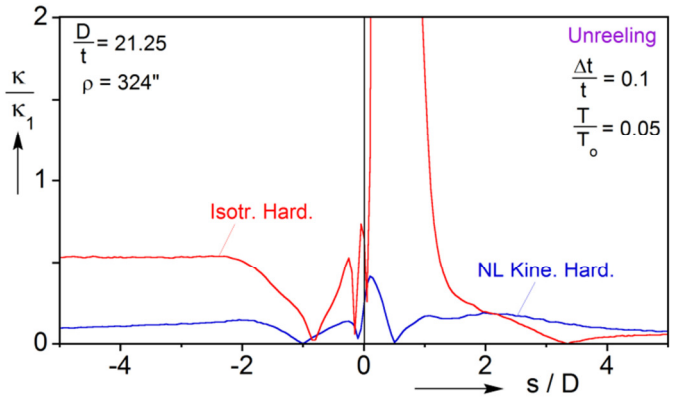

(a)

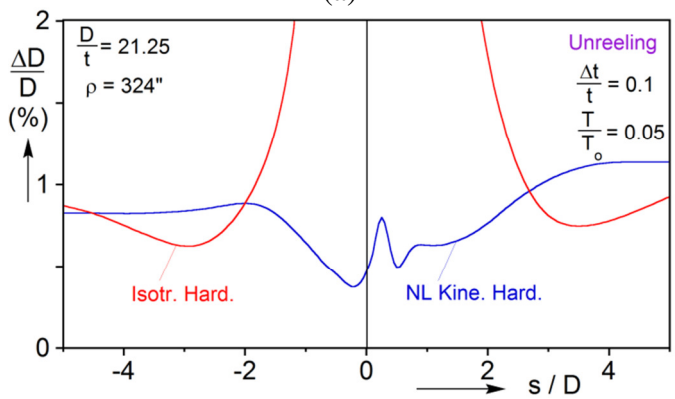

(b)

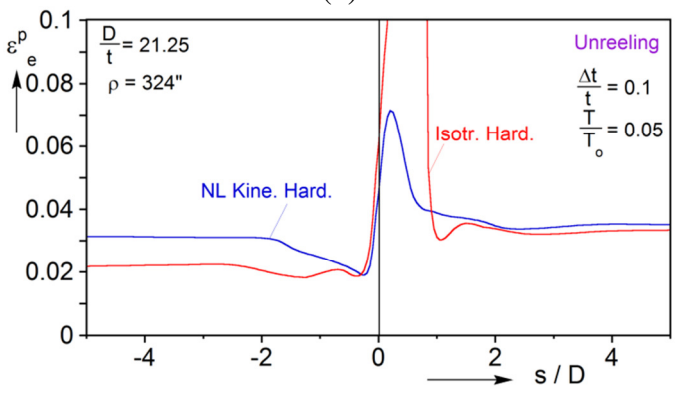

(c)

Figure 4.13 Effect of constitutive model on: (a) mid-surface curvature, (b) change in diameter and (c) equivalent plastic strain after unreeling for isotropic hardening and non-linear kinematic hardening for $T = 0.05T_o$ and $\Delta t = 0.1t$.

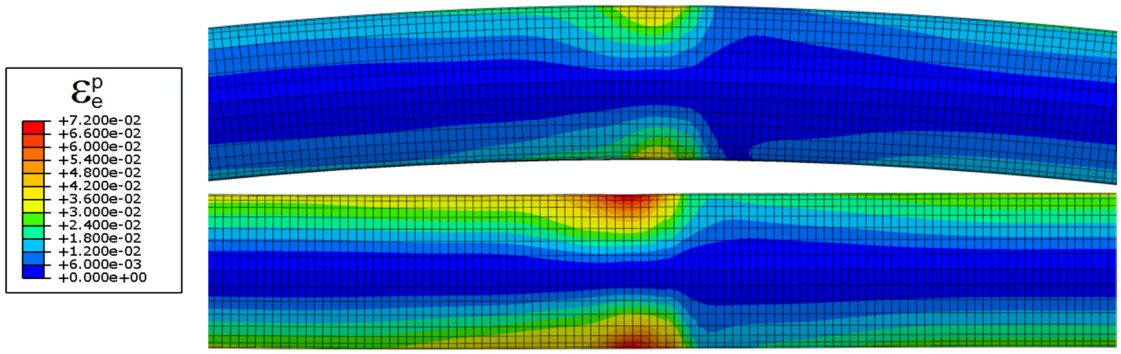

(a) Kinematic Hardening

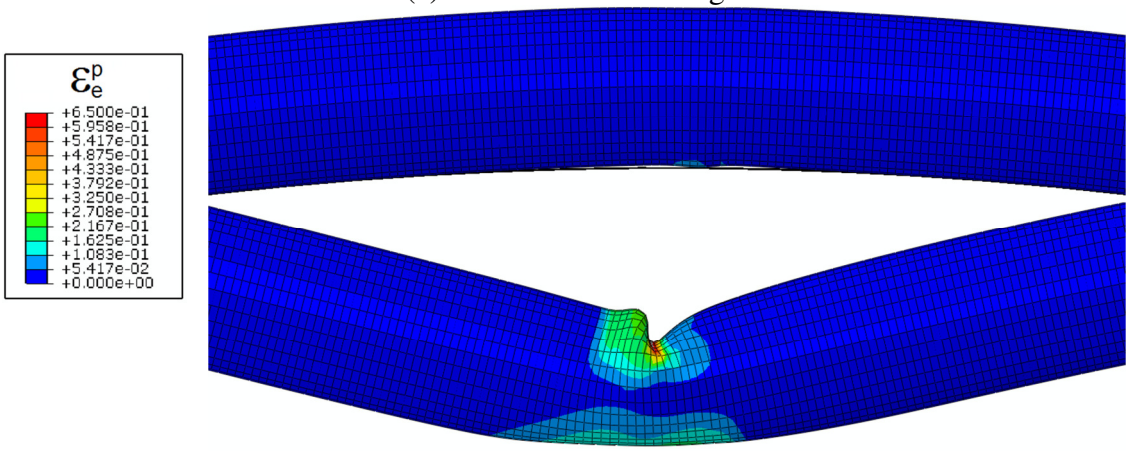

(b) Isotropic Hardening

Figure 4.14 Pipe deformed configurations of the neighborhood of the discontinuity for (a) kinematic hardening and (b) isotropic hardening. Top images correspond to reeling in Fig. 4.12 and bottom ones to unreeling in Fig. 4.13.

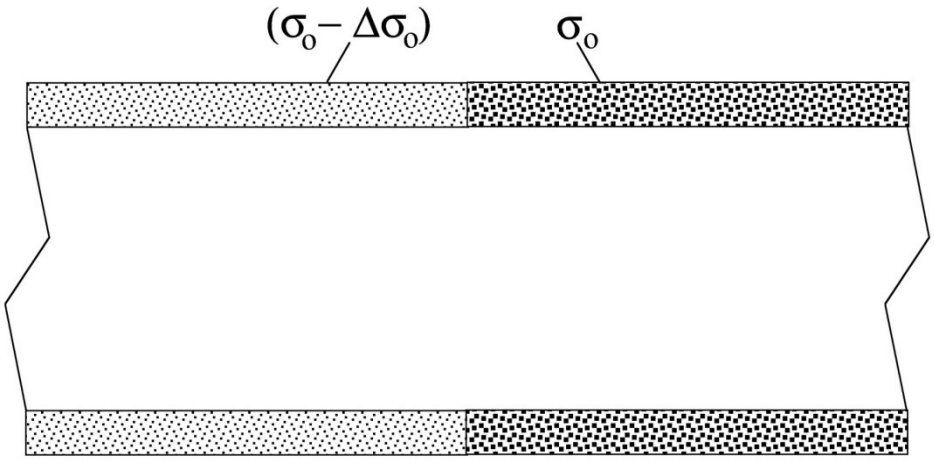

Figure 4.15 Schematic of idealized yield stress discontinuity.

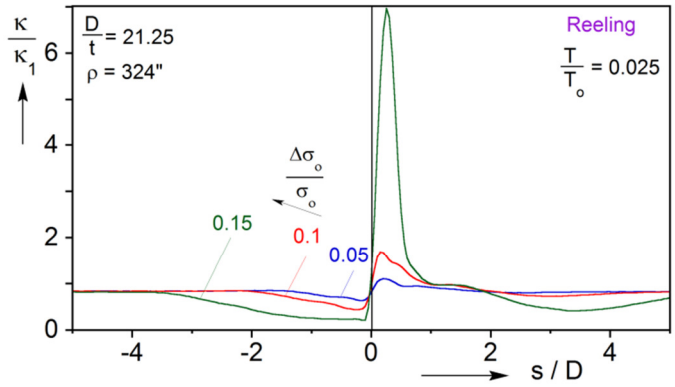

(a)

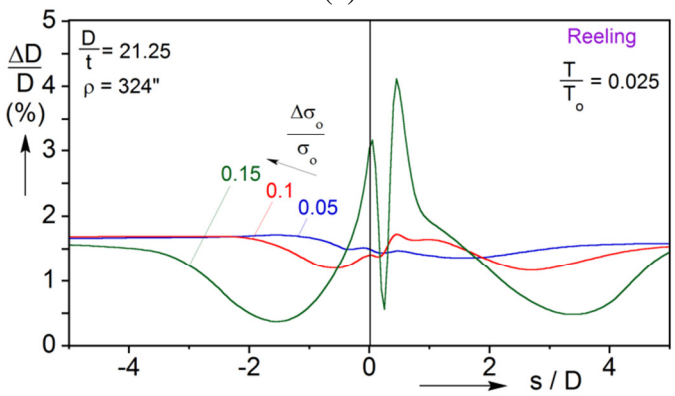

(b)

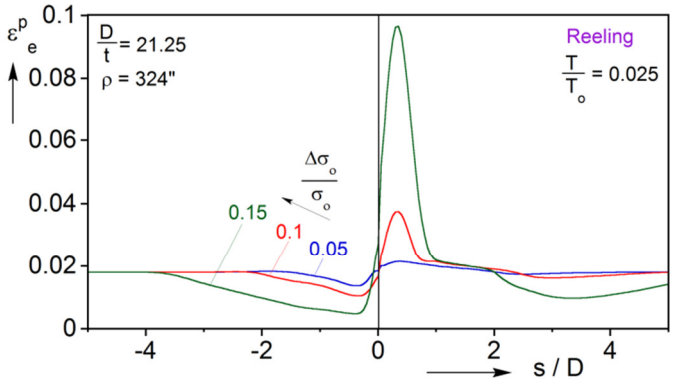

(c)

Figure 4.16 Effect of yield stress discontinuity on: (a) mid-surface curvature, (b) change in diameter and (c) equivalent plastic strain after reeling for $T = 0.025T_o$.

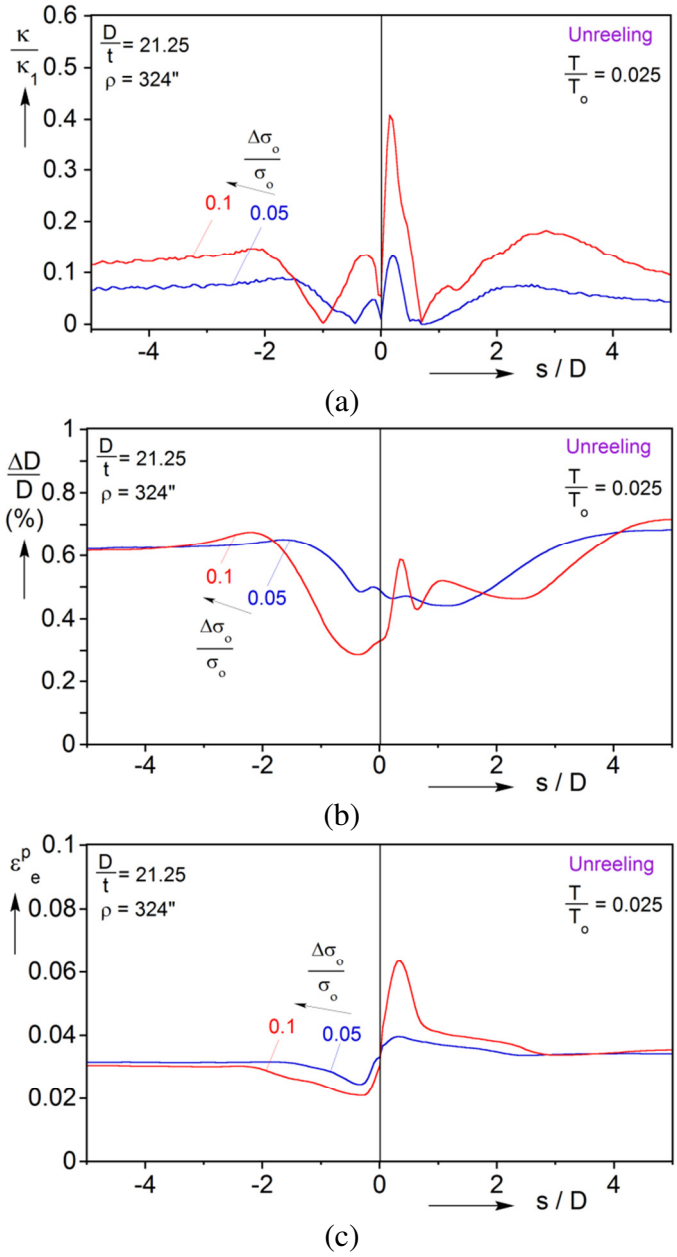

Figure 4.17 Effect of yield stress discontinuity on: (a) mid-surface curvature, (b) change in diameter and (c) equivalent plastic strain after unreeling for $T = 0.025T_O$.

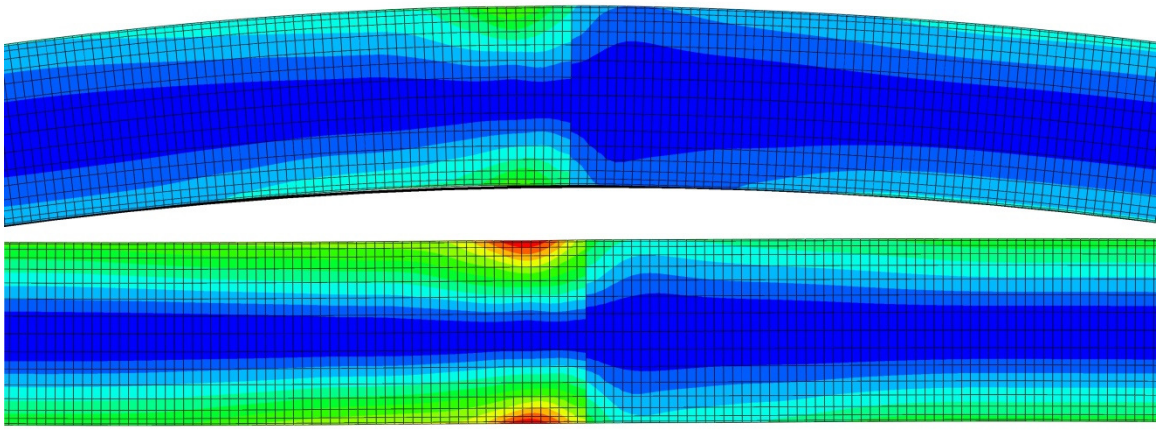

(a) $\Delta\sigma_o = 0.1\sigma_o$

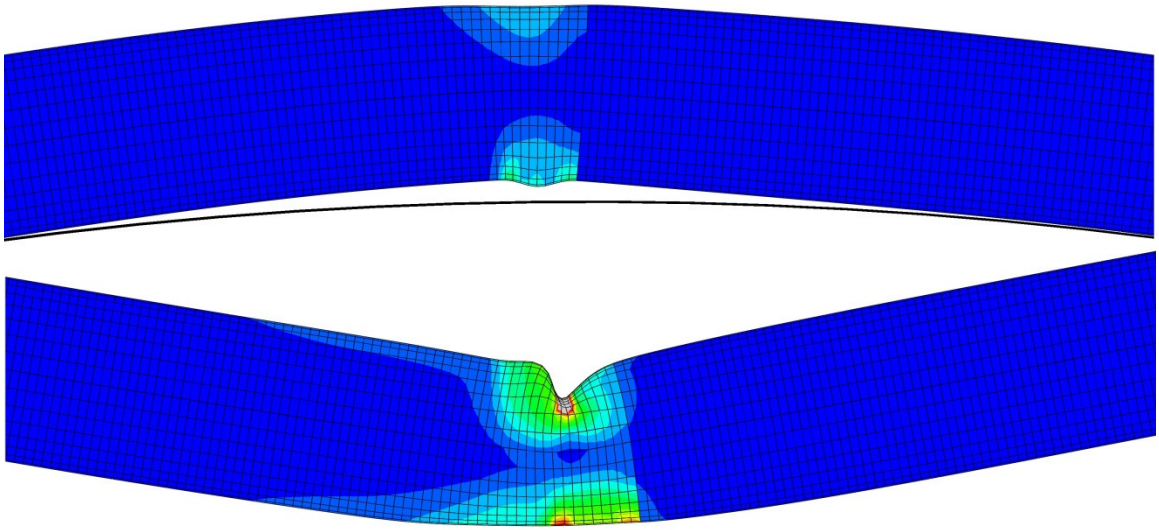

(b) $\Delta\sigma_o = 0.15\sigma_o$

Figure 4.18 Pipe deformed configurations of the neighborhood of the discontinuity for (a) $\Delta\sigma_o = 0.1\sigma_o$ and (b) $\Delta\sigma_o = 0.15\sigma_o$. Top images correspond to reeling in Fig. 4.16 and bottom ones to unreeling in Fig. 4.17.

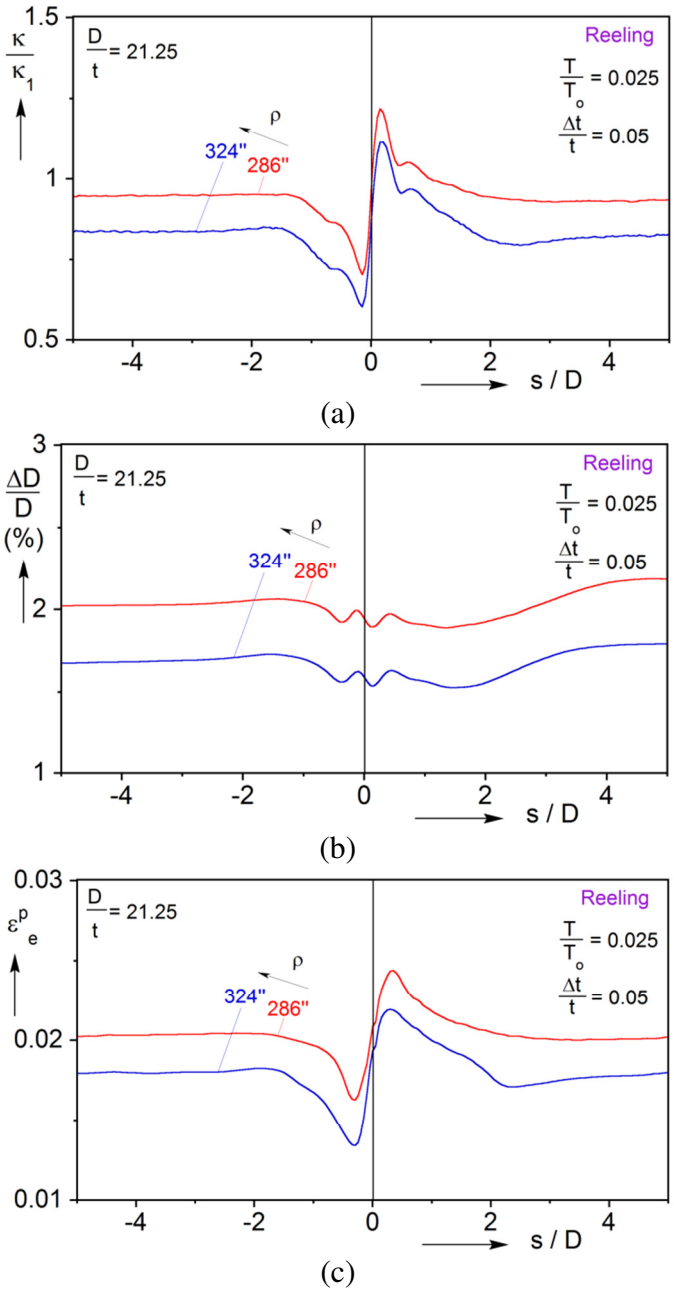

Figure 4.19 Effect of reel radius on: (a) mid-surface curvature, (b) change in diameter and (c) equivalent plastic strain after reeling for $T = 0.025T_o$ and $\Delta t = 0.05t$.

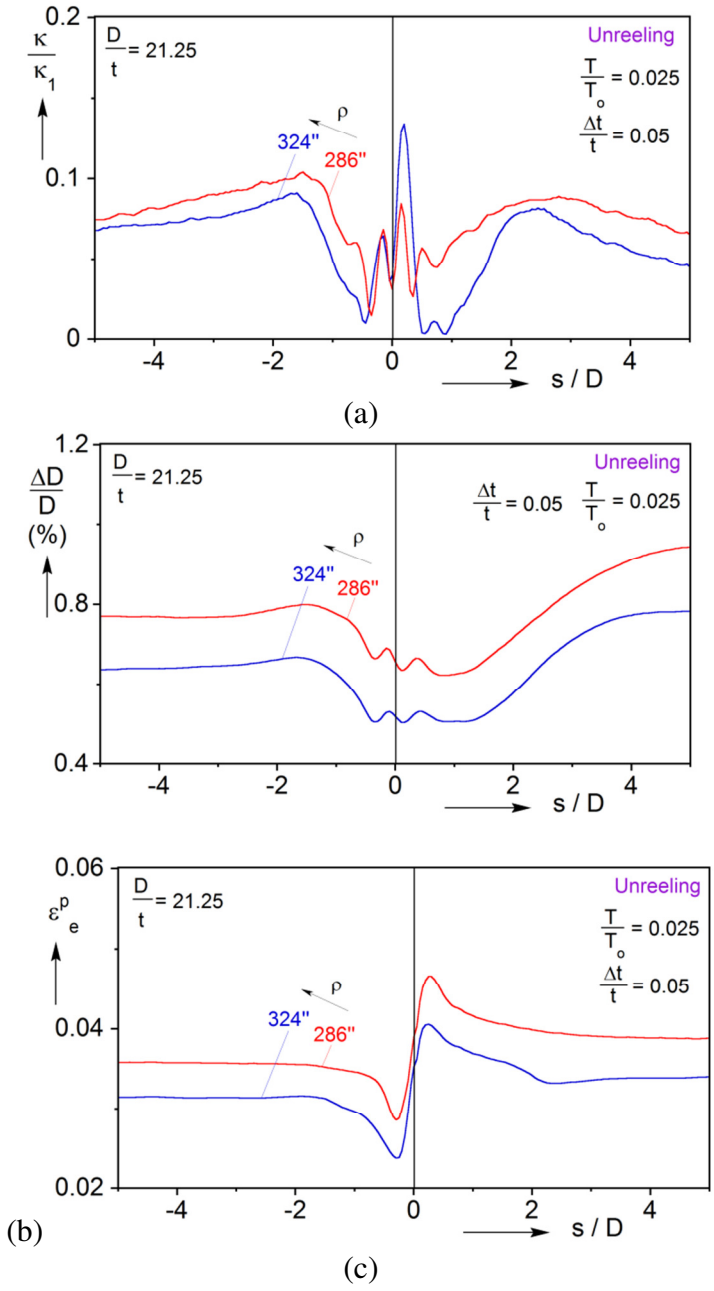

Figure 4.20 Effect of reel radius on: (a) mid-surface curvature, (b) change in diameter and (c) equivalent plastic strain after unreeling for $T = 0.025T_o$ and $\Delta t = 0.05t$.

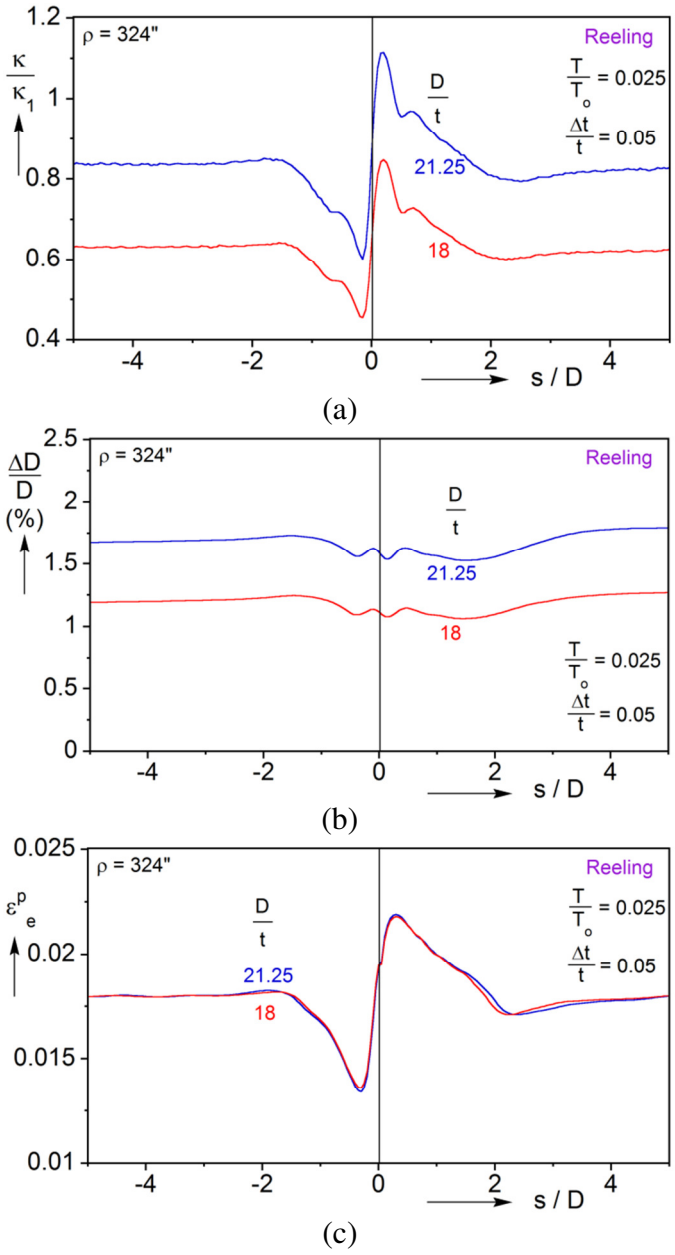

Figure 4.21 Effect of *D/t* on: (a) mid-surface curvature, (b) change in diameter and (c) equivalent plastic strain after reeling for $T = 0.025T_o$ and $\Delta t = 0.05t$.

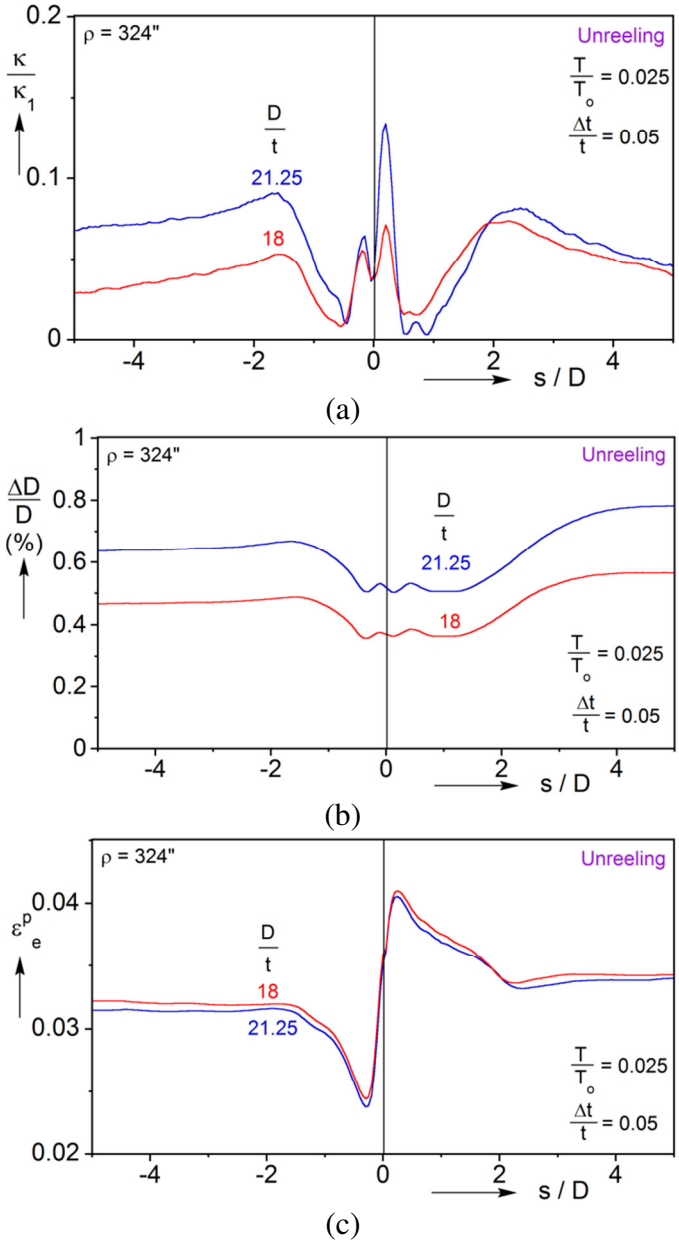

Figure 4.22 Effect of *D/t* on: (a) mid-surface curvature, (b) change in diameter and (c) equivalent plastic strain after unreeling for $T = 0.025T_o$ and $\Delta t = 0.05t$.

Chapter 5: REELING OF PIPE WITH LÜDERS BANDS[5]

Lüders banding is a dislocation governed material instability, which macroscopically manifests as discontinuous deformation. Bending of tubes with a material that exhibits Lüders banding (see Hallai and Kyriakides [2011a, 2011b]) results in banded, localized deformation organized in diamond-shaped pockets on the tensioned and compressed sides of the tube. Furthermore, the Lüders-deformed section exhibits higher ovalization and curvature than the rest of the structure. Under deformation controlled bending, the higher deformation and curvature tend to propagate until the whole length of the structure is so deformed. As a consequence of the clustering of Lüders bands, the ovalization develops axial undulations. Such undulations can act as imperfections in subsequent, particularly compressive, loadings of the structure.

In this chapter, the effect of Lüders banding on a reeled pipe is examined numerically. As the pipe approaches the reel, it bends and eventually conforms to the reel surface and comes in contact with it. The length of the line where it transitions into reel curvature is controlled by the back tension applied by the tensioner mounted on the installation ramp (see Fig. 1.1 and Kyriakides and Corona [2007]). Consequently, the transition length of pipe close to the point of contact sees a variable curvature. Furthermore, contact with the reel is thought to provide some support that may delay collapse. The objective of this investigation is to understand how these differences from pure bending affect the mechanical behavior and integrity of a pipeline that exhibits Lüders banding. The problem is studied using a large-scale three-dimensional finite element framework similar to the ones presented in Chapters 3 and 4. The material is

[5] Liu, Y., Kyriakides, S. and Hallai, J.F. (2015). Reeling of pipe with Lüders bands. *Int'l J. Solids Structures*, **72**, 11-25. (The author implemented the constitutive model, conducted the numerical simulations, and analyzed the results.)

modeled using a stress–strain response with a negative slope over the extent of the Lüders deformation. The effects of problem variables such like the Lüders strain, the applied tension, the ratio of the reel diameter to that of the pipe, and the pipe diameter-to-thickness ratio on the pipe mechanical behavior is examined.

5.1 LÜDERS BANDING

Lüders banding is a material instability that can be microscopically explained using dislocation dynamics. Cottrell and Bilby [1949] attributed the upper yield stress to the pinning of dislocations by carbon and nitrogen atoms that tend to form "atmospheres" around them. They postulated that initial yielding requires a higher stress to pull the dislocations out of their atmospheres, but once released, they can be moved by a lower stress. The reappearance of Lüders strain following mild heat-treatment (*strain aging*) that allows impurities to migrate and repin the dislocations supports this concept. Johnston and Gilman [1959] attributed the initial load drop to multiplication of dislocations. Indeed, simple considerations of dislocation motion put forward initially by Johnston and Gilman, and further exploited by Hahn [1962], demonstrated that up-down-up stress-strain responses like ones measured in LiF crystals could be derived from such a premise (see also Johnston [1962]).

A simple demonstration of the macroscopic effects of Lüders banding is illustrated in Fig. 5.1 that shows results from a tensile test on a strip of low carbon steel (LCS) pulled at a constant displacement rate of $\dot{\delta} = 10^{-4} L \; s^{-1}$ ($L \equiv$ length of the test section; from Hallai and Kyriakides [2013]). Figure 5.1a shows the recorded nominal stress-normalized displacement response and Fig. 5.1b a set of full field contours of axial strain recorded with digital image correlation (DIC). The response rises elastically to a stress peak (σ_U) and is followed by a stress plateau (σ_L) that extends over a strain of

$\Delta\varepsilon_L$ (*Lüders strain*). Following the initial load maximum, deformation localizes on the left-hand side (LHS) of the specimen and gradually propagates to the right while the load remains essentially unchanged. Two deformation regimes co-exist in the test section as the stress plateau is traced: on the right the specimen is essentially elastic with a strain that corresponds to the beginning of the stress plateau while the left section is plastically deformed to the strain that corresponds to the end of the extent of the plateau (~2.65%). An inclined front that propagates to the right at a velocity $c = \dot{\delta} / \Delta\varepsilon_L$ separates the two deformation regimes. When the whole specimen is Lüders deformed, the material starts hardening and subsequently the test section deforms uniformly. Similar results produced without the quantitative benefit of DIC can be found in Butler [1962], Hall [1970], Kyriakides and Miller [2000], and Loucheand Chrysochoos [2001] among others; results using other full-field deformation monitoring methods are not reviewed for brevity. It is well established that Lüders variables $\{\sigma_U, \sigma_L, \Delta\varepsilon_L\}$ depend on the alloy content, grain size, strain rate and temperature. Furthermore, these factors influence also the localization patterns that develop.

5.1.1 Modeling of Lüders Banding

A physically based constitutive model of Lüders instability is challenging because of the number and complexity of factors that govern its extent. Generalization of the 1-D dislocation multiplication model of Hahn [1962] associated with the first load drop by Shioya and Shioiri [1976], and its further exploitation by Yoshida *et al.* [2008] are noteworthy but require empirical adjustments for them to be implemented in structural analyses (see also Yoshida [2000]). Kyriakides and co-workers have followed a more phenomenological but equivalent approach that introduces an unstable material response over the extent of the Lüders stress plateau as shown in Fig. 5.2 (e.g., see Shaw and

Kyriakides [1998], Tsukahara and Iung [1998], Kyriakides and Miller [2000], Corona et al. [2002], Aguirre et al. [2004], Kyriakides et al. [2008], Zhang et al. [2008], Hallai and Kyriakides [2011b]). The initial elastic part of a measured response is adopted; it terminates at the upper yield stress that is $\Delta\sigma/2$ higher than the measured stress plateau. It is followed by a linear softening branch whose termination point at the end of the plateau is at a level that makes the areas of the two shaded triangles equal (i.e., $\sigma_L \equiv$ *Maxwell stress*, Ericksen [1975], Kyriakides [2001], Abeyaratne and Knowles [2006]). Beyond this point, the fit follows the hardening part of the measured stress-strain response. Hallai and Kyriakides [2013] recently extracted the "underlying material response" of a LCS over the Lüders affected regime (see also Shioya and Shioiri [1976]). It provides an estimate of σ_U and confirms the softening nature of the underlying response. Although the actual trajectory of the softening branch is nonlinear, this difference from the assumed linear softening was found not to play a significant role in the induced localization patterns that develop in the problems considered. We thus continue to represent the material response as illustrated in Fig. 5.2 with its slope calibrated in the manner described in the next section.

5.2 ANALYSIS

5.2.1 Finite Element Model

The process of winding a pipe onto a circular drum was modeled in ABAQUS as follows. The reel is represented as a circular rigid surface of radius R_r. One end of a long section of pipe (100D for the cases presented) is connected to the reel as shown in Fig. 5.3 while its other end is placed between rollers that prevent vertical but allow free horizontal motion of the line. A constant level of tension (T) is applied on the left end, and the line is wound by applying incrementally a rotation (ϕ) to the reel.

It has been previously demonstrated that during bending of a tube Lüders banding manifests as inclined narrow bands of localized deformation with jumps in strain of the order of the Lüders strain. Capturing such events requires a fully 3-D discretization and a fine mesh. Although this choice is not unique, we have found ABAQUS's incompatible elements C3D8I best suited for the problem (Aguirre et al. [2004], Kyriakides et al. [2008], Hallai and Kyriakides [2011b]). These are linear elements enhanced to allow for the deformation gradient inside the element to vary while displacement continuity is maintained (see Wilson et al. [1973], Ortiz et al. [1987], Nacar et al. [1989], Simo and Armero [1992]).

Symmetry about the plane of bending allows consideration of one half of the pipe cross section. Two mesh densities and element types are adopted: a very fine mesh of C3D8I elements for the length of pipe that will be wound onto the reel ($15D$), and a courser mesh of C3D8 elements for the rest of the pipe ($85D$). The $15D$ length that comes in contact with the reel is sufficient to ensure that the effects of Lüders banding on the pipe reach steady state. The length of the section that remains straight is chosen to ensure that the interaction of the pipe with the reel at the point of first contact is representative of actual operations. The following mesh densities were arrived at from convergence studies aimed to ensure the veracity of the banded deformation patterns that develop:

The finer mesh section has 2 elements across the thickness, 72 elements around the half circumference, and 40 elements per pipe diameter along the length. In the case of the main pipe dimensions used in this study (see top row of Table 5.1), this distribution provides for a nearly isotropic mesh on the surface of the pipe. This mesh density is fine enough to capture the bands of localized deformation that develop, which is one of the main goals of the study. The courser mesh length has 2 elements across the thickness, 18 elements around the half circumference, and 4 elements per diameter in the axial

direction. The end of the model on the RHS is "connected" to the reel by kinematically coupling all translational and rotational degrees of freedom of the nodes in the pipe end cross section to a reference node on the rigid surface.

The reel was modeled as an analytical rigid surface. Contact with the deformable pipe is modeled using a strict “master-slave” algorithm of ABAQUS, with the reel surface as the master and the pipe as the slave surface. The contact is frictionless but “finite sliding” is allowed between a contact pair. An exponential “softened” contact pressure-overclosure relationship is used with 500 psi (3.4 MPa) and 0.0001 in (0.00254 mm) being representative pressure and clearance values respectively.

The material is modeled as a finitely deforming J_2-type elastic-plastic solid that hardens/softens isotropically. The model is calibrated to the true stress-logarithmic strain version of a non-monotonic stress-strain response like the one shown in Fig. 5.2. The induced softening is mild and terminates within a few percent of deformation. Consequently the problem’s mesh sensitivity is limited. Despite this, a “mild” rate dependence is introduced by incorporating the commonly used powerlaw expressed as:

$$\left(\frac{\dot{\varepsilon}^p}{\dot{\varepsilon}_o}\right)^m = \frac{\sigma}{\Sigma(\varepsilon^p)}, \tag{5.1}$$

where $\dot{\varepsilon}_o$ is a reference strain rate, $\Sigma(\varepsilon^p)$ is the measured stress-strain response at this strain rate and m is the rate exponent typically chosen to be 0.001.

5.2.2 Reeling Simulation

The effect of Lüders banding on reeled pipe will now be demonstrated in detail through an example that involves a 12-inch pipe that is wound on a reel with a 300 in (7.62 m) radius. This arrangement induces a maximum bending strain of 2.08%, which of course plasticizes the pipe. The pipe has D/t = 24.0 and a material with a Lüders stress of

$\sigma_L = 65$ ksi (448 MPa), strain $\Delta\varepsilon_L = 2.5\%$ and a slope of the softening branch of $E' = -0.12E$ (see top row of Table 5.1). The reeling is performed with a back tension of $T = 0.05T_o$ that amounts to 66.2 kips (295 kN; $T_o \equiv$ yield tension).

Table 5.1 Major geometric and material parameters of example cases.

D in (mm)	t in (mm)	$\frac{D}{t}$	E Msi (GPa)	σ_L ksi (MPa)	$\frac{\Delta\sigma}{\sigma_L}$	$\frac{-E'}{E}$	$\Delta\varepsilon_L$ %	R_r in (m)	$\frac{T}{T_o}$	$\dot{\phi}$ rad/s
12.75 (323.9)	0.531 (13.5)	24.0	30 (207)	65.0 (448)	0.14	0.012	2.5	300 (7.62)	0.05	0.001
12.75 (323.9)	0.638 (16.19)	20.0	30 (207)	65.0 (448)	0.14	0.012	2.5	300 (7.62)	0.05	0.001
12.75 (323.9)	0.708 (17.92)	18.0	30 (207)	65.0 (448)	0.14	0.012	2.5	300 (7.62)	0.05	0.001

The results of the reeling simulation are illustrated in Figs. 5.4-5.7. Figure 5.4 portrays a set of seven configuration that show the pipe gradually coming into increasing contact with the reel which is rotated to an angle ϕ = 40.1° (0.70 rad). Superimposed on the deforming model pipe are contours of equivalent plastic strain. The contours clearly illustrate that Lüders banding results in clusters or pockets of deformation bands inclined to the axis of the tube. It is important to point out that for compatibility of deformation the bands necessarily affect the whole thickness of the tube. Each cluster of bands starts developing as the pipe is locally conforming to the curvature of the rigid surface. The bands are stronger, and affect a wider span of the cross section, in its upper half that experiences higher stress. These clusters of bands are periodic and are separated by relatively undeformed zones free of bands. Each cluster of bands at the top has a corresponding pocket on the bottom with the two cluster "centers" being diametrically opposite to each other. However, for this tension level, the lower half bands are weaker, cover a narrower angular span, and at least in the scale of the contours appear somewhat

more diffuse. By comparison, under pure bending the banded deformation pockets are more symmetric between the tensioned and compressed sides, they are nearly diamond shaped, and are not separated by space. These differences will be explained in the following sections.

The global bending history of the section of pipe being wound onto the reel is illustrated in Fig. 5.5. Figure 5.5a shows the slope of the mid-surface of the tube, $\theta(s)$, plotted against the natural coordinate s along the axis of the tube for the seven configurations in Fig. 5.4. The value of $\theta(s)$ plotted corresponds to the three-point average of the nodes along the mid-surface. Each trajectory is seen to start with $\theta(s)=0$ on the far RHS when the section is far away from the reel. It then smoothly transitions into a nearly linear trajectory that corresponds to the curvature of the reel ($\kappa = d\theta/ds$) when it comes into contact with it. The constant curvature section increases as more pipe is wound on the reel going from configuration ① to ⑦.

Figure 5.5b shows the corresponding normalized moment distributions along the $15D$ fine mesh length of pipe for the same seven configurations. Here

$$M = 2\sum_{i=1}^{N} z_i F_i, \tag{5.2}$$

with F_i representing the axial force acting on the i^{th} node on the cross section, z_i is its distance from the mid-surface of the tube, and M_o is the fully plastic moment of the section $(=\sigma_L D_o^2 t)$. Each trajectory starts with a relatively low moment while off the reel on the RHS. As a particular section approaches the reel, it gradually bends increasing the local moment. It reaches a maximum when it first contacts the surface of the reel. The moment maxima of trajectories ② to ⑦, are all very close to M_o, which corresponds to the moment plateau that develops for such responses under pure bending (see Hallai and Kyriakides [2011a, 2011b]). The s location of the maximum moment is marked on the

corresponding θ - s trajectory with a symbol "♦" in Fig. 5.5a. It is seen to correspond to the point at which $\theta(s)$ transitions to the value of $d\theta/ds$ that equals the curvature of the reel. The moment at a section in contact with the reel drops slightly as it moves around the reel and reaches a plateau with small undulations clearly seen in the moment trajectories of configurations ⑤, ⑥, and ⑦ in Fig. 5.5b.

In the way of presenting a more quantitative view of the deformation induced by the process, Fig. 5.6 shows plastic strain profiles along the top (T) and bottom (B) generators and along the tube mid-surface (M), corresponding to configurations ②, ④ and ⑦ (the reel rotation, ϕ, for each profile is listed in the figures). The top and bottom profiles exhibit the periodicity implied by the clustered nature of the bands of localized deformation while the mid-surface is seen to remain essentially plastically undeformed. Since the T and B profiles traverse the bands, both exhibit short wavelength undulations that are reminiscent of experimental observations of the banded nature of Lüders induced local deformation under pure bending (see Fig. 9 in Aguirre and Kyriakides [2004] and Fig. 17 in Hallai and Kyriakides [2011a]). Save for the first cluster that is influenced by the fixity of the tube end, the T strain clusters reach higher strain levels than the B ones and are separated by deeper valleys. The B profiles exhibit the somewhat more defuse character implied by the color contours in Fig. 5.4. Interestingly, the higher plastic strain peaks in the top reach levels that exceed 4%. We are reminded that the radius of the reel with which the pipe is in contact dictates a kinematic constraint of a maximum bending strain of 2.08%. Consequently, Lüders banding induced local deformation that is nearly double this value is incompatible with this constraint. This incompatibility is resolved by the banded clusters being separated by relatively undeformed sections of the tube so that the strain averages to the value imposed by the reel. The separation of the clusters is less severe on the bottom because here the Lüders induced strains are less severe. More

support for this mechanism will be provided in the next section in light of additional results. It is worth mentioning that taking the average of strains recorded in the top and bottom generators works out to essentially the bending strain imposed by the reel.

It is well known that bending induces ovalization to the pipe cross section (Brazier [1927], Kyriakides and Corona [2007]), and that reeling under tension tends to increase the ovalization. Since ovalization is a deciding parameter for the collapse pressure of the pipe, it is important that it be monitored. Figure 5.7 shows the evolution of the change in diameter of the pipe in the plane of bending ($\Delta D / D$) along the length as it comes into contact with the reel. Shown are the axial profiles of $\Delta D / D$ that correspond to the seven reeled pipe configurations in Fig. 5.4. Relating the ovalization profiles to the slope and moment profiles along the length of the pipe in Fig. 5.5a, it is clear that ovality starts growing as the pipe approaches the point of contact with the reel and reaches an average value of about 2.5% soon after that. Hallai and Kyriakides [2011b] reported that Lüders banding influences the induced ovalization under pure bending. This is partly reflected here through the undulations exhibited in the ovality profiles. Ovality peaks correspond to the location of clusters of bands and valleys correspond to the sections between them that develop less strain.

To illustrate the evolution of Lüders bands and the formation of a cluster, we concentrate on the development of one cluster that occurs between reel rotations of $29.5^{o} \le \phi \le 32.7^{o}$. Figure 5.8 shows a sequence of seven expanded images of the affected section of pipe with superimposed contours of equivalent plastic strain. Plastic strain axial profiles of the top and bottom generators corresponding to these configurations are shown in Fig. 5.9. Included in each figure is the corresponding normalized moment profile. Image ① shows a fully developed cluster on the right with the section next to it just coming into full contact with the reel. The corresponding strain profiles for both T

and B are also fully developed. Furthermore the moment maximum, which as mentioned above corresponds to the point of first contact of a section with the reel, is seen in Fig. 5.9 to have moved further along. In image ② inclined bands of localized deformation have initiated approximately 1.75D to the left of the center of the initial cluster. An associated spike in strain has appeared in image ② with the moment maximum lagging slightly behind. In image ③ the bands at the top have strengthened and multiplied, and several weaker bands have appeared at the bottom in the space between the original cluster and the new one being formed. The moment maximum is now coincident with the position of the largest strain spike at the top. In image ④ the bands at the top have strengthened further and so have the ones at the bottom. The strengthening and increase in the number of bands at the top continues in configurations ⑤ and ⑥ but simultaneously bands have now appeared directly below the newly formed cluster. In image ⑦ the moment maximum has moved further downstream and the new cluster is fully developed both at the top and bottom. As reported earlier, the bottom bands are somewhat more diffuse than the ones at the top covering also some of the space between the two clusters on the top.

In summary, the aim of this simulation was to demonstrate and understand the development of banded localization induced by Lüders banding. A 12-inch pipe with D/t of 24 and a Lüders strain of 2.5% has been wound on a reel that induces a bending strain of about 2.08% at a tension of $0.05T_o$. Lüders banding takes the form of inclined bands that organize themselves into clusters. For the case considered, because the local strains induced to the top of the pipe exceed the value imposed by the reel curvature, the clusters are separated by sections free of Lüders bands so that the bending strain averages out to the one imposed by the reel curvature. At the bottom the bands are somewhat more diffuse and exhibit a more regular distribution along the length. Again the strain along the

bottom generator averages out to the value imposed by the reel. The process induced an average ovalization of about 2.5% to the cross section, which in an external pressure collapse sensitive installation would be unacceptable. The clustering of localized deformation imposes axial undulations in cross sectional ovalization. Such undulations can act as imperfections in subsequent loadings of the structure. We emphasize that consideration of the possibility of wrinkling and collapse requires perturbation of the structure with appropriate geometric imperfections which is beyond the scope of the present study.

5.3 PARAMETRIC STUDY

We now examine the effects of various problem parameters of reeled pipe that exhibits Lüders banding on the localization patterns that develop and on other structural changes that result.

5.3.1 Effect of Lüders Strain

The extent of Lüders strain depends on factors like carbon and alloy content of the steel, thermomechanical processing of the pipe at the mill, etc., and can vary in finished seamless pipes. It is thus worth examining its effect on reeled pipe. To this end, we perform a series of reeling simulations using the 12-inch pipe listed in Table 5.1 with a similar X-65 stress-strain response in which the Lüders strain, $\Delta\varepsilon_L$, is varied between 1.0% to 3.5%. This is achieved by keeping the slope of the linear softening branch constant ($E' = -0.12E$) but varying $\Delta\sigma$ as shown below so that the plateau stress, σ_L, is kept at a constant level of 65 ksi (448 MPa) as shown in Fig. 5.10.

$\Delta\varepsilon_L(\%)$	1.0	1.5	2.0	2.5	3.0	3.5
$\Delta\sigma / \sigma_L$	0.056	0.084	0.112	0.140	0.168	0.196

The reeling simulations are performed using the same model geometry and mesh presented in Section 5.2.1. The overall mechanical behavior is similar to the one reported for $\Delta\varepsilon_L = 2.5\%$, but the induced Lüders deformation patterns differ. Figure 5.11 shows the deformed configurations of six models with different values of $\Delta\varepsilon_L$ after undergoing the same amount of reel rotation. Superimposed on each are contours of equivalent plastic strain. All have developed Lüders banding but the clustering of the bands, and the extent of the associated localized strain differ. Therefore, for clearer visualization a different color scale is adopted for each image. Figure 5.12 shows corresponding plots of plastic strain profiles along the top (T) and bottom (B) generators for each case.

The strain patterns and strain levels for $\Delta\varepsilon_L = 2.5\%$ are the same as in Figs. 5.4 and 5.6. For $\Delta\varepsilon_L = 2.0\%$, the clustering of bands continues at the top but their spacing has been reduced. Concurrently, the clustering on the bottom has almost disappeared. The strain levels in the top bands have been reduced with the maximum value being around 3.0% and a smaller amplitude of the strain undulations. This Lüders strain is closer to the bending strain imposed by the reel and this reduces the need for a longer zone of much smaller strain between the top pockets. At the bottom, the Lüders strain fluctuates around the value imposed by the reel.

Clusters of less intense bands are also visible at the top in the 1.5% Lüders strain configuration in Fig. 5.11, but here the space between them has almost disappeared. This is also reflected in the top strain profile in Fig. 5.12 while the one at the bottom is essentially linear and at the level imposed by the reel curvature. In fact, the relatively small undulations at the top are seen to also average out to the bending strain imposed by the reel.

When $\Delta\varepsilon_L$ drops to 1.0%, Lüders banding still takes place resulting again in organized clusters. However, as illustrated in the corresponding configuration in Fig. 5.11 and in the strain profiles in Fig. 5.12, the final result is a much more uniform deformation in the reeled section. A more detailed view of the ensuing events for this case is shown in Fig. 5.13 that shows expanded a set of configurations that show a section of pipe located between $9 < s/D < 13$ at different stages of reel rotation. This section contains the transition between reeled and unreeled pipe. In image ①, a length of $10.15D$ is in contact with the reel and is represented here by the section on the RHS whose upper and lower parts are plasticized to a strain approaching 2%. A pair of bands is just starting to emerge next to the plastically deformed section. The reel rotates and in images ② and ③ the number of bands increases and become more intense. In images ④ and ⑤ the section with the cluster of bands is getting closer to contact with the reel and now bands are starting to cover the relatively undeformed section ahead of the initial cluster. In image ⑥, the bands although still distinct have joined the rest of the plasticized zone. Since the Lüders induced strain is significantly smaller than the bending strain imposed by the reel, the local strain must increase as the section comes into contact with the reel. The additional deformation takes the material into the hardening regime and is consequently homogeneous. Thus in image ⑦, this additional deformation overwhelms the banding and, at least on the top and bottom, deformation appears continuous. This is reflected in the nearly uniform strain at both the top and bottom seen in the corresponding profiles in Fig. 5.12.

In the two cases with Lüders strain higher than 2.5%, the deformation in the bands increases and the clusters become further separated by sections of very low strain. The local strains in the bottom bands increase also and group themselves into more distinct clusters.

The main effect of the level of Lüders strain on the ovalization induced by reeling is that as it increases the cross section experiences larger amplitude undulations as shown in the change in diameter axial profiles in Fig. 5.14. At the same time the average value is not altered significantly.

In summary, as the Lüders strain increases, the local strain in the induced bands increases both at the top and bottom. The amplitude of the strain undulations increases and the clusters are separated by increasingly longer sections of relatively undeformed material. The periodicity of the clusters, as measured by the distance between the maximum strain recorded in each, goes from 1.14D for Lüders strain of 1.5%, to 1.54D for 2.5% and 1.80D for 3.5%.

5.3.2 Effect of Tension

The application of a small amount of back tension during a reeling operation has a stabilizing effect on the structure (e.g., see Liu and Kyriakides [2014]). It is thus worth examining the effect of the level of tension on a reeled pipe that exhibits Lüders bands. This will be examined through reeling simulations that involve the pipe and reel geometry of the base case listed in Table 5.1 with an X-65 material with $\Delta\varepsilon_L = 2.5\%$. The tension level is varied between $0.01\,T_o$ and $0.10\,T_o$ and the results are summarized in Figs. 5.15-17. Figure 5.15 shows the deformed configurations of five models wound to the same angle on the reel, 40.1°, at different values of tension. Superimposed are again contours of equivalent plastic strain. Figure 5.16 shows plots of plastic strain profiles along the top (T) and bottom (B) generators for three of the five tension levels. The first observation is that increasing the tension increases the length of pipe that is in contact with the reel for the same reel rotation. Thus for tension of $0.01T_o$ the contact length is 12.55D, for $0.05T_o$ it is 13.98D and for $0.1T_o$ is 14.55D. The Lüders banding at the

top is seen to be similar in intensity with the width of the clusters increasing somewhat with tension. The bands at the bottom appear somewhat less intense and of smaller amplitude as the tension increases while the clustering becomes more intense and more similar to the ones at the top. As expected, reeling under tension increases the ovalization of the pipe cross section. This effect is quantified in the plot of $\Delta D / D$ vs. length in Fig. 5.17 where the average ovalization is seen to increase from about 2% at $0.01T_o$ to 2.75% at $0.1T_o$. The results also show that the amplitude of the undulations in ovalization not to change significantly with tension.

5.3.3 Effect of Reel Curvature

We next examine the effect of the curvature of the reel on the Lüders induced banded deformation. To this end the 12-inch pipe listed in Table 5.1 is wound onto reels with radii (R_r) of 400, 350, 300 and 250 in (10.16, 8.89, 7.62, 6.35 m). These combinations of pipe diameter and reel radius induce bending strains of 1.57%, 1.79%, 2.08% and 2.49% respectively. The material is the same X-65 steel listed in Table 5.1 with $\Delta\varepsilon_L = 2.5\%$ and the tension level is $0.05T_o$. Figure 5.18 shows deformed configurations for each of the four cases with superimposed color contours of the intensity of plastic deformation. In each case the reel was rotated to the same degree bringing a length of $\phi R_r = 16.47D$ into contact. Figure 5.19 shows plots of the plastic strain profiles at the top and bottom generators for three of the cases. The amplitude of the strains in the bands is governed by the Lüders strain, which is constant, so it remains unchanged. However, the spacing of the clusters changes with R_r going from $1.71D$ for the 400 in reel to $1.47D$ for the 250 in one. The reel-induced average bending strain decreases as the reel radius increases and, since the Lüders strain is the same, the spacing must increase. Some difference can be seen in the bands at the bottom; whereas for the

250 in reel radius the banding is nearly continuous, for the larger R_r the bands are organized into clusters that are separated by zones of small strain. In all cases both the strains at the top and bottom generators average out to the reel induced strains listed above.

Figure 5.20 shows plots of the pipe ovalization induced by reeling for the four reel radii considered. As expected, decreasing the reel radius takes the pipe further into the plastic strain, resulting in larger change in diameter in the plane of bending and larger ovalization. Thus for reel radius of 400 in the average ovalization is approximately 1.5% whereas for 250 in it increases to about 3.2%. The undulations in the ovality also are affected so that for the larger R_r each period has two undulations whereas for the smallest radius just one.

5.3.4 Effect of Pipe D/t

We next examine the effect of changing the pipe D/t on the induced Lüders deformations. The pipe and reel diameters are kept the same as in the base case but the thickness is changed so that the pipes have D/ts of 20 and 18 (see Table 5.1); these are values commonly used in offshore reeling installation operations. The material is modeled with the same X-65 non-monotonic stress strain response with $\Delta\varepsilon_L = 2.5\%$ and the tension is $0.05T_o$. Figure 5.21 compares deformed configurations for three D/t values. Since the pipe and reel diameters are the same, the induced bending strain for the three pipes is at the same level of 2.08%. The three cases were wound to the same reel angle ($\phi = 40.1^o$), however, a small decrease in the length that comes into contact with the reel is observed as the D/t decreases due to the increased bending stiffness of the pipe. The number of elements through the thickness of the models remains at two with the mesh on the surface of the pipe staying the same for the three cases. Thus, as the

thickness increases the aspect ratio of the elements increasingly deviates from its nearly isotropic nature for D/t = 24. At the top, the induced bands appear similar and are organized into similar clusters. This is also reflected in the strain profiles along the top generators plotted in Fig. 5.22. A small reduction in the extent of the top bands with D/t may be related to the differences in the meshes. The bottom bands appear stronger and more continuous for the higher D/t and the same trend is reflected in the strain profiles. The amplitudes of the strains at the top generator are nearly the same but the spacing of the clusters decreases from 1.55D for D/t of 24 to 1.44D for 18.

Figure 5.23 shows plots of the ovalization induced to each pipe by reeling. Increasing the pipe wall thickness reduces the change in diameter in the plane of bending and the ovalization. Thus, the change in diameter which is at a level of about 2.5% for D/t = 24 reduces to about 1.5% for D/t = 18. The amplitude of the ovality undulations is about the same but their period is reduced slightly as the D/t decreases in concert with that of the cluster of bands.

5.4 MESH SENSITIVITY

In the way of demonstrating the adequacy of the mesh adopted in the base case in Section 5.2.1 in capturing the Lüders banding induced by reeling, the simulation was repeated with a much finer mesh using a tension of $0.01T_o$. The two nearly isotropic meshes used are compared in Fig. 5.24 that shows a 30° sector of the pipe cross section with a 0.5D length. In Fig. 5.24a the pipe is discretized with the two elements through the thickness and in Fig. 5.24b with four. Thus the finer mesh consists of 8 times more elements. The simulation and its main results are essentially identical for the two meshes. We have thus chosen to compare the detailed deformation in the cluster of bands at approximately s = 2D. Expanded views of the affected section of deformed pipe with

color contours of equivalent plastic strain superimposed are compared in Fig. 5.25. Figure 5.26 compares the strains along the top generator from the two meshes. The main features of bands in the two meshes are essentially the same and so is the location of the clusters. The strain contours show the bands to be somewhat more intense and to extend somewhat further out for the finer mesh. The strains at the top generator are also very similar. In view of the very significant increase in computation time required by the finer mesh, the small differences in the deformation bands are deemed to be of secondary importance as they do not change the main observations and conclusions of this study.

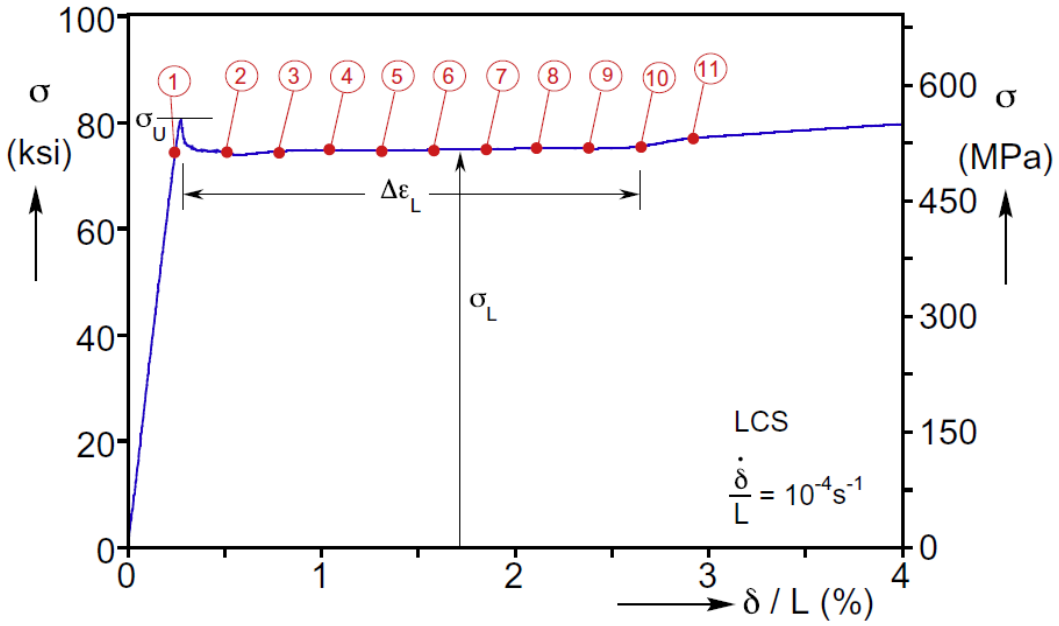

(a)

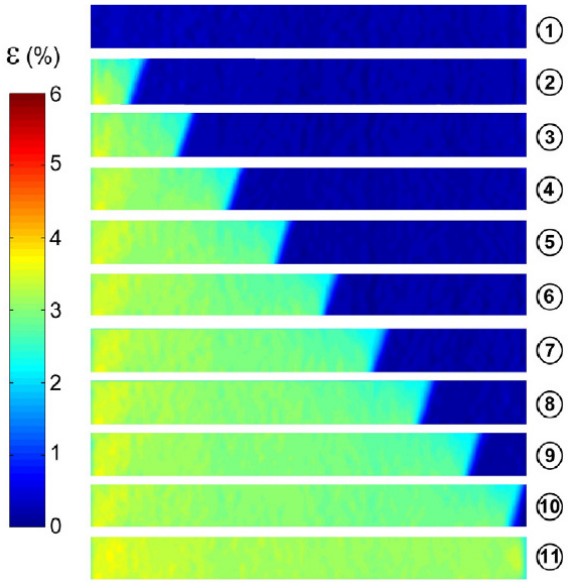

(b)

Figure 5.1 Results from a tensile test on a strip of a low-carbon steel that exhibits Lüders banding. (a) Measured stress-elongation response; (b) a set of corresponding DIC generated axial strain contours (from Hallai and Kyriakides [2013]).

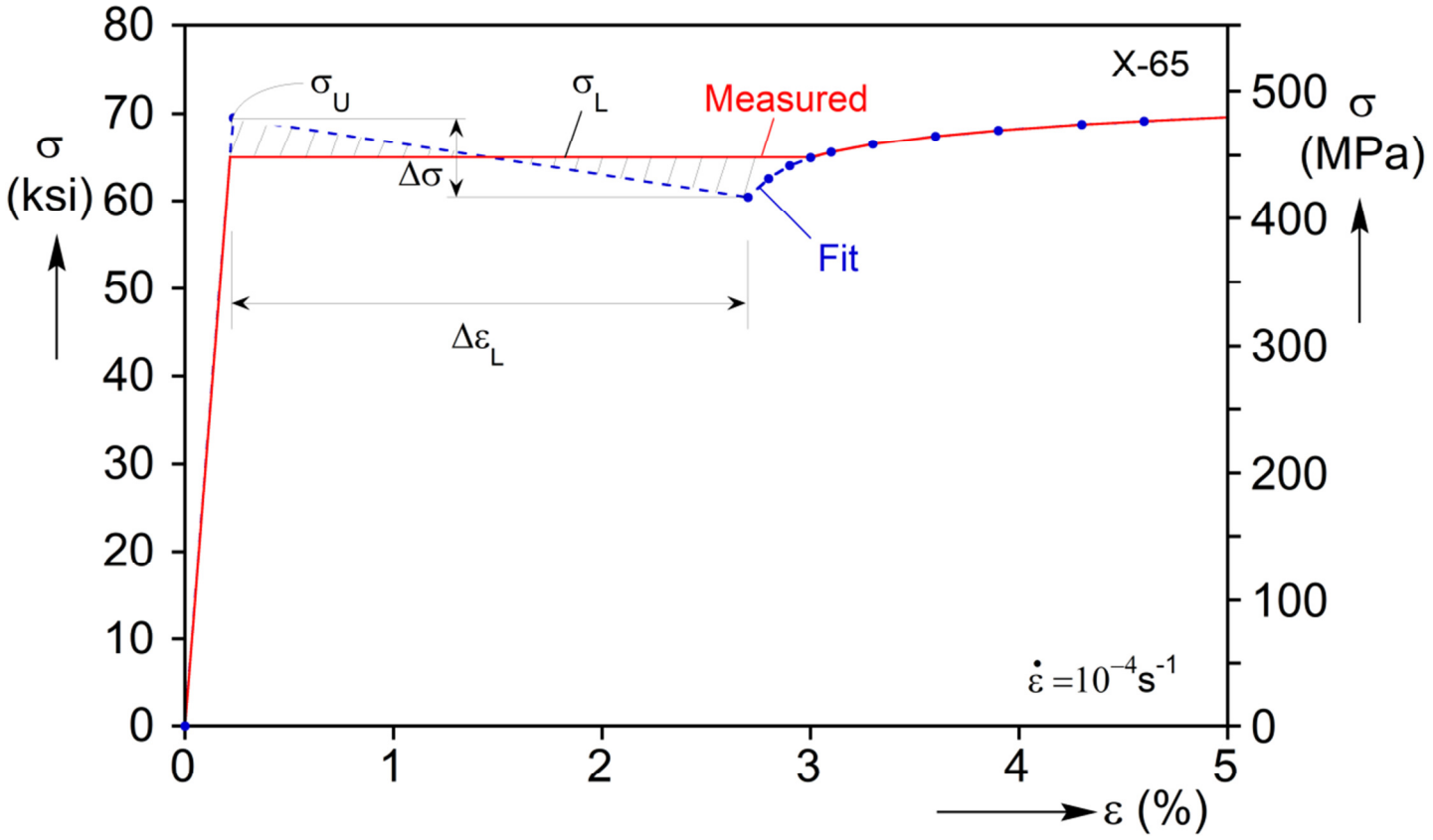

Figure 5.2 Measured material stress-elongation response and stress–strain response adopted in the simulations

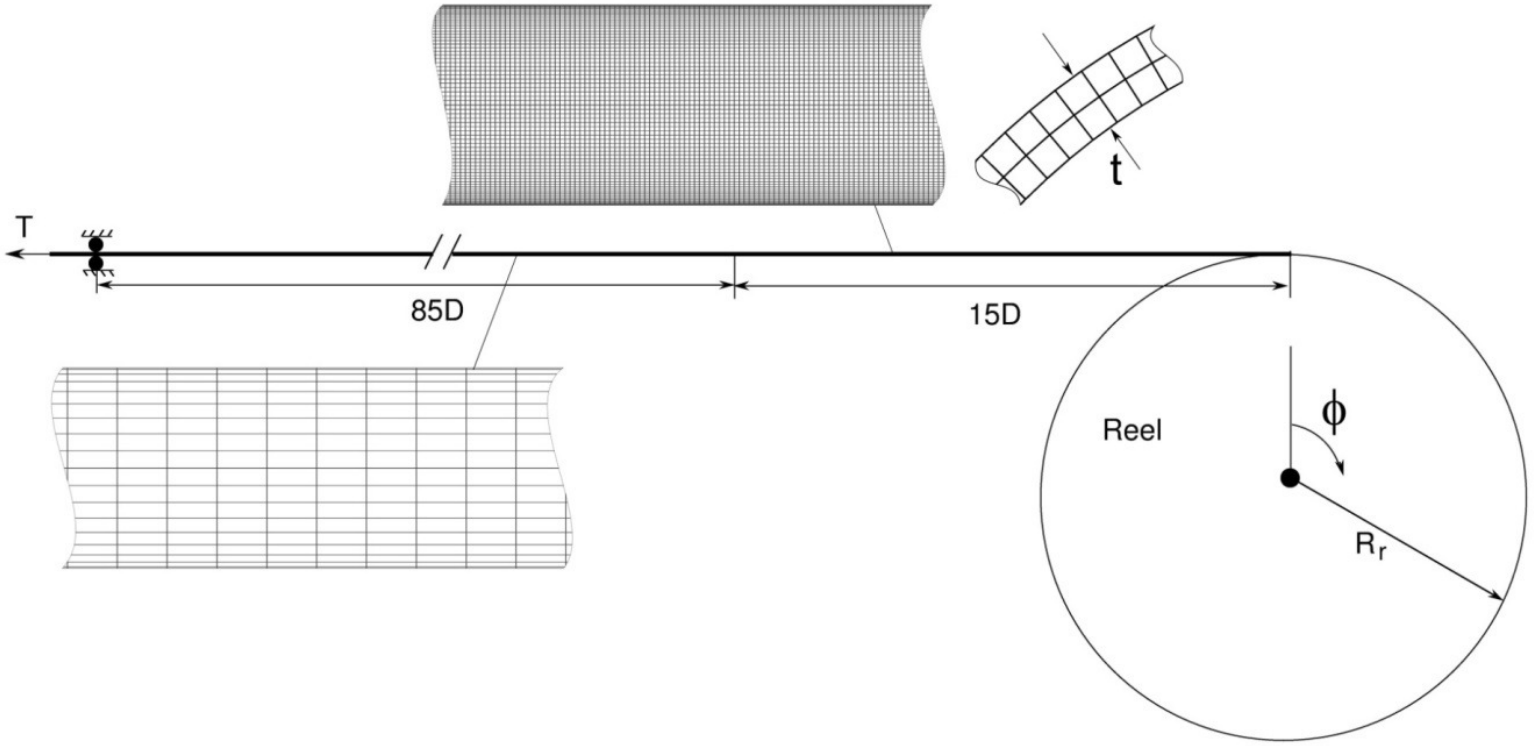

Figure 5.3 Problem geometry showing the pipe and reel in their initial positions. Shown also are the two meshes used to discretize the pipeline.

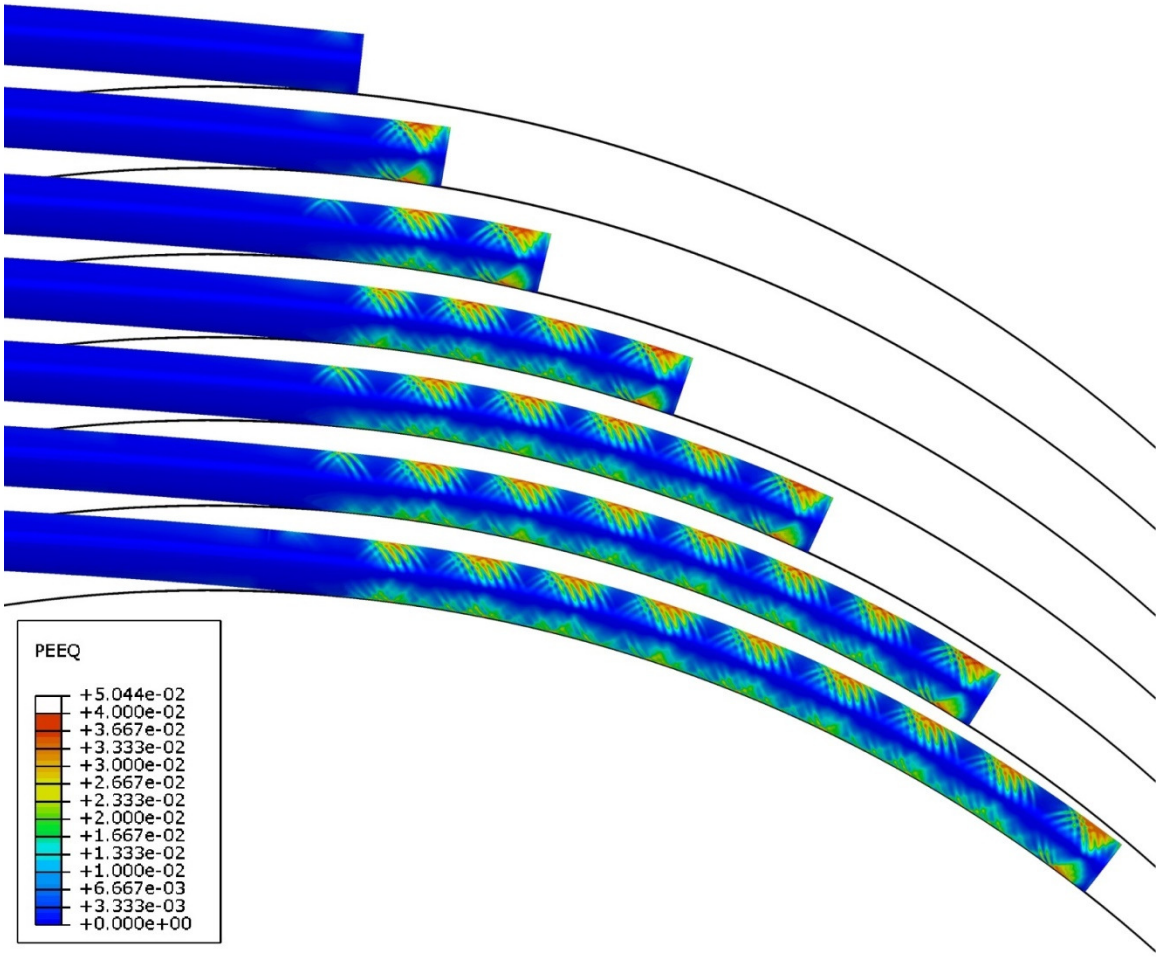

Figure 5.4 Deformed configurations of a 12-inch pipe at different stages of winding on the reel for $T = 0.05T_o$. Superimposed color contours represent the equivalent plastic strain developed in clusters of bands.

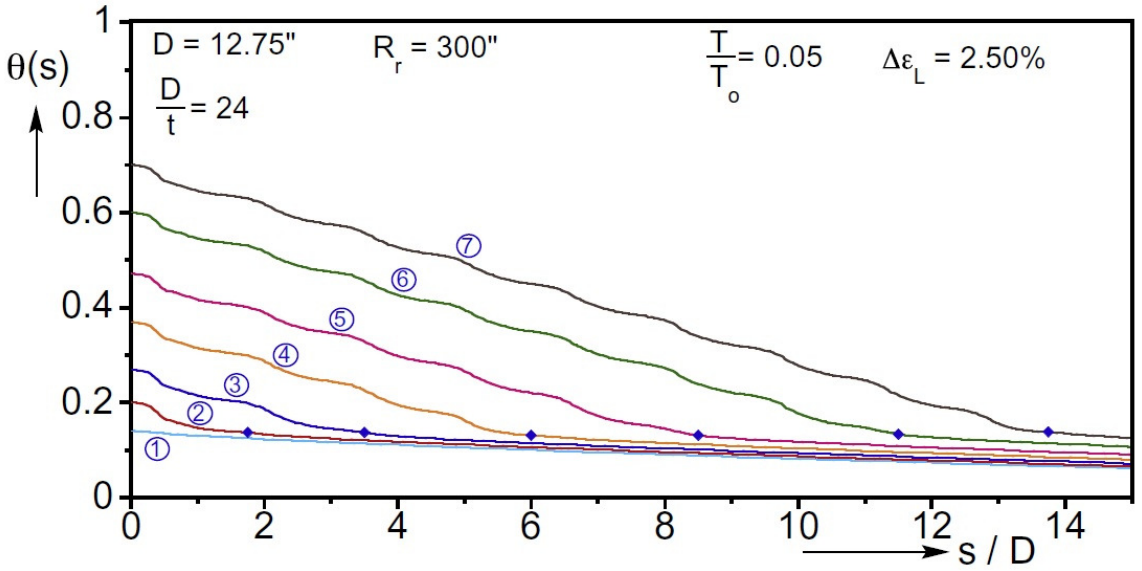

(a)

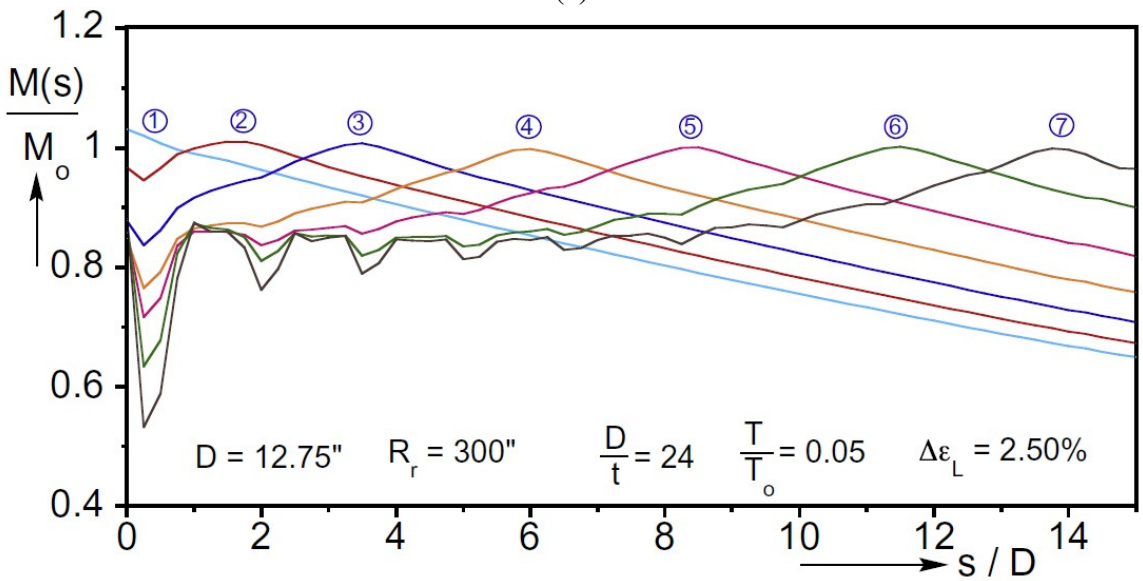

(b)

Figure 5.5 (a) Slope, $\theta(s)$, and (b) moment, $M(s)$, along the pipe length at different stages of reel rotation. Trajectories correspond to configurations in Fig. 5.4.

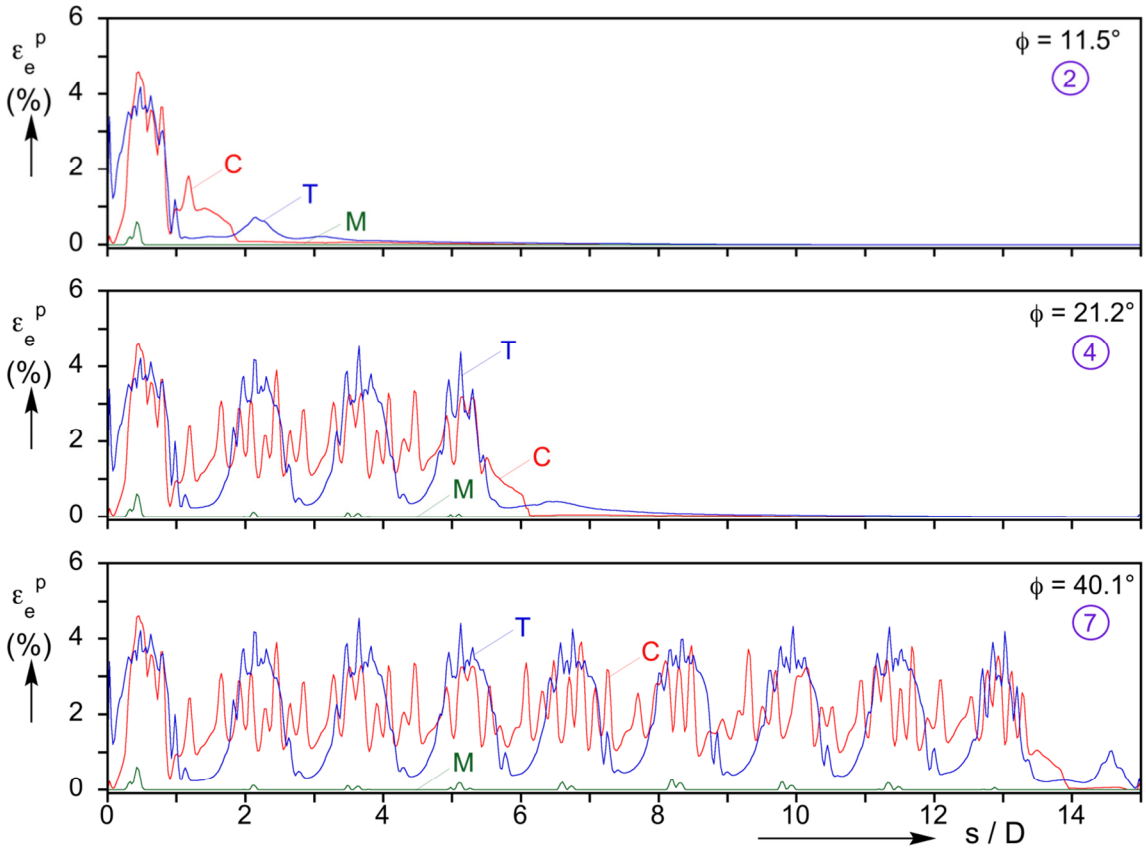

Figure 5.6 Axial strain profiles of the top and bottom generators for three of the configurations in Fig. 5.4.

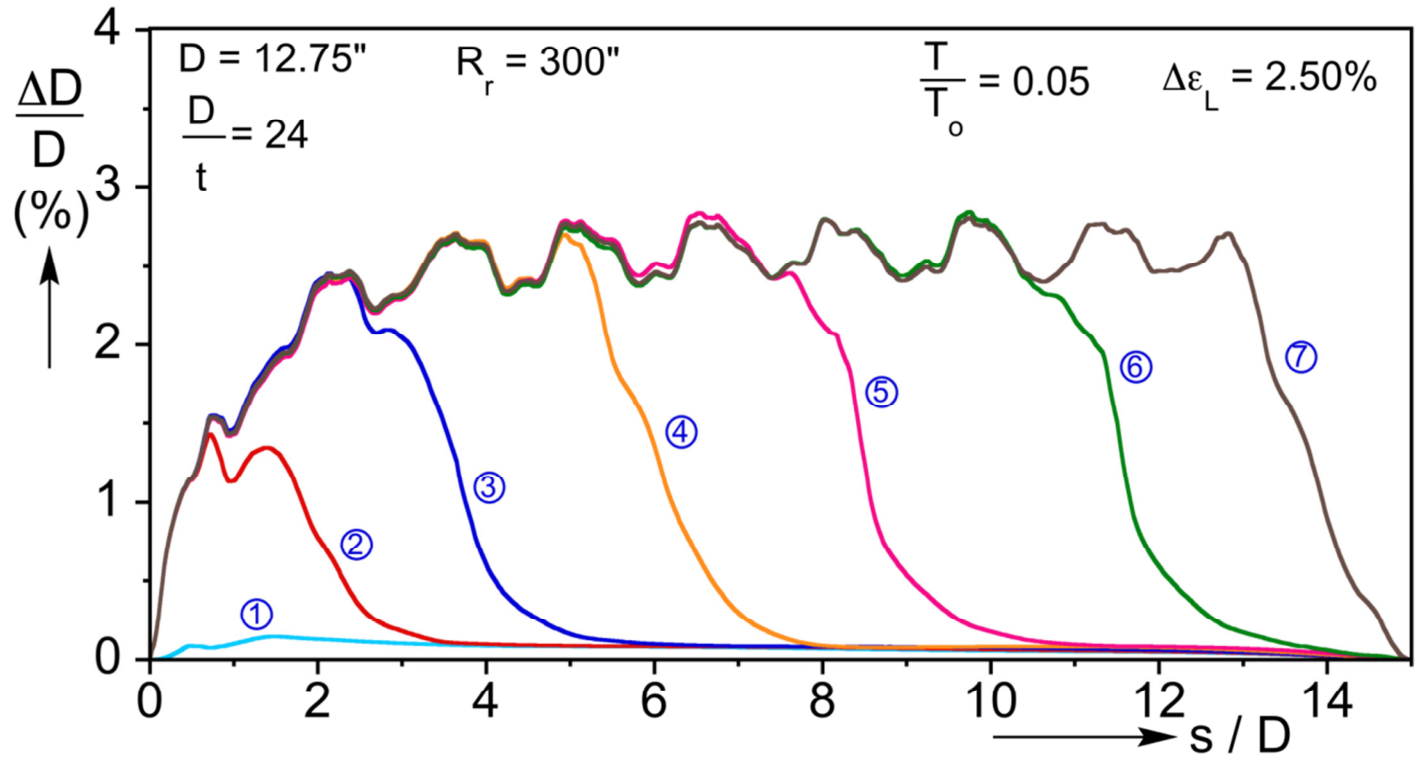

Figure 5.7 Ovalization along the pipe length at different stages of reel rotation. Trajectories correspond to configurations in Fig. 5.4.

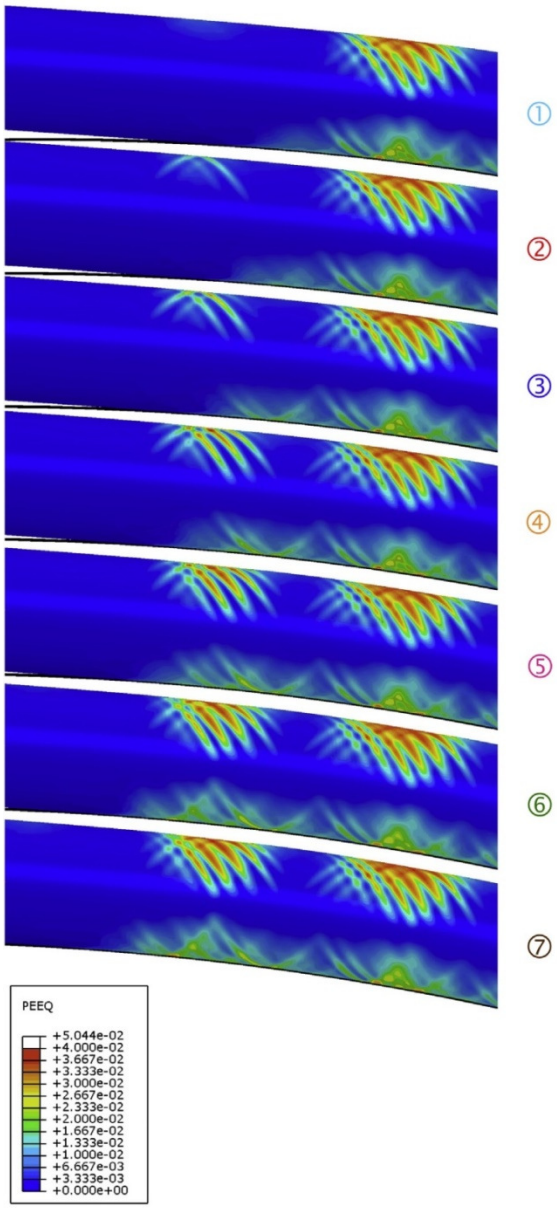

Figure 5.8 Zoomed in configurations of a section of pipe with plastic strain contours superimposed showing the development of one cluster of bands. Images correspond to reel rotations $29.5^{o} \le \phi \le 32.7^{o}$.

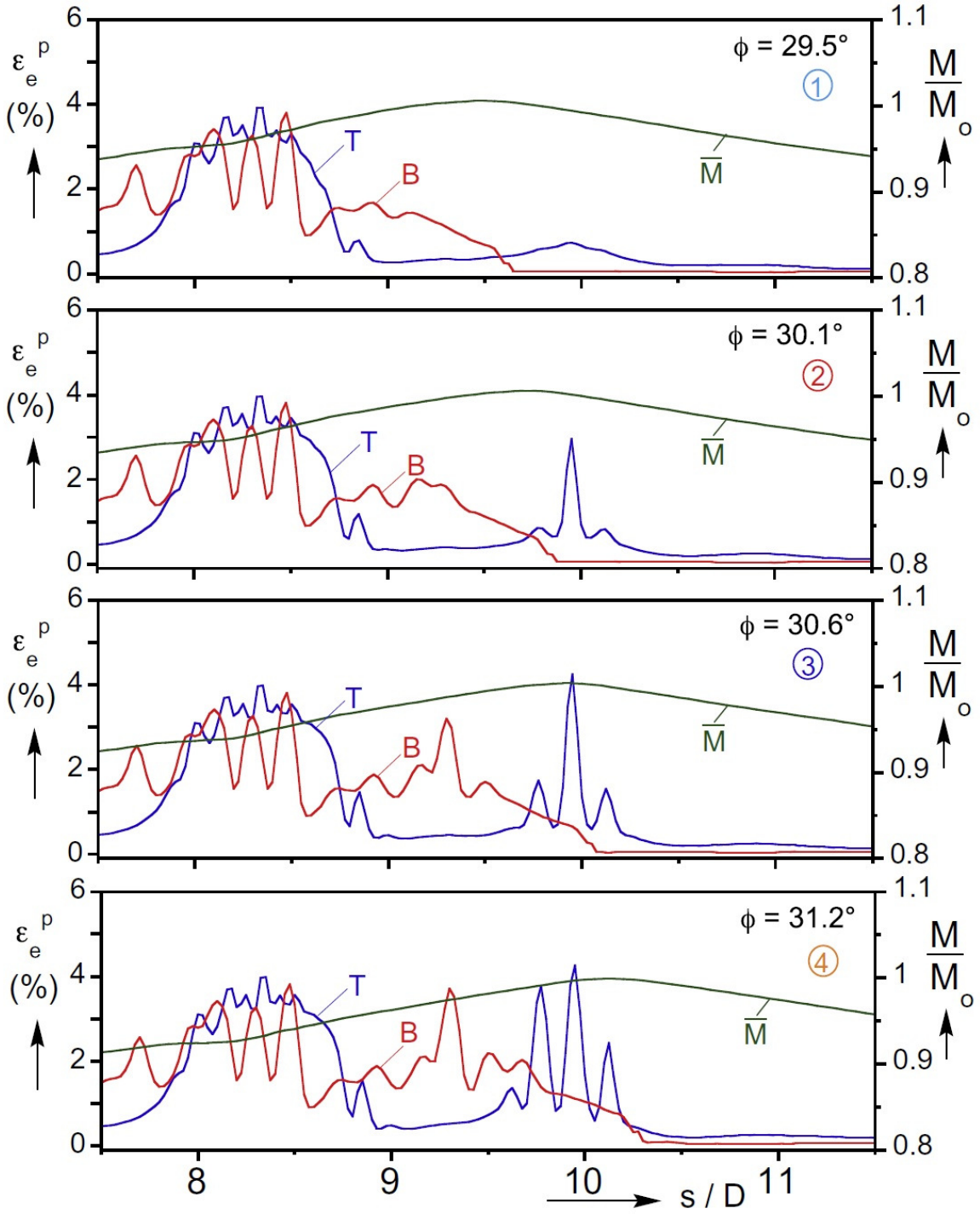

Figure 5.9 Axial strain profiles of the top and bottom generators and moment distributions for four of the configurations in Fig. 5.8.

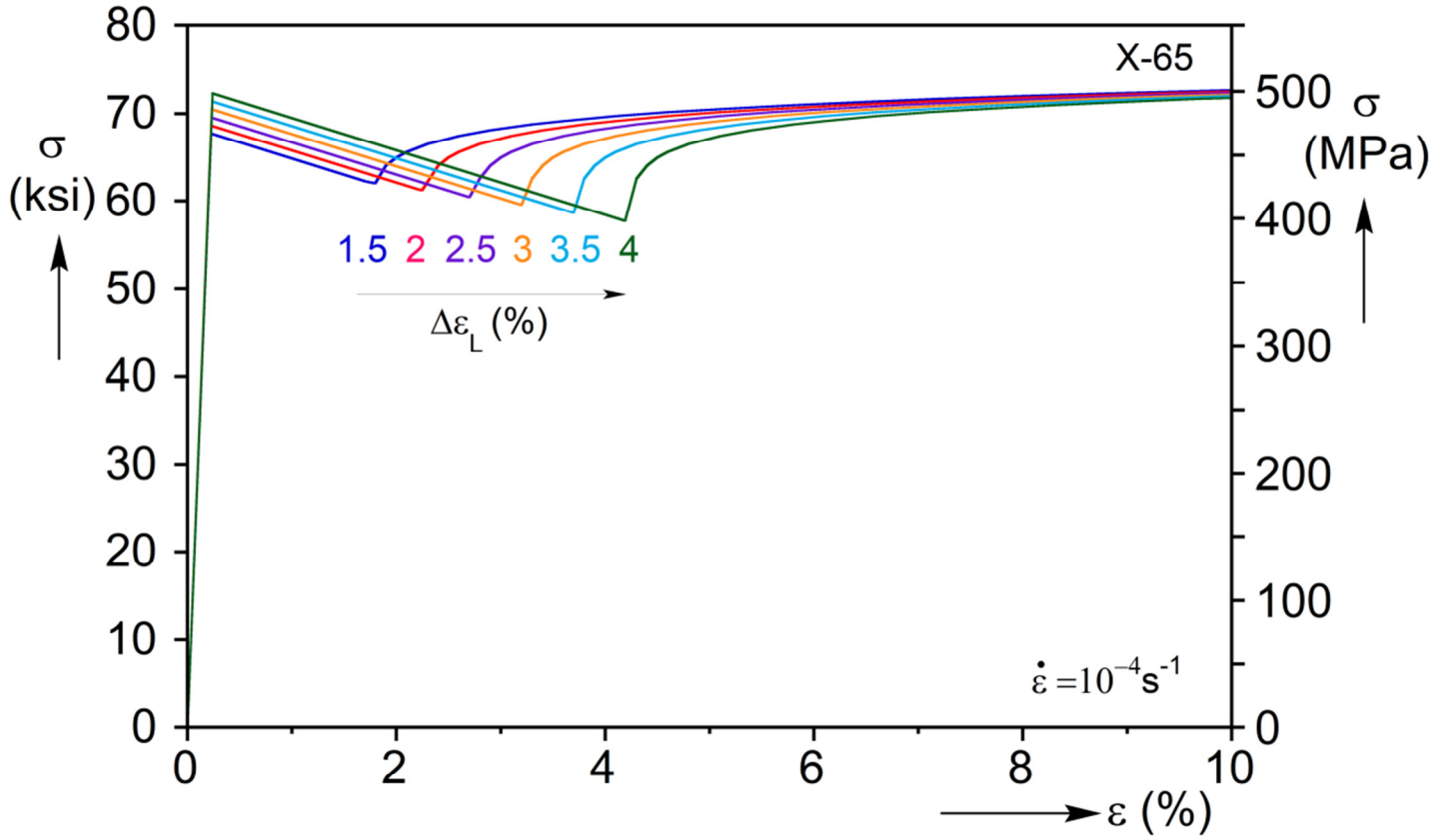

Figure 5.10 Partially unstable stress–strain responses for different values of $\Delta\varepsilon_L$.

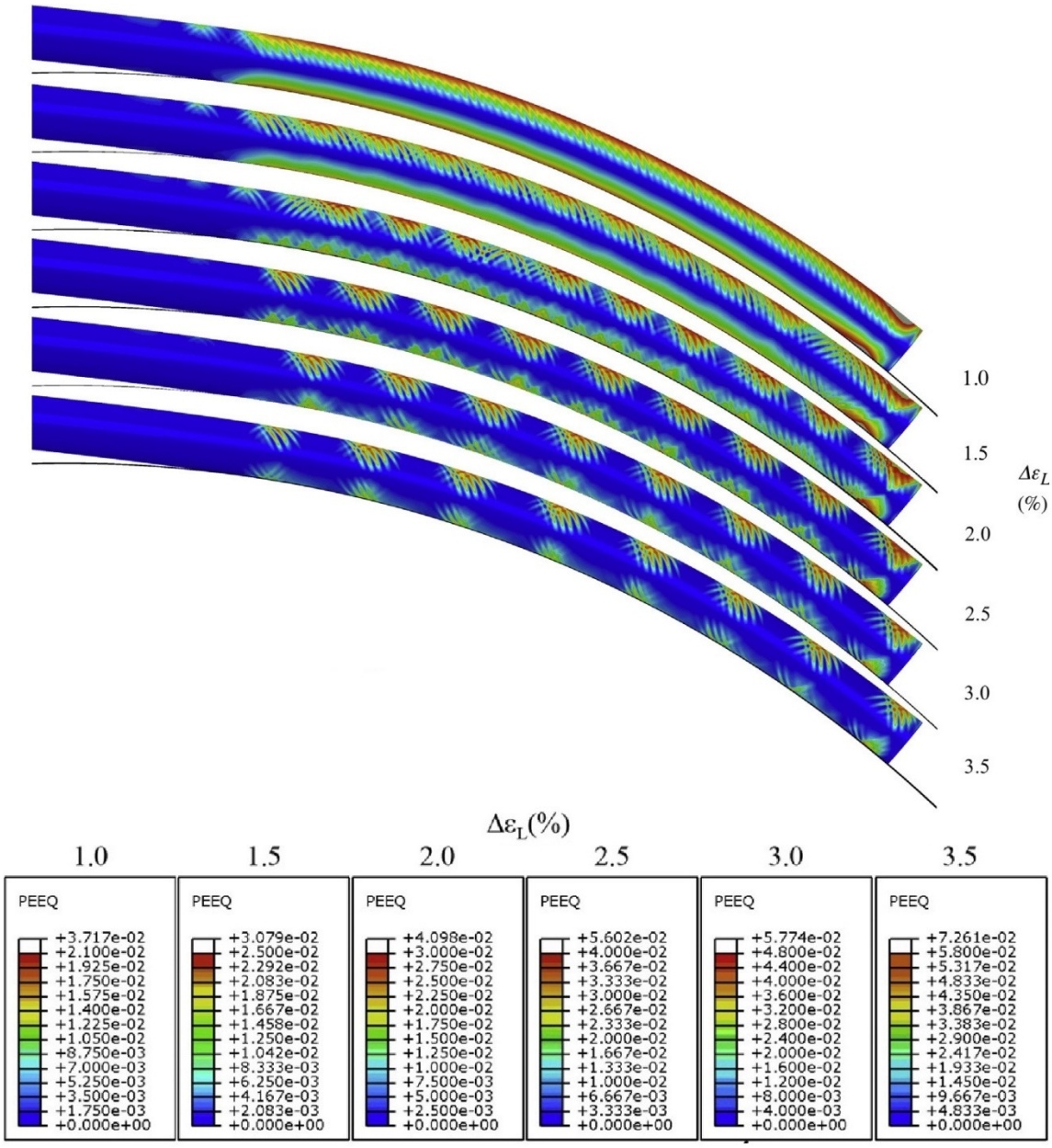

Figure 5.11 Deformed configurations of 12-inch pipe at the same reel rotation, calculated using different Lüders strains and $T = 0.05T_o$. Superimposed color contours represent the equivalent plastic strain developed.

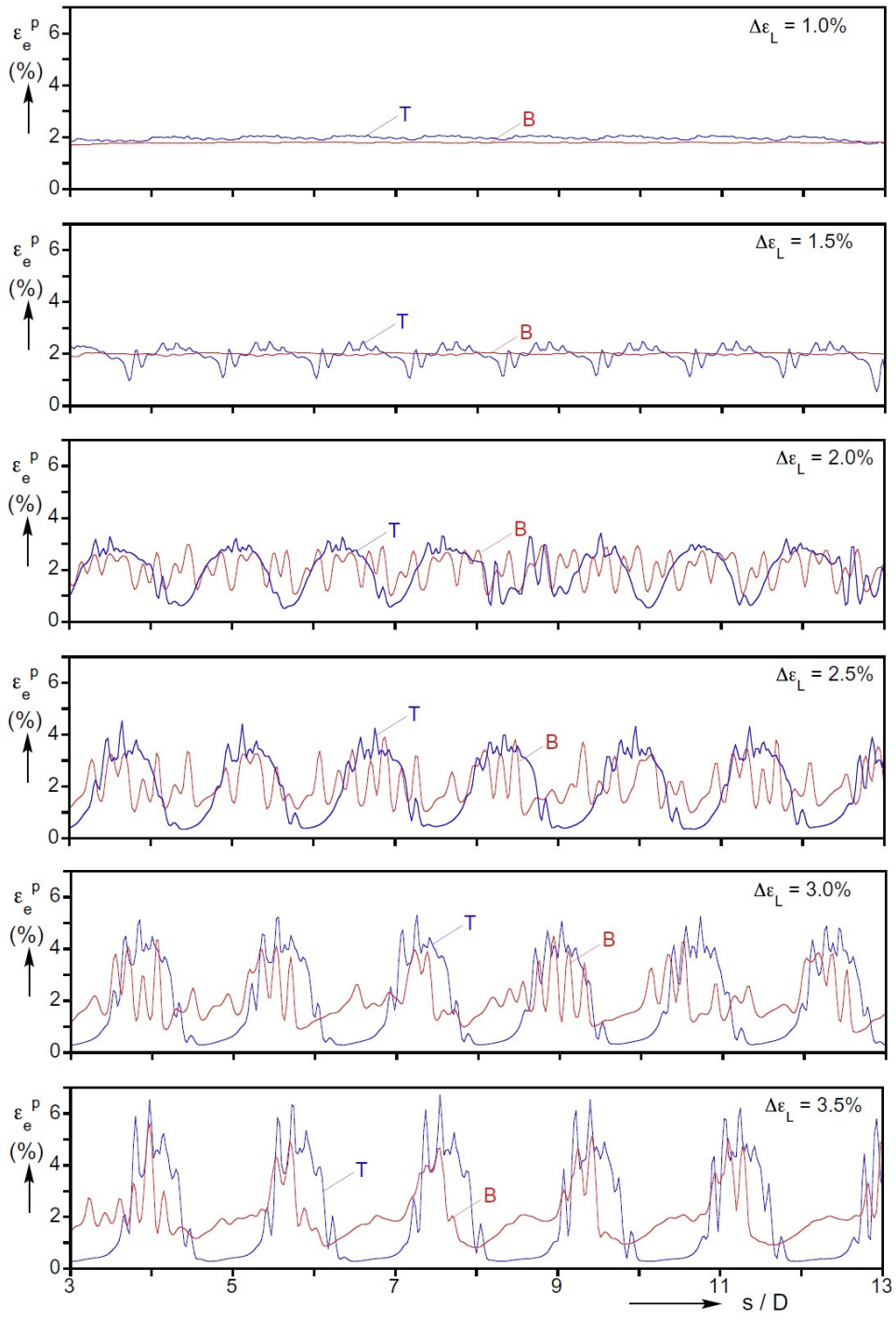

Figure 5.12 Axial strain profiles of the top and bottom generators corresponding to the different Lüders strain configurations in Fig. 5.11.

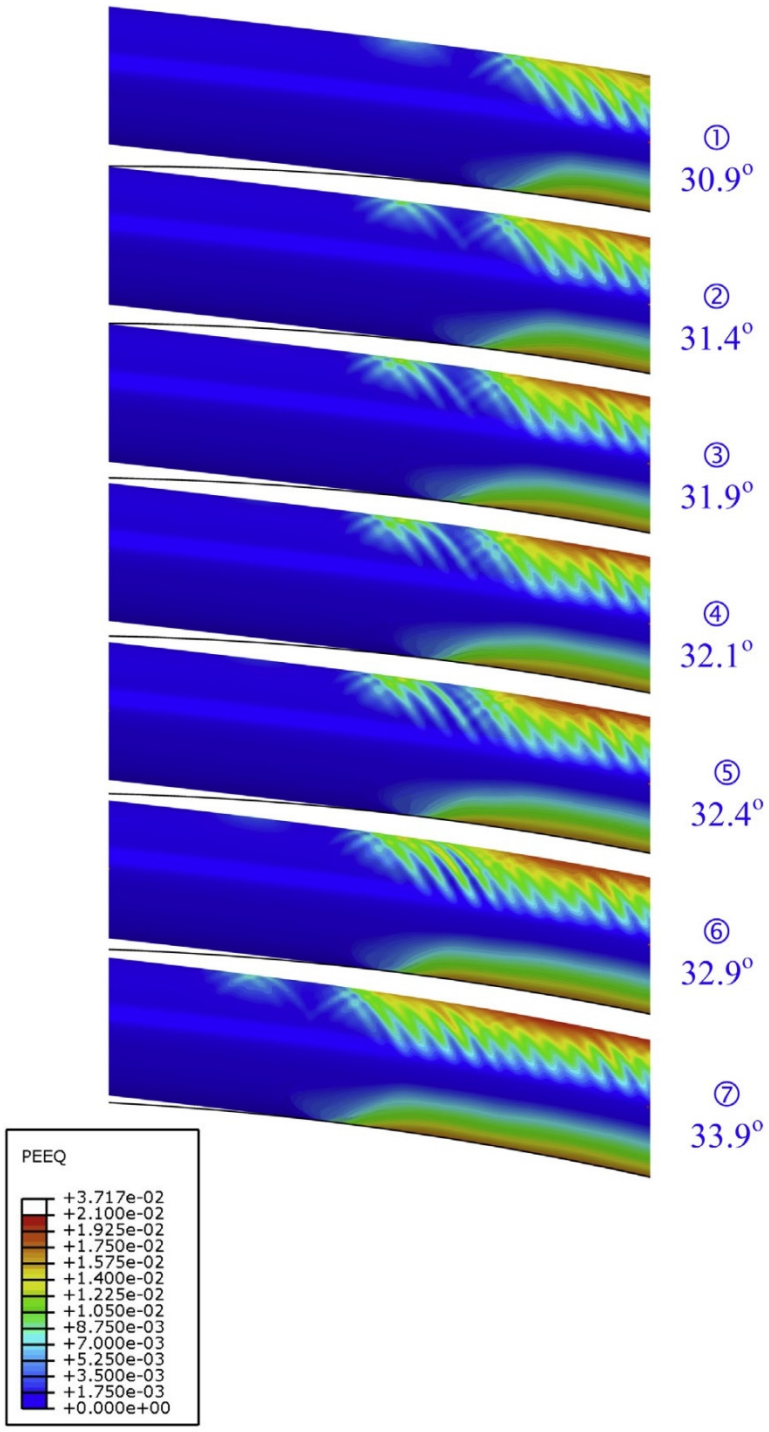

Figure 5.13 Zoomed in configurations of a section of pipe with plastic strain contours superimposed showing the development of plastic deformation for $\Delta\varepsilon_L = 1.0\%$.

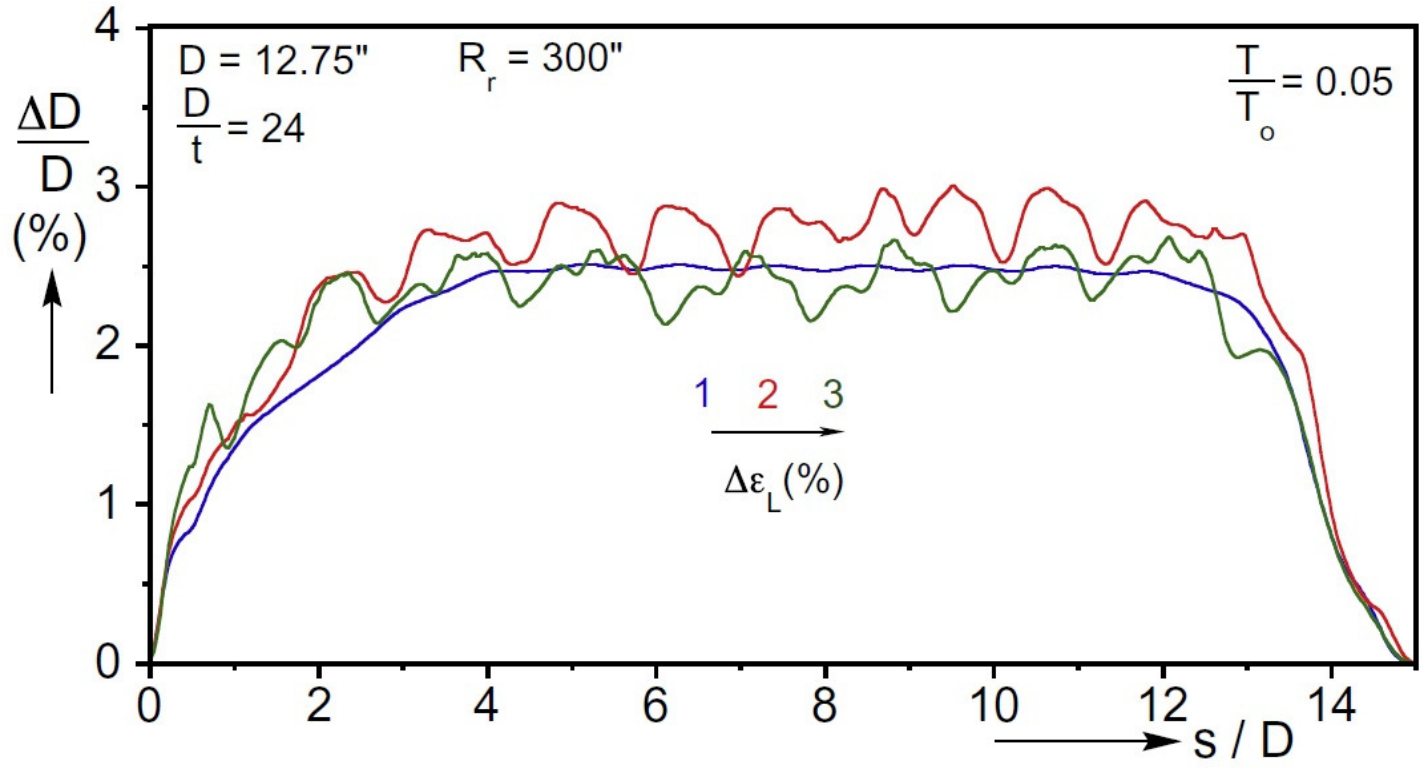

Figure 5.14 Ovalization along the pipe length of reeled pipe for three values of Lüders strain and $T = 0.05T_o$.

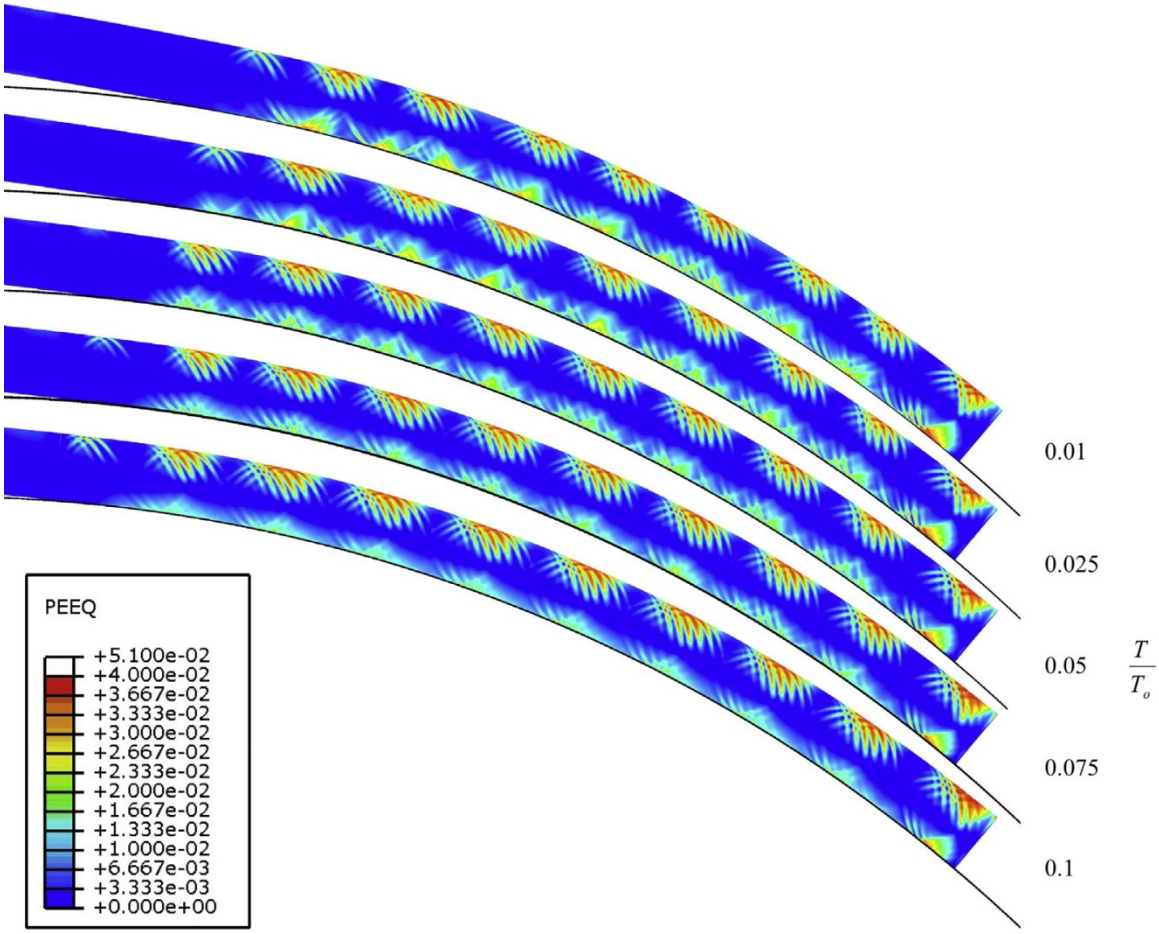

Figure 5.15 Deformed configurations of 12-inch pipe at the same reel rotation for different values of back tension ($\Delta\varepsilon_L = 2.5\%$). Superimposed color contours represent the equivalent plastic strain developed.

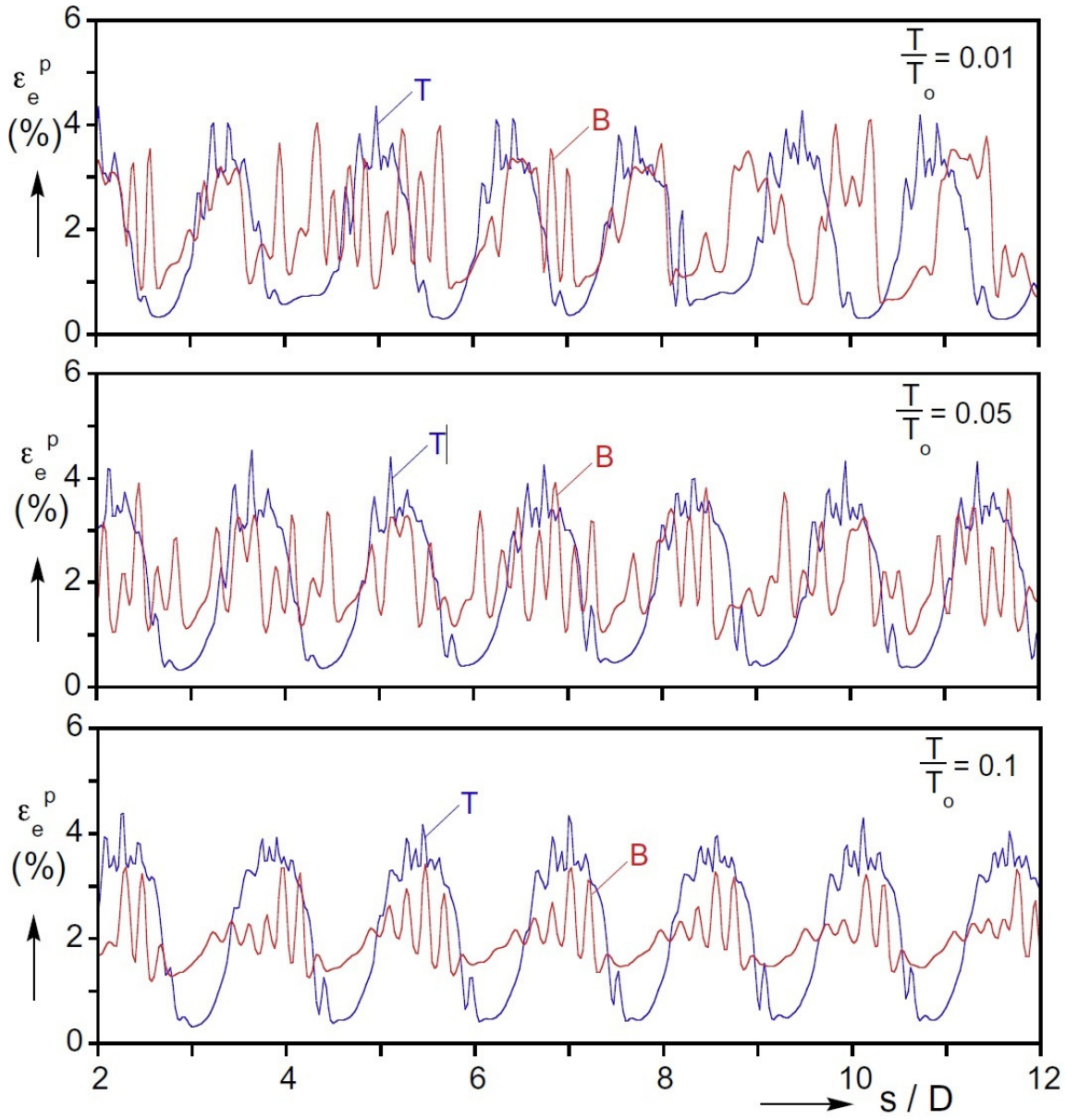

Figure 5.16 Axial strain profiles of the top and bottom generators corresponding to three of the tension level configurations in Fig. 5.15.

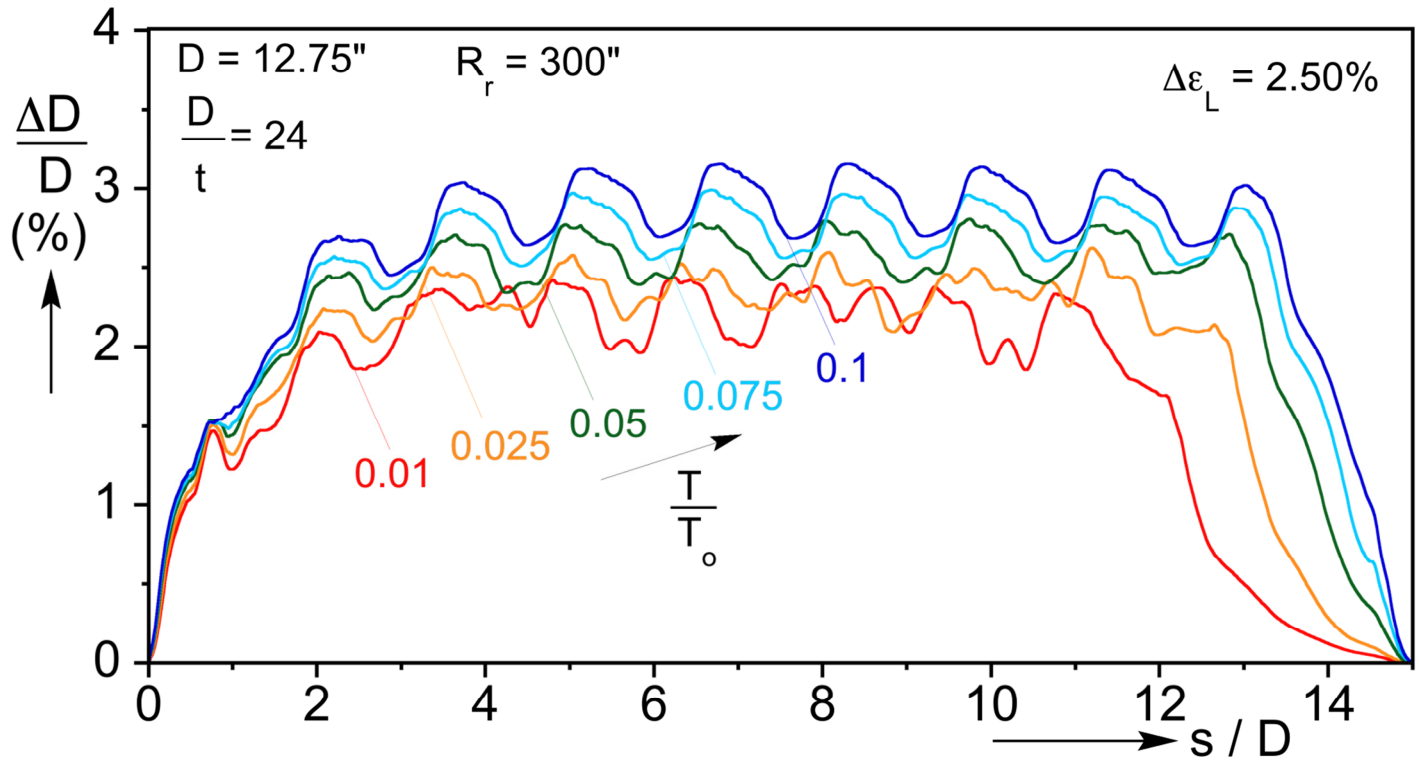

Figure 5.17 Ovalization along the length of pipe reeled at different tension levels.

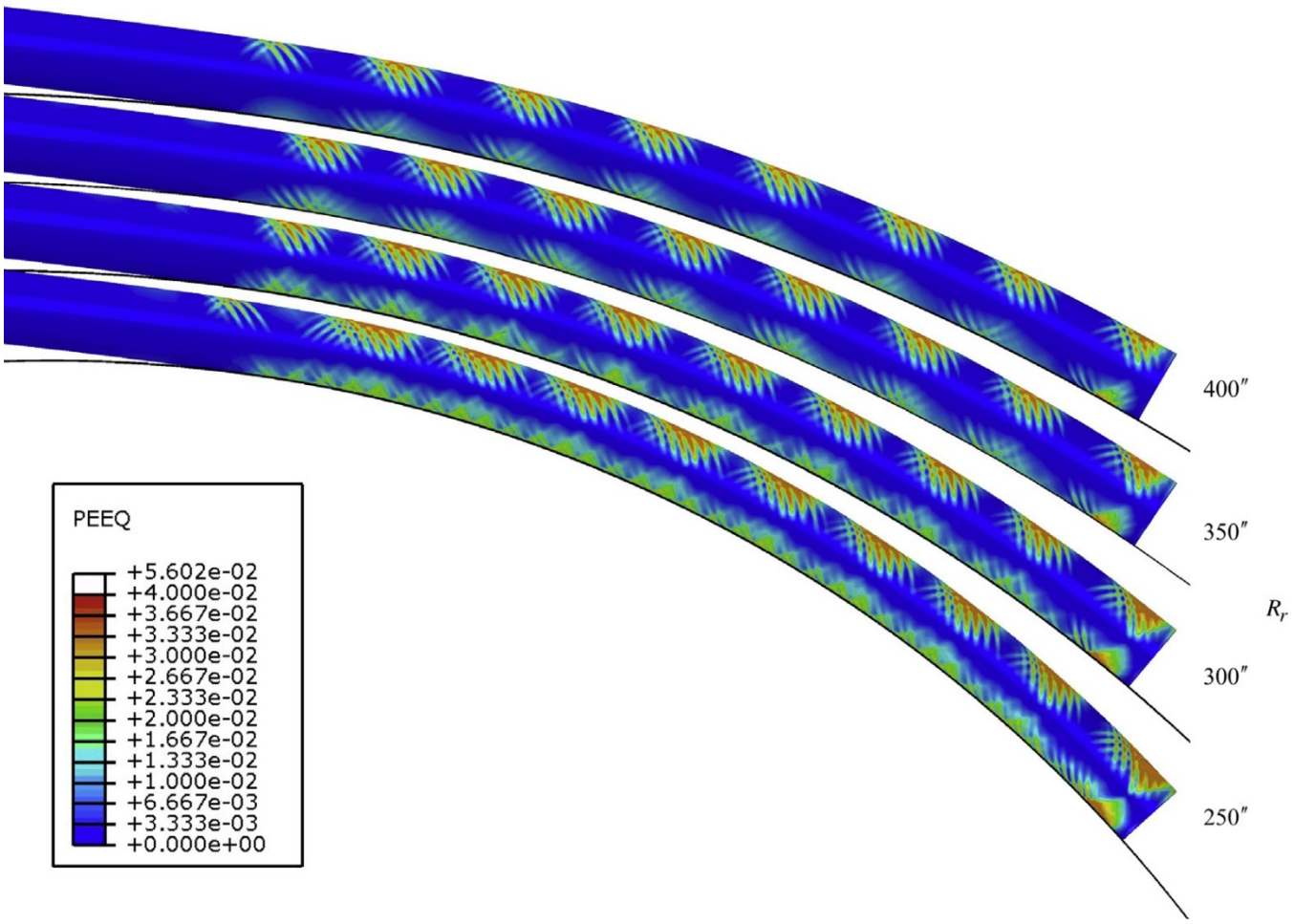

Figure 5.18 Deformed configurations of 12-inch pipe wound on reels of different radii to $\phi R_r = 16.47D$. Superimposed color contours represent the equivalent plastic strain developed.

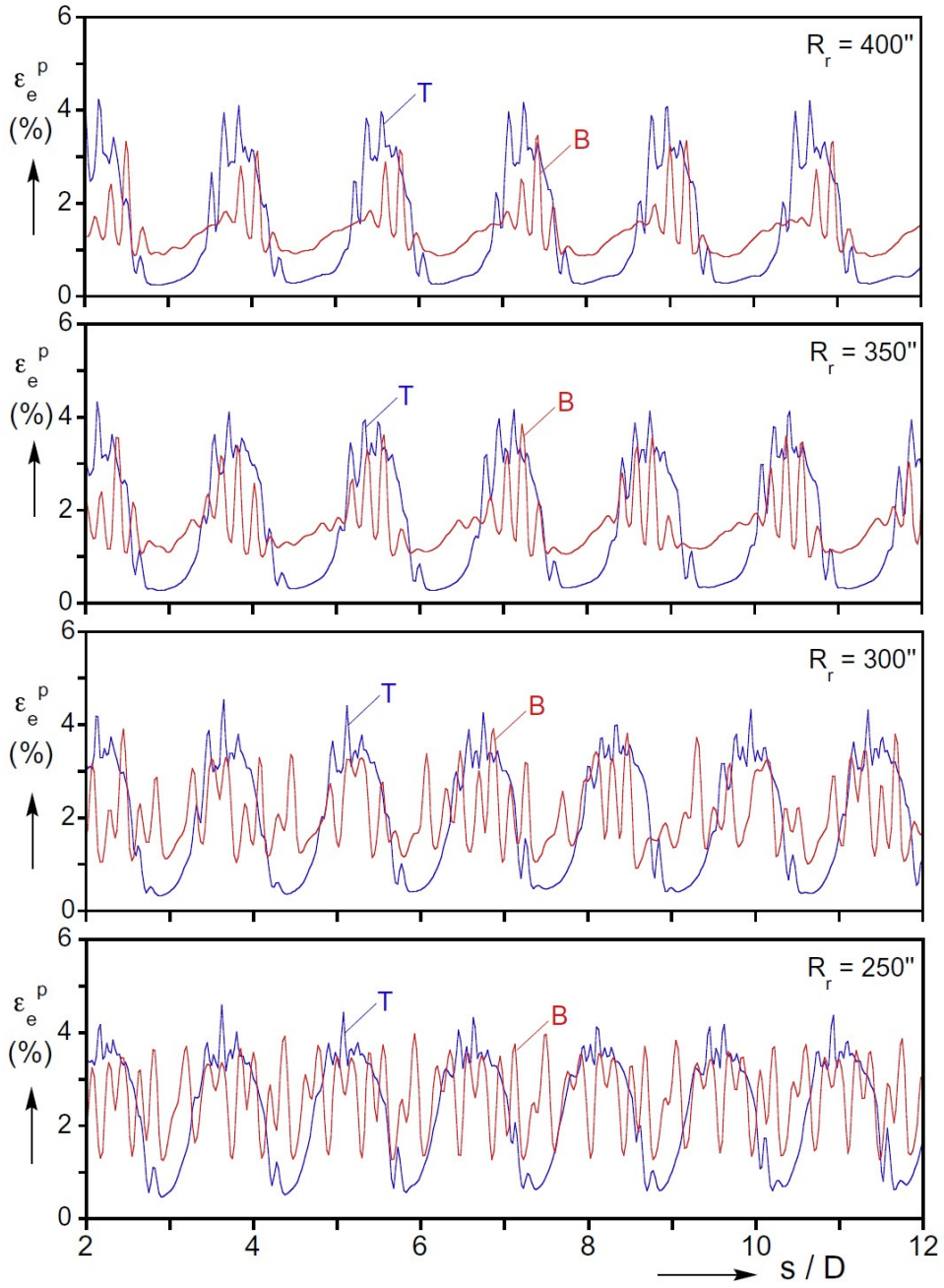

Figure 5.19 Axial strain profiles of the top and bottom generators corresponding to the configurations in Fig. 5.18 for four reel radii.

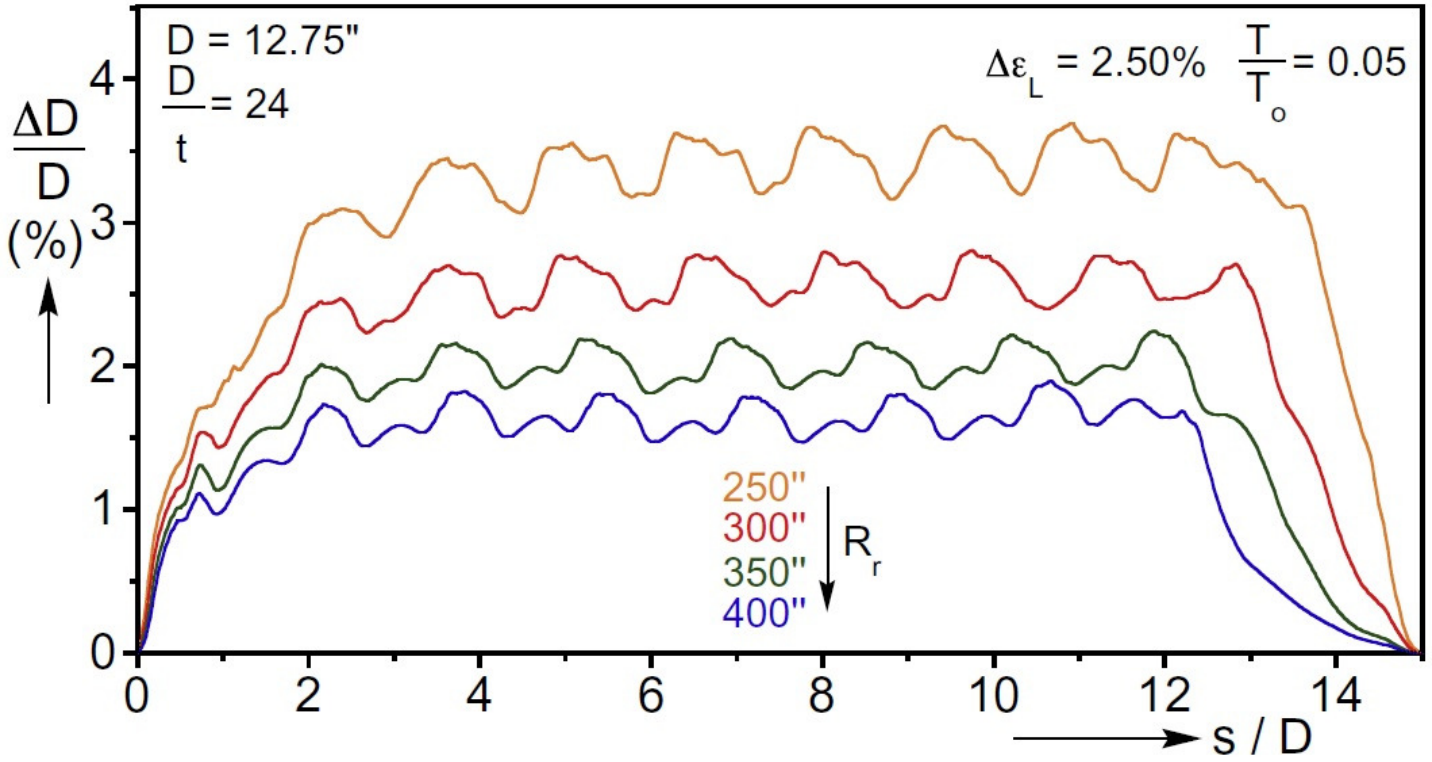

Figure 5.20 Ovalization along the length of pipe wound on reels of different radii.

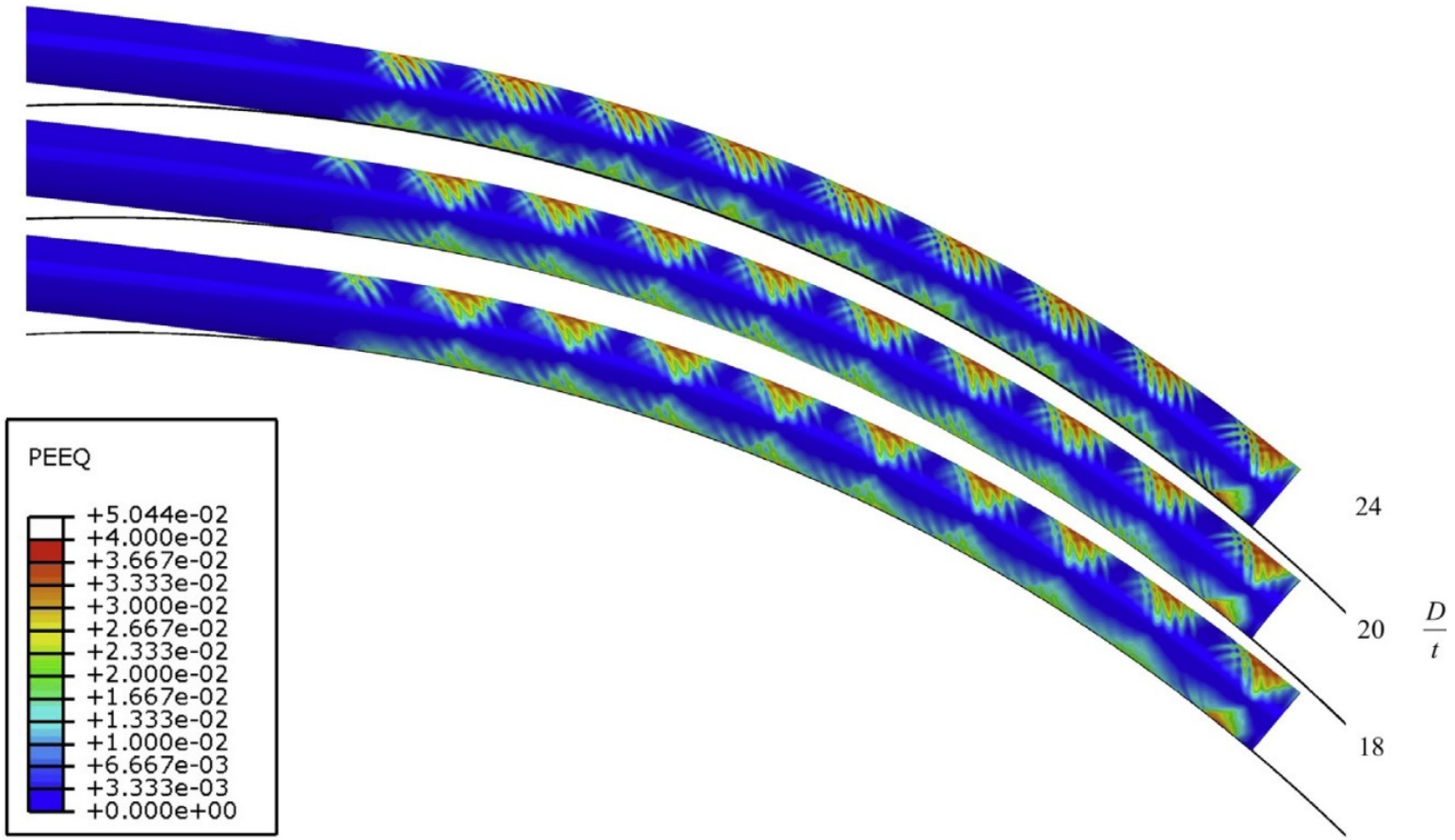

Figure 5.21 Deformed configurations of 12-inch pipe with three different D/t values at the same reel rotation. Superimposed color contours represent the equivalent plastic strain developed.

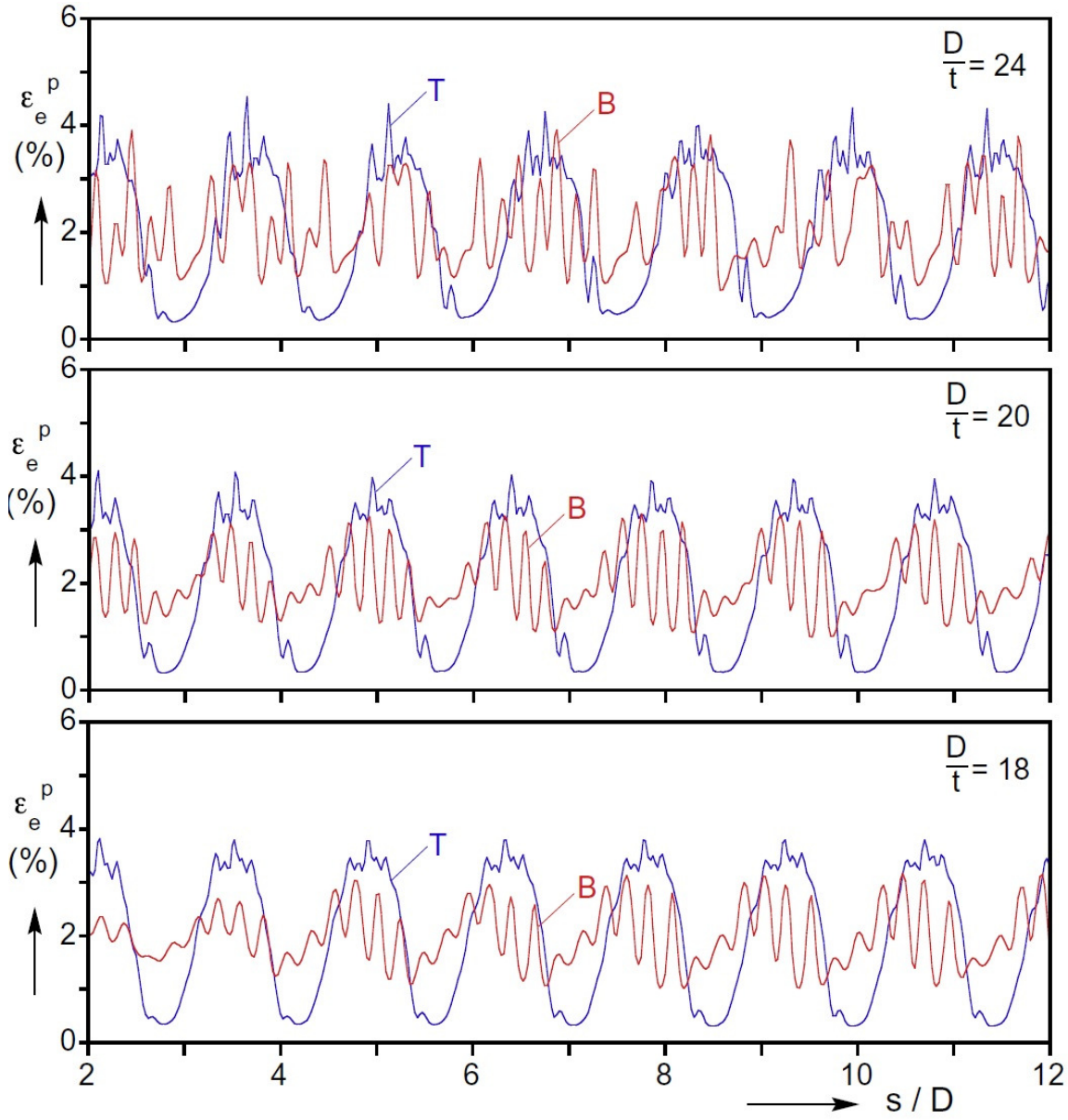

Figure 5.22 Axial strain profiles of the top and bottom generators corresponding to the configurations in Fig. 5.21 for three pipe D/ts.

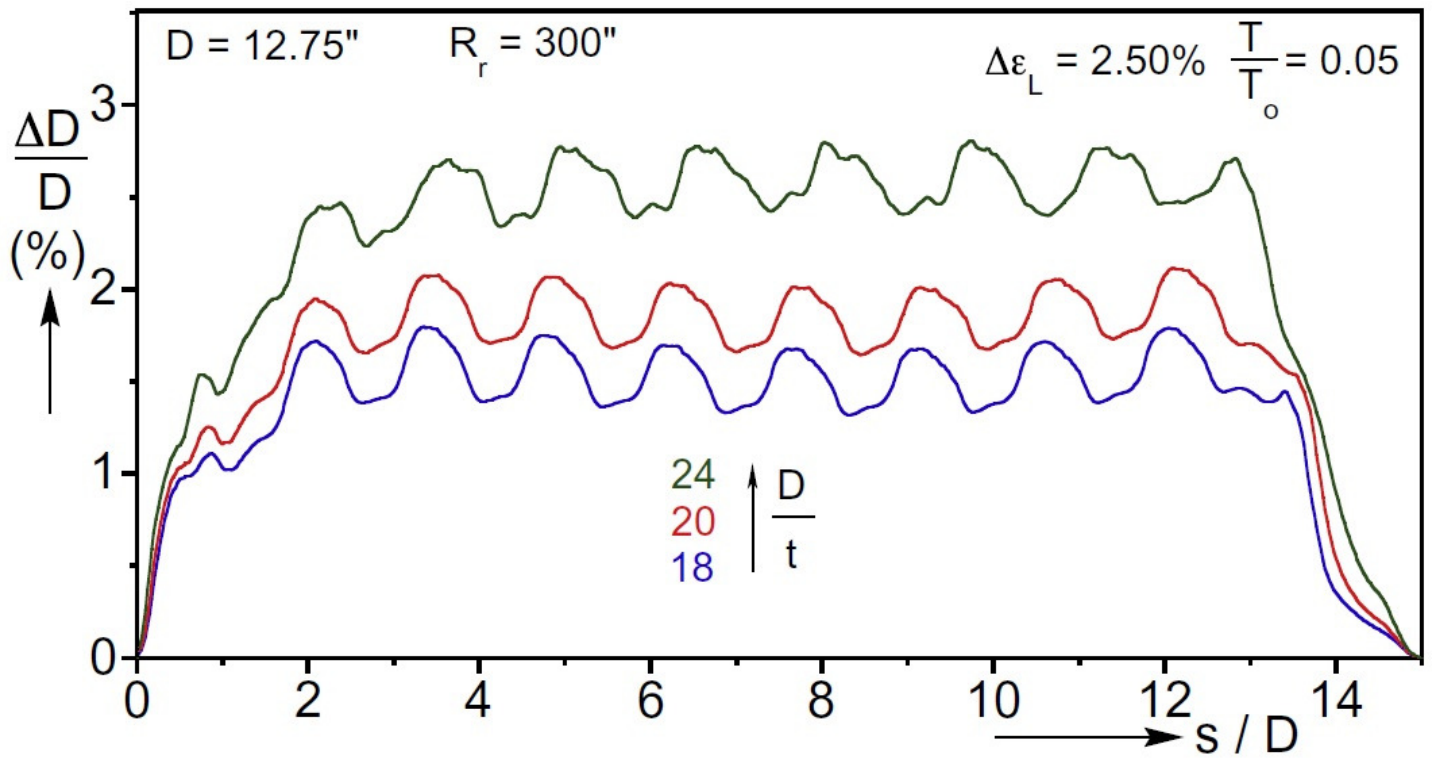

Figure 5.23 Ovalization along the length of pipes of different D/ts wound to the same reel rotation

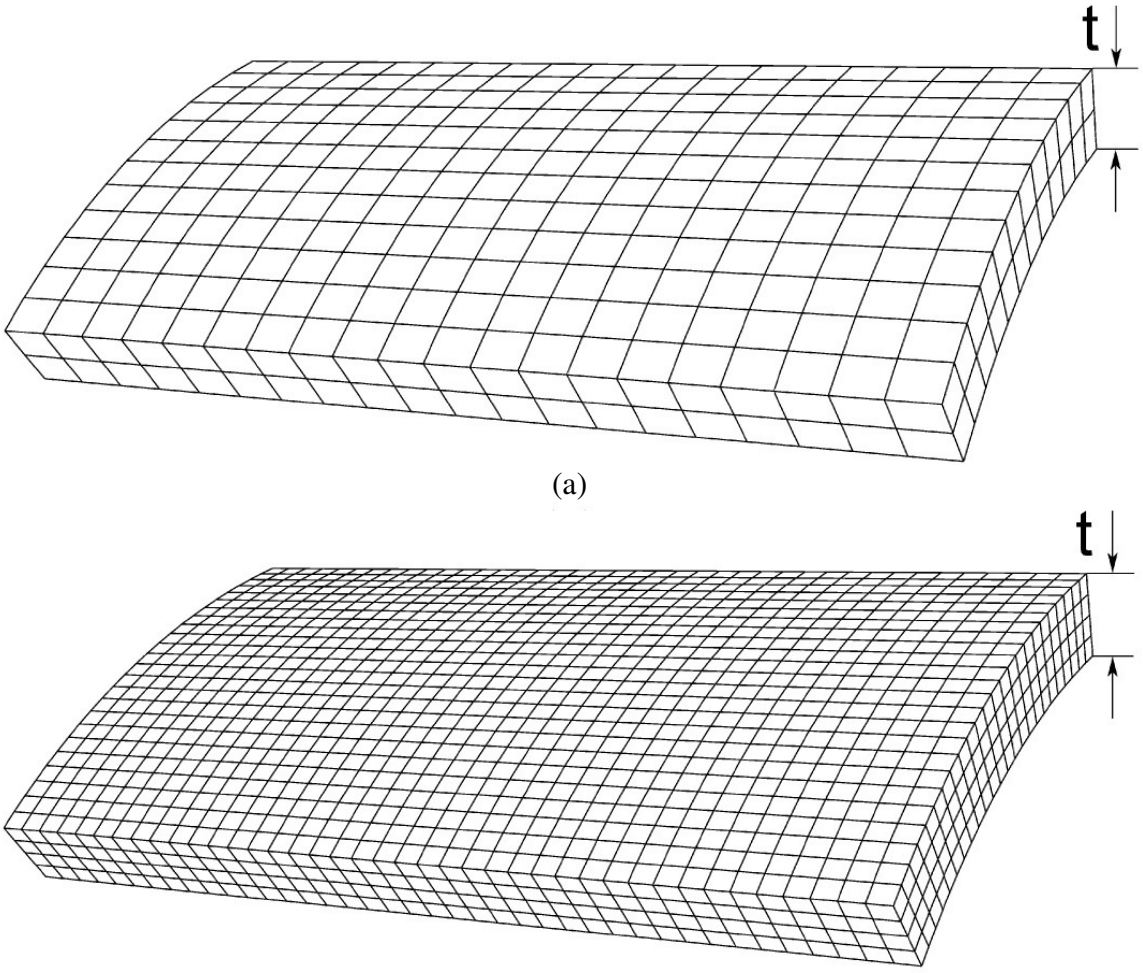

Figure 5.24 Two nearly isotropic mesh densities considered for reeling pipe with Lüders bands: (a) Two elements and (b) four elements through the thickness.

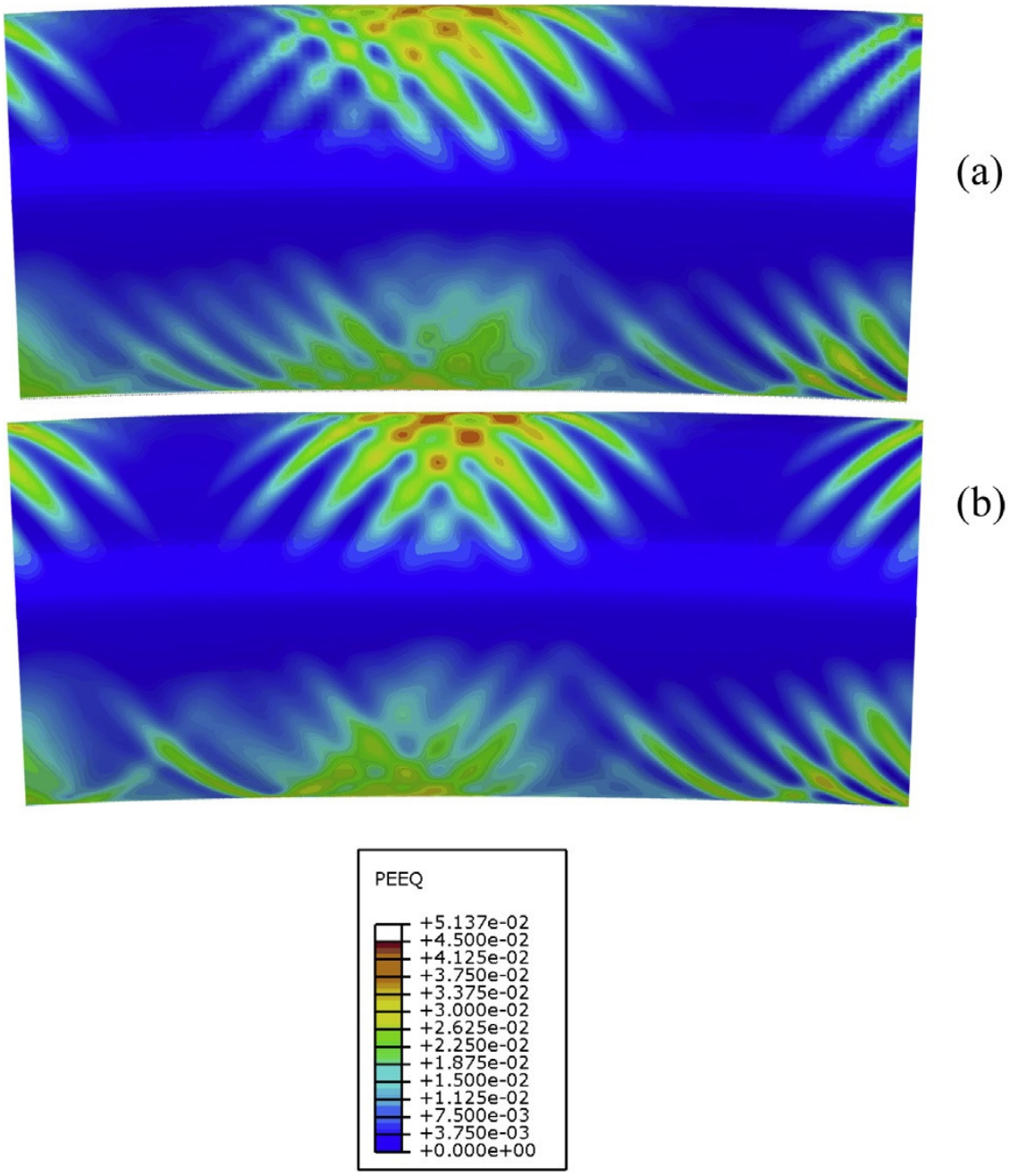

Figure 5.25 Lüders band clusters developed in models with different mesh densities: (a) Two elements and (b) four elements through the thickness.

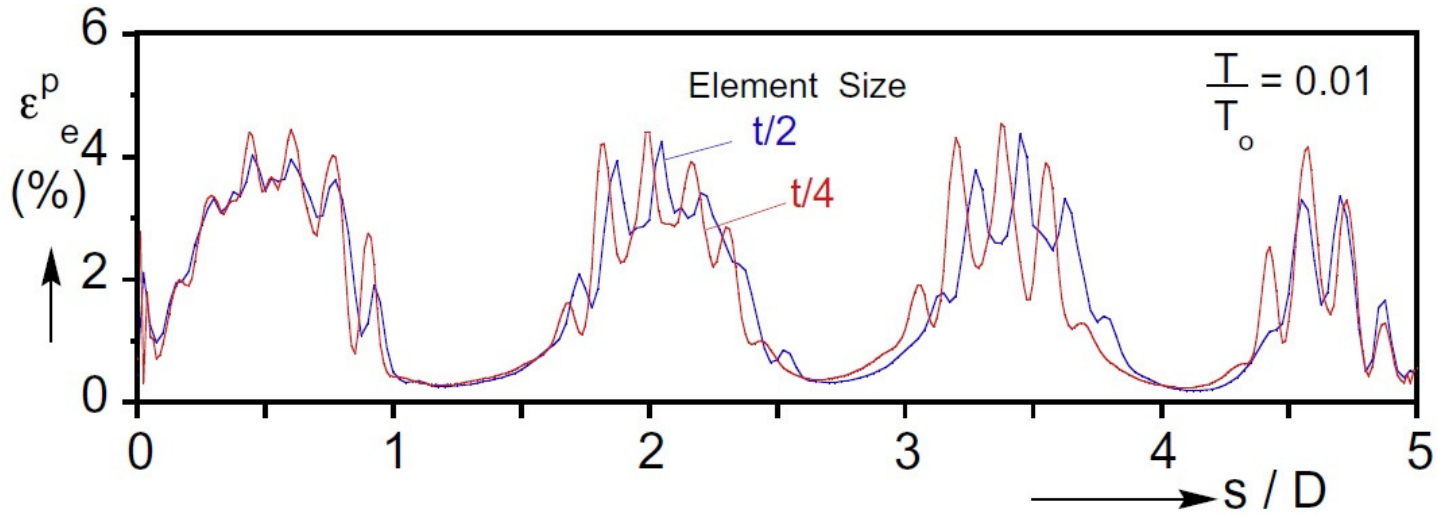

Figure 5.26 Axial strain profiles of the top generators developed in models with two and four elements through the thickness.

Chapter 6: CONCLUSIONS

The reeling installation process of offshore pipelines, as is practiced by modern reeling facilities, involves repeated elasto-plastic bending, unloading, and reverse bending of the pipe. The repeated excursions to plastic bending strains of 1-3% alter the material properties of the line and ovalize its cross section. Back tension, often applied in order to reduce the possibility of catastrophic local buckling by bending, tends to aggravate the cross sectional changes and elongates the pipe. The induced structural and material changes can be further agravated by geometric and material discontinuities in the pipeline and material instability in the form of Lüders banding. A large-scale numerical framework of reeling has been presented and used to study the effect of reeling on three related aspects of the process. This chapter summarizes the major conclusions drawn from each component of this study.

6.1 Effects of Reeling on Pipe Structural Performance

The effects of back tension applied during the reeling process were studied experimentally in Kyriakides and Mok [1992], and the results were recently summarized in Kyriakides [2017]. It was demonstrated that the changes in cross sectional geometry and material properties induced by reeling/unreeling cycles are strongly dependent on the applied back tension. In addition, the induced degradation of the pipe results in decreased collapse pressure.

The present study used two modeling schemes to simulate the experiments and establish the geometric and material changes induced to a pipeline by repeated reeling/unreeling cycles. The first is a large-scale 3-D finite element model in which the pipe is modeled as a shell. The model includes proper treatment of contact and nonlinear kinematic hardening plasticity based on Chaboche's model (see Section 2.1). The second

is a simplified 2-D model in which all problem variables are assumed to remain uniform along the length. The formulation includes pipe geometric cross sectional nonlinearities, contact, and nonlinear kinematic hardening plasticity based on the Tseng-Lee model (see Section 2.2).

The two models were used to simulate all experiments in Kyriakides and Mok [1992] and were compared with the experiments. The following main conclusions can be drawn from this comparison.

a. During each cycle, ovalization grows during winding, relaxes somewhat during unwinding and straightening, but a permanent residual ovality is left.
b. Back tension, even at modest levels, causes a net elongation of the line each time it is plastically deformed by bending during the reeling/unreeling cycle. Thus, the line stretches during winding and once more during the unwinding and straightening.
c. Both the 2-D and 3-D models reproduced the ovality and axial elongation induced at various levels of tension with good accuracy for the first and second cycles, while the results for the third cycle were generally overpredicted.
d. The induced changes in sectional geometry and material properties both tend to increase significantly with increased back tension and accumulate with additional bending/straightening cycles.
e. For the experiments of one reeling/unreeling cycle followed by external pressure loading, both numerical models are capable of predicting the collapse pressure with high accuracy. The collapse pressure was shown to decrease significantly with increased tension, which is primarily a result of the induced ovality.
f. The axially uniform 2-D model is a highly efficient modeling tool that is adequate if the objective of modeling is to establish the cross sectional changes induced to the pipe by the reeling process and assess any degradation in its mechanical performance.

g. The 3-D model, although computationally expensive, can yield a more complete picture of the evolution of sectional geometry and other aspects of the problem, such as the role of back tension on line configuration, the interaction of the pipe with the reel through contact and for pipelines with variations in geometry or properties such as the problems considered in Chapter 4. Such issues can be essential in assessing the integrity of the pipeline during reeling.

6.2 Effect of Geometric and Material Discontinuities on The Reeling of Pipelines

Discontinuities in mechanical properties and wall thickness of adjacent strings of pipe act as stress risers, lead to localized deformations, and can cause local buckling, collapse and rupture. The finite element model for simulating the reeling of a pipeline developed in Chapter 3 is extended to include a discontinuity in the pipeline. The model was used to assess the effect of discontinuities in wall thickness and material yield stress on the integrity of the pipeline. For a given pipe geometry, mechanical properties and reel radius, the variables of interest are the magnitude of the discontinuity and the tension applied to the line during winding and unwinding. Results from reeling/unreeling simulations using twelve-inch pipes with discontinuities of wall thickness and yield stress of various levels were performed for different levels of back tension. The following observations can be made and conclusions drawn from the results.

a. Both material and wall thickness discontinuities cause a disturbance that affects a section of pipe a few diameters long. In the neighborhood of the discontinuity the curvature localizes which leads to a spike in strain and ovality. The extent of the disturbance is governed by the bending strain imposed by the ratio of pipe to reel diameter.

b. The extent of the disturbance can be reduced by an increase in the back tension. However, increase in tension has the down side of causing higher ovality in the pipeline and a corresponding reduction in its collapse pressure.
c. The extent of the disturbance can also be reduced by an increase in the wall thickness of the pipe, with of course its additional cost downside.
d. For some combinations of tension and magnitude of discontinuity, the pipe collapses locally during winding. Collapse is in the form of a bending-type, sharp inward kink. The deformation is severe enough to rupture the line on the reel or later during unwinding. In other cases, the pipeline survives the winding, but the local deformation caused by the discontinuity is severe enough that it buckles and collapses the pipeline as it straightens during unwinding. In such cases the buckle occurs on the side of the pipe that was tensioned during winding.

In summary, the results of this study suggest that pipe discontinuities can be the cause of local collapse and rupture during a reeling installation process. Consequently, a modeling framework such as the one presented in this study should be used to generate a design protocol for a reel-installed pipeline project. Since failures can occur during reeling and unreeling, the complete history seen by a discontinuity should be considered in sensitive pipeline projects.

6.3 REELING OF PIPE WITH LÜDERS BANDS

This part of the study examined the behavior of a pipe that exhibits Lüders banding in the practical setting of a reeling operation. The reeling process was modeled with finite elements with a mesh that is fine enough to capture the evolution of Lüders banding that develops. Similar with the study of the behavior of such a pipe under pure

bending in Hallai and Kyriakides [2011b], an up-down-up stress-strain response over the extent of the Lüders deformation was adopted.

Unlike in the case of pure bending where premature local collapse occurs for some combinations of Lüders strain and tube D/t, pipes with the same properties survived when reeled with applied back tension. For pure bending, the pipe collapses when the high curvature section develops to a certain length. For reeling, however, the zone of highest curvature is limited to a couple of tube diameters. This zone is in turn stabilized by the adjacent lower curvature zones, thus delaying buckling. The back tension and the contact with the surface of the reel have additional a stabilizing effects. Thus overall, pipe reeled under some level of back tension is much more stable than under pure bending.

In reeling induced bending, Lüders banding produces inclined bands of localized deformation similar to those seen under pure bending. The bands are also organized in clusters but with distinctly different spatial distribution than that of pure bending. Now the clusters are separated by sections of pipe free of Lüders bands. For realistic pipe and reel geometries, the average bending strain imposed by the curvature of the reel is lower than the strain induced by Lüders banding. Accordingly, the clusters are separated by relatively undeformed sections so that the bending strain averages out to the value imposed by the reel. The applied tension introduces some differences between the deformation patterns that develop on the tensioned and compressed sides of the pipe. The bands on the compressed side are somewhat more diffuse and exhibit a more regular distribution along the length. It is further demonstrated that as a consequence of the spatially periodic distribution of bending deformation due to the clustering of Lüders bands, the ovalization develops axial undulations. Such undulations can act as imperfections in subsequent, particularly compressive loadings of the structure.

Reeling process factors that affect this type of Lüders banding were studied parametrically and the following observations can be made from the results:

a. The extent of Lüders strain in the material plays a deciding role in the spatial distribution of the clusters of bands that develop and their strain intensity. Lüders strain that is smaller than the bending strain imposed by the reel results in nearly uniformly distributed plastic bending strain. Lüders strain that is of the order of the reel induced bending strain or larger results in increasingly more separated clusters of bands with larger local strains.
b. Back tension influences the asymmetry between the banded deformation in the tensioned and compressed sides of the pipe. Lower tension makes the deformation more symmetric and larger tension increases the asymmetry. Concurrently, tension tends to increase the induced ovality, which in turn reduces the collapse pressure of reeled pipe.
c. The reel radius, or more precisely the ratio of the pipe-to-reel diameter, dictates the induced bending strain and consequently influences the clustering and intensity of Lüders banding.
d. Increasing the pipe wall thickness, or decreasing its D/t, does not influence significantly the clustering of deformation patterns but, as expected, reduces the induced ovality.

References

Abeyaratne, R., Knowles, J.K. (2006). *Evolution of Phase Transitions.* Cambridge University Press, New York.

Aegir: https://hmc.heerema.com/fleet/aegir/

Aguirre, F., Kyriakides, S. and Yun, H.D. (2004). Bending of steel tubes with Lüders bands. *Int. J. Plast.* 20, 1199-1225.

Apache II: http://www.technip.com/en/vessel/apache-ii

Armstrong, P.J. and Frederick, C.O. (1966). A mathematical representation of the multiaxial Bauschinger effect. Berkeley Nuclear Laboratories, R&D Department, Rep. No. RD/B/N/731.

Bauer, J., Schwinn, V., Tacke K.-H. (2002). Recent quality achievements on steel plate for line pipe. 4th Int'l Pipeline Conf., IPC02-27316, Oct. 2002, Calgary, Canada.

Brazier, L.G. (1927). On the flexure of thin cylindrical shells and other thin sections. *Proc. Royal Soc.* London **A116**, 104-114.

Brown, G., Tkaczyk, T., Howard, B. (2004). Reliability based assessment of minimum reelable wall thickness for reeling. Proc. Int'l Pipeline Conf., IPC04-0733, Oct. 2004, Calgary, Canada.

Butler, J.F. (1962). Lüders front propagation in low-carbon steels. *J. Mech. Physics of Solid* **10**, 313-334.

Chaboche, J.-L. (1986). Time-independent constitutive theories for cyclic plasticity. *Int'l J. Plast.* **2**, 149-188.

Chatzopoulou, G., Karamanos, S.A. and Varelis, G.E. (2016). Finite element analysis of cyclically-loaded steel pipes during deep water reeling installation. *Ocean Eng.* **124**, 113–124.

Corona, E. and Kyriakides, S. (1988). On the collapse of inelastic tubes under combined bending and pressure. *Int'l J. Solids Structures* **24**, 505-535.

Corona, E. and Kyriakides, S. (1991). An experimental investigation of the degradation and bucking of circular tubes under cyclic bending and external pressure. *Thin-Walled Struct.* **12**, 229-263.

Corona, E., Lee, L.-H. and Kyriakides, S. (2006). Yield anisotropy effects on buckling of circular tubes under bending. *Int'l J. Solids Struct.* **43**, 7099-7118.

Corona, E., Shaw, J.A. and Iadicola, M.A. (2002). Buckling of steel bars with Lüders bands. *Int'l J. Solids Struct.* **39**, 3313-3336.

Cottrell, A.H., Bilby, B.A. (1949). Dislocation theory of yielding and strain ageing of iron. *Proc. Phys. Soc.* **62/I-A**, 49–62.

Crome, T. (1999). Reeling of pipelines with thick insulation coating, finite element analysis of local buckling. Proc. *Offshore Tech. Conf.*, OTC 10715, V. 3, 560-566, May 1999, Houston, TX.

Dafalias, Y.F. and Popov, E.P. (1975). A Model of nonlinearly hardening materials for complex loading. *Acta Mechanica* **21**, 173-192.

Dafalias, Y.F. and Popov, E.P. (1976). Plastic internal variables formalism of cyclic plasticity. *ASME J. Appl. Mechanics* 43, 645-651.

Das, S., Cheng, J.J., Murray, D.W., Nazemi, N. (2008). Effect of monotonic and cyclic bending deformations on NPS12 wrinkled steel pipeline. *ASCE J. Struct. Eng.,* **134**:12, 1810-1817.

Denniel, S., Tkaczyk, T., Howard, B., Levold, E., Aamlid, O. (2009). On the influence of mechanical and geometrical property distribution on the safe reeling of rigid pipelines. Proc. *28th Int'l Conf. Ocean, Offshore Arctic Eng.*, OMAE2009-79344, June 2009, Honolulu, HI, USA.

Deep Blue: http://www.technip.com/en/vessel/deep-blue

Deep Energy: www.technip.com/en/vessel/deep-energy

Dyau, J. Y., and Kyriakides, S. (1992). On the response of elastic-plastic tubes under combined bending and tension. *ASME J. Offshore Mech. Arctic Eng.* **114**, 50-62.

Ericksen, J.L. (1975). Equilibrium of bars. *J. Elasticity* **5**, 191-201.

Ernst, H.A., Bravo, R.E., Schifini, R., Passarella, D.N. (2007). Probabilistic fracture mechanics methodology applied to pipes subjected to multiple reeling cycles. Proc. 26th Int'l Conf. Offshore Mechanics & Arctic Eng., OMAE2007-29345, June 2007, San Diego, CA, USA.

Estrin, Y. and Kubin, L.P. (1995). Spatial coupling and propagative plastic instabilities. In *Continuum Models for Materials with Microstructure.* Ed. H.-B. Muhlhaus. © John-Wiley and Sons, Ltd.

Hahn, G.T. (1962). A model for yielding with special reference to the yield-point phenomena of iron and related BCC metals. *Acta Metal.* **10**, 727–738.

Hall, E.O. (1970). *Yield point phenomena in metals and alloys*. Plenum Press, New York.

Hallai, J.F., Kyriakides, S. (2011a). On the effect of Lüders bands on the bending of steel tubes. Part I: Experiments. *Int'l J. Solids & Structures* **48**, 3275-3284.

Hallai, J.F., Kyriakides, S. (2011b). On the effect of Lüders bands on the bending of steel tubes. Part II: Analysis. *Int'l J. Solids & Structures* **48**, 3285-3298.

Hallai, J.F., Kyriakides, S. (2012). Bending capacity of tubes with Lüders bands. Influence of geometric and material parameters. *Proc. 31st ASME Int'l Conf. on*

Ocean, Offshore Arctic Eng., June 2012, Rio de Janeiro, Brazil, OMAE2012-83604.

Hallai, J.F., Kyriakides, S. (2013). Underlying material response for Lüders-like instabilities. *Int'l J. Plasticity* **47**, 1-12.

Hassan, T. and Kyriakides, S. (1992). Ratcheting in cyclic plasticity-Part I: uniaxial behavior. *Int'l J. Plasticity* 8, 91-116.

Hassan, T., Corona, E. and Kyriakides, S. (1992). Ratcheting in cyclic plasticity-Part II: multiaxial behavior. *Int'l J. Plasticity* 8, 117-146.

Hassan, T. and Kyriakides, S. (1994a). Ratcheting of cyclically hardening and softening materials: I. Uniaxial behavior. *Int'l J. Plasticity* 10, 149-184.

Hassan, T. and Kyriakides, S. (1994b). Ratcheting of cyclically hardening and softening materials: II Multiaxial behavior. *Int'l J. Plasticity* 10, 185-212.

Imamura, J., Hayakawa, H. and Taoka, T. (1971). Contribution of local strain rate at Lüders band front to grain size dependence of lower yield stress in iron. *Iron & Steel Inst. Japan* **11**, 191-200.

Jiao, R., Kyriakides, S. (2009). Ratcheting, wrinkling and collapse of tubes under axial cycling. *Int'l J. Solids Structures* 46, 2856-2870.

Johnston, W.G. and Gilman, J.J. (1959). Dislocation velocities, dislocation densities, and plastic flow in lithium fluoride crystals. *J. Appl. Phys.* **30**, 129–144.

Ju, G.T. and Kyriakides, S. (1991). Bifurcation buckling versus limit load instabilities of elastic-plastic tubes under bending and pressure. *ASME J. Offshore Mech. Arctic Eng.* **113**, 43-52.

Ju, G.T. and Kyriakides, S. (1992). Bifurcation and localization instabilities in cylindrical shells under bending: Part II Predictions. *Int'l J. Solids Structures* **29**, 1143-1171.

Kyriakides, S. (2001). Propagating instabilities in materials. In: Materials Science for the 21st Century, *Society of Materials Science, Japan*, **1**, 316–325, May 2001.

Kyriakides S. (2017). Effects of reeling on pipe structural performance—Part I: Experiments, *ASME J. Offshore Mech. Arctic Eng.*, **139**, 051706.

Kyriakides, S. and Corona, E. (2007). Mechanics of Offshore Pipelines: Volume 1 Buckling and Collapse. Elsevier, Oxford, UK and Burlington, Massachusetts.

Kyriakides, S., Corona, E. and Miller, J.E. (2004). Effect of yield surface evolution on bending induced cross sectional deformation of thin-walled sections. *Int'l J. Plasticity* **20**, 607-618.

Kyriakides, S., Dyau, J.-Y., and Corona, E., (1994) I. Pipe Collapse Under Bending, Tension and External Pressure (BEPTICO) and II. Simulation of pipeline Reeling/Unreeling (REELING). Computer Program Manual, Univ. Texas at

Austin, Engineering Mechanics Research Laboratory Report No. 94/4, January 1994.

Kyriakides, S. and Miller, J.E. (2000). On the propagation of Lüders bands in steel strips. ASME *J. Appl. Mech.* **67**, 645-654.

Kyriakides, S., and Mok, S. W. (1992). On the effect of reeling on pipe collapse. Univ. Texas at Austin, Engineering Mechanics Research Laboratory, Report No. 92/6, August 1992.

Kyriakides, S. and Ju, G.T. (1992). Bifurcation and localization instabilities in cylindrical shells under bending: Part I Experiments. *Int'l J. Solids Structures* **29**, 1117-1142.

Kyriakides, S., Ok, A. and Corona, E. (2008). Localization and propagation of curvature under pure bending in steel tubes with Lüders bands. *Int'l J. Solids Struct.* **45**, 3074-3087.

Kyriakides, S. and Shaw, P.K., (1987). Inelastic buckling of tubes under cyclic bending. *ASME J. Pressure Vessel Techn.* **109**, 169-178.

Lemaitre, J., Chaboche, J.-L. (1990). *Mechanics of Solid Materials*. Cambridge University Press

Liu, Y. and Kyriakides, S. (2014). Effect of geometric and material discontinuities on the reeling of pipelines. *33rd Int'l Conf. Ocean, Offshore Arctic Eng.*, OMAE2014-24474, June 2014, San Francisco, CA, USA.

Liu, Y., Kyriakides, S. and Hallai, J.F. (2015). Reeling of pipe with Lüders bands. *Int'l J. Solids Structures* **72**, 11-25.

Liu, Y., Kyriakides, S. (2016). Effect of reeling on pipeline structural performance. *35th Int'l Conf. Ocean, Offshore Arctic Eng.,* OMAE2016-54866, June 2016, Busan, South Korea.

Liu, Y., Kyriakides, S., and Dyau, J.-Y. (2017). Effects of reeling on pipe structural performance—Part II: Analysis. *ASME J. Offshore Mech. Arctic Eng.*, **139**, 051707.

Liu, Y. and Kyriakides, S. (2017). Effect of geometric and material discontinuities on the reeling of pipelines. *Applied Ocean Research*, **65**, 238-250.

Louche, H. and Chrysochoos, A. (2001). Thermal and dissipative effects accompanying Lüders band propagation. *Mater. Science Eng.* **A307**, 15-22.

Mroz, Z. (1967). On the description of anisotropic work hardening. *J. Mech. Physics of Solids* **15**, 163-175

Meissner, A., Erdelen-Peppler, M., Schmidt, T. (2012). Impact of reel-laying on mechanical pipeline properties investigated by full- and small-scale reeling simulations. *Int'l J. Offshore & Polar Eng.* **22**, 282-289.

Morrison, W.B. and Glenn, R.C. (1968). Examination of the Lüders front in a low-carbon steel by transmission electron microscopy. *J. Iron Steel Inst.* **206**, 611–612.

Nacar, A., Needleman, A. and Ortiz, M. (1989). A finite element method for analyzing localization in rate dependent solids at finite strains. *Comp. Methods Appl. Mech. Eng*. **73**, 235–258.

Needleman, A. (1988). Material rate dependence and mesh sensitivity in localization problems. *Comp. Methods Appl. Mech. Eng.* **67,** 69-85.

Netto, T.A., Lourenco, M.I., Botto, A. (2008). Fatigue performance of pre-strained pipes with girth weld defects: full-scale experiments and analyses. *Int'l J. Fatigue* **30**, 767-778.

Ortiz, M., Leroy, Y. and Needleman, A. (1987). A finite element method for localized failure analysis. *Comp. Methods Appl. Mech. Eng*. **61**, 189–214.

Seven Navica:

http://www.subsea7.com/content/dam/subsea7/documents/whatwedo/fleet/rigidpipelay/Seven%20Navica.pdf

Seven Oceans:

http://www.subsea7.com/content/dam/subsea7/documents/whatwedo/Fleet_2017/Seven%20Oceans.pdf

Seven Pacific:

http://www.subsea7.com/content/dam/subsea7/documents/whatwedo/Fleet_2017/Seven%20Pacific.pdf

Shaw, J.A. and Kyriakides, S. (1998). Initiation and propagation of localized deformation in elasto-plastic strips under uniaxial tension. *Int'l J. Plast*. **13**, 837–871.

Shioya, T. and Shiroiri, J. (1976). Elastic-plastic analysis of the yield process in mild steel. *J. Mech. Phys. Solids* **24**, 187–204.

Simo, J.C. and Armero, F. (1992). Geometrically non-linear enhanced strain mixed methods and the method of incompatible modes. *Int'l J. Num. Methods Eng.* **33**, 1413–1449.

Smith, D., Tkaczyk, T., Denniel, S. (2011). Reliability based assessment of minimum wall thickness for reeling: a focus on cold worked pipe. Proc. *30th Int'l Conf. Ocean Offshore & Arctic Eng*., OMAE2011-49389, June 2011, Rotterdam, The Netherlands.

Sriskandarajah, T., Rao, V., Manouchehri, S. (2011). Integral buckle arrestors for deepwater rigid pipelines installed by reeling method. *30th Int'l Conf. Ocean, Offshore Arctic Eng*., OMAE2011-50184, June 2011, Rotterdam, The Netherlands.

Tseng, N.T. and Lee, G.C. (1983). Simple plasticity model of two-surface type. *ASCE J. Eng. Mechanics* **109**, 795-810.

Tsuru, E., Shinohara, Y, Hara, T., Hattori, Y. (2012). Potential strain limit for girth-welded UOE line pipes commercially manufactured for strain-based design. *22nd Int'l Offshore & Polar Eng. Conf. ISOPE 2012*, pp. 457-463, June 2012, Rhodes, Greece.

Tsuru, E., Shinohara, Y, Nagai, K., Nagata, Y., Hamatani, H. (2013). Reeling capability of non-heat-treated ERW line pipes in R-lay. *23rd Int'l Offshore & Polar Eng. Conf. ISOPE 2013*, pp. 560-566, July 2013, Anchorage, Alaska.

Tsukahara, H. and Iung, T. (1998). Finite element simulation of the Piobert–Lüders behavior in a uniaxial tensile test. *Mat. Sci. Eng.* **A248**, 304–308.

Wilson, E.L., Taylor, R.L., Doherty, W.P. and Ghaboussi, J. (1973). Incompatible displacement models. In: Fenves, S.J. et al. (Eds.), *Numerical and Computer Models in Structural Mechanics*. Academic Press, New York.

Yoshida, F., Kaneda, Y., Yamamoto, S. (2008). A plasticity model describing yield-point phenomena of steels and its application to FE simulation of temper rolling. *Int'l J. Plast.* **24,** 1792-1818.

Zhang, J. and Jiang, Y. (2005). Lüders bands propagation of 1045 steel under multiaxial stress state. *Int'l J. Plast.* **21**, 651-670.

Zhang, Y.T., Ao, T, Jiao, W., Cui, Y.H. (2008). Prediction of the Lüders band in fine grained steel strips under uniaxial tension. *Computational Materials Science* **41**, 547-552.

Vita

Yafei Liu entered Beijing Institute of Technology and received the degree of Bachelor of Engineering in Materials Engineering in July, 2010. In August 2010, he joined the Engineering Mechanics graduate program at the University of Texas at Austin pursuing a Ph.D. degree.

Permanent address (or email): yafei.liu@utexas.edu

This dissertation was typed by the author.